

# Robust mass damper design for bandwidth increase of motion stages

***Citation for published version (APA):***

Verbaan, C. A. M. (2015). *Robust mass damper design for bandwidth increase of motion stages*. [Phd Thesis 1 (Research TU/e / Graduation TU/e), Mechanical Engineering]. Technische Universiteit Eindhoven.

***Document status and date:***

Published: 20/04/2015

***Document Version:***

Publisher's PDF, also known as Version of Record (includes final page, issue and volume numbers)

***Please check the document version of this publication:***

- A submitted manuscript is the version of the article upon submission and before peer-review. There can be important differences between the submitted version and the official published version of record. People interested in the research are advised to contact the author for the final version of the publication, or visit the DOI to the publisher's website.
- The final author version and the galley proof are versions of the publication after peer review.
- The final published version features the final layout of the paper including the volume, issue and page numbers.

[Link to publication](#)

***General rights***

Copyright and moral rights for the publications made accessible in the public portal are retained by the authors and/or other copyright owners and it is a condition of accessing publications that users recognise and abide by the legal requirements associated with these rights.

- Users may download and print one copy of any publication from the public portal for the purpose of private study or research.
- You may not further distribute the material or use it for any profit-making activity or commercial gain
- You may freely distribute the URL identifying the publication in the public portal.

If the publication is distributed under the terms of Article 25fa of the Dutch Copyright Act, indicated by the "Taverne" license above, please follow below link for the End User Agreement:

[www.tue.nl/taverne](http://www.tue.nl/taverne)

***Take down policy***

If you believe that this document breaches copyright please contact us at:

[openaccess@tue.nl](mailto:openaccess@tue.nl)

providing details and we will investigate your claim.

# Robust Mass Damper Design for Bandwidth Increase of Motion Stages

Kees Verbaan

The research leading to this dissertation is funded and actively supported by ASML Research, Veldhoven, The Netherlands.



Robust Mass Damper Design for Bandwidth Increase of Motion Stages.  
By C.A.M. Verbaan – Eindhoven University of Technology, 2015 – Ph.D.-Thesis.  
Reproduction: Ipskamp Drukkers B.V., Enschede, the Netherlands.  
Cover Design: Susanne Verbaan-Van Erk.

A catalogue record is available from the Eindhoven University of Technology Library.  
ISBN : 978-90-386-3823-2.  
NUR : 978

Copyright © 2015 by C.A.M. Verbaan. All rights reserved.

# Robust Mass Damper Design for Bandwidth Increase of Motion Stages

## PROEFSCHRIFT

ter verkrijging van de graad van doctor  
aan de Technische Universiteit Eindhoven,  
op gezag van de rector magnificus prof.dr.ir. C.J. van Duijn,  
voor een commissie aangewezen door het College voor Promoties,  
in het openbaar te verdedigen op maandag 20 april 2015 om 16:00 uur

door

Cornelis Abraham Marinus Verbaan

geboren te Utrecht



Dit proefschrift is goedgekeurd door de promotoren en de samenstelling van de promotiecommissie is als volgt:

|             |                            |                                |
|-------------|----------------------------|--------------------------------|
| voorzitter: | prof.dr.ir. M.G.D. Geers   |                                |
| promotor:   | prof.dr.ir. M. Steinbuch   |                                |
| copromotor: | dr.ir. P.C.J.N. Rosielle   |                                |
| leden:      | prof.dr.ir. H. Butler      |                                |
|             | prof.dr.ir. G.W.M. Peters  |                                |
|             | prof.dr.ir. A. de Boer     | Universiteit Twente            |
|             | prof.dr.ir. J. Swevers     | Katholieke Universiteit Leuven |
| adviseur:   | dr.ir. S.H. van der Meulen | ASML Research                  |

# Societal Summary

Integrated circuits (IC's) are widely used in devices nowadays to control process parameters. Examples are transportation vehicles, medical equipment, computers and phones, and industrial plants. The amount of IC's in all types of products has increased tremendously during the last decades. This functionality became usable by miniaturization of the IC's, which enabled to apply more components within the size of an IC, combined with a decrease in production cost. The most important step in the production of IC's is the illumination of the IC pattern on the surface of a wafer which is provided with a photo-sensitive layer. This illumination is executed after positioning the wafer with respect to the optical column by means of a motion stage. Mechanical vibrations in the motion stage take long to fade naturally and compromise image quality as they limit the control systems' bandwidth. They are related to design specific natural frequencies of the motion stage. This thesis presents the idea of adding mechanical damper devices to the motion stage to increase the damping of these natural frequencies. This leads to a fast decrease of the vibration amplitude by dissipating the energy stored in the vibrations. The result is an increase in control bandwidth, which allows increased productivity and hence lower prices. Analyses have been performed on complex stage designs to quantify the performance improvement. Experimental validation showed the correspondence between theory and practice. This thesis proves a damper concept that enables further increase of density hence functionality of IC's. The boundaries of the societal impact are not easily identified.



# Robust Mass Damper Design for Bandwidth Increase of Motion Stages

In the production of integrated circuits (e.g. computer chips), optical lithography is used to transfer a pattern onto a semiconductor substrate, which is called wafer. This wafer is fixed on top of a motion stage which positions the wafer's surface with respect to the optical column used for projection of the pattern.

The accuracy of the motion system largely determines the minimum feature size that can be projected and the speed of the motion stage is a measure for the throughput. Both the accuracy and the velocity of the motion stage are determined by a position control system which exists of a feedback loop with a PID<sup>+</sup> controller and a feedforward path. The gain of the feedback loop, which has to be high to counteract disturbances, is usually limited by flexible behavior of the stage mechanics. The resonance frequencies as well as the modal damping values of these resonances determine to what extent bandwidth limitations exist. An increase of the modal damping, which is usually low in high-precision mechanical designs, results in a decreased amplification factor at these resonances and, therefore, provides additional room to increase the controllers' frequency dependent gain.

This thesis addresses the challenge to increase the modal damping of the bandwidth limiting resonances of motion stages. This modal damping increase is realized by adding passive elements, called robust mass dampers (RMDs), at specific stage locations. These RMDs exist of a mass, mounted to the stage by a parallel spring and a high-damping dashpot and provide robust and broad banded damping to the flexibilities.

The theoretical advantages of RMDs for an abstracted stage model and ideal damper models are used as a starting point and a closed-loop criterion is derived as performance measure for further optimization

A robust mass damper design is presented based on a high-viscosity fluid in order to maintain linear time-invariant behavior and the performance limitations of this damper are investigated. Especially, the linear visco-elastic behavior introduces differences with respect to an ideal damper model. Multi-mode Maxwell models are created to take this behavior into account.

Subsequently, two complex motion stage designs are elaborated and RMDs are designed in order to maximize the performance. The damper parameters that have to be determined are mass, stiffness and damping. In both cases, the optimal RMD parameters are obtained by executing optimization algorithms. These optimizations include models, obtained by finite-element modal analyses and RMD models which include the linear visco-elastic fluid model.

The first motion stage design is optimized based on an open-loop criterion for modal damping increase between 1 and 4 kHz. Experimental validation shows that a suppression factor of over 24 dB is obtained in this frequency range. In addition, a suppression of 19 dB is visible up to 6 kHz. Transient time responses show an amplitude decrease rate which is 20 times faster for the damped stage than for the undamped stage. In addition, the optimization results show that a larger suppression factor can be obtained by applying linear viscoelastic materials compared to applying purely viscous damping.

The second motion stage design is optimized under closed-loop conditions and in addition to the RMD properties as listed before, the controller parameters are included in the optimization. RMDs are designed and experimental identification of both the undamped and damped stage is performed. For the stage with RMDs, a low-frequency sensitivity improvement of 9 dB is proven in the vertical direction of motion for a  $PID^+$  controller by experimental validation on a six degree of freedom experimental motion stage. This corresponds to an increase of the bandwidth frequency of 50 %.

In addition to the improvements in input-output behavior (frequency response function), the stage shows inherently better damped behavior for a number of modes. This improves the spatial behavior for modes that are not observed in the FRF.

The theoretical and experimental results show that there is great potential of using the Robust Mass Dampers as an add-on to high-precision motion stages with high bandwidths.

# Contents

|  |     |
|--|-----|
| Societal Summary   | iii |
| Summary  | v   |
| Chapter 1    Introduction  | 1   |
| 1.1    IC production and lithography                                 | 2   |
| 1.2    Motion stages   | 3   |
| 1.3    Performance limiters  | 4   |
| 1.4    Thesis goals  | 5   |
| 1.5    Outline   | 6   |
| Chapter 2    Robust Mass Dampers and Broad Banded Damping            | 9   |
| 2.1    Introduction  | 10  |
| 2.2    Tuned Mass Dampers  | 11  |
| 2.3    The undamped stage model                                      | 12  |
| 2.4    The damped stage model  | 16  |
| 2.5    Performance improvement in z-direction                        | 20  |
| 2.6    Performance improvements in $\varphi$ - and $\psi$ -direction | 23  |
| 2.7    Plant robustness increase                                     | 24  |
| 2.8    Damper design & validation                                    | 26  |
| 2.9    Conclusions   | 29  |

|                  |   |           |
|------------------|---|-----------|
| <b>Chapter 3</b> | <b>Sensitivity Based Iterative Approach to Increase Closed-loop Performance</b>       | <b>31</b> |
| 3.1              | Introduction  | 32        |
| 3.2              | Undamped stage behavior   | 33        |
| 3.3              | The damped stage model  | 39        |
| 3.4              | Closed-loop parameter optimization  | 41        |
| 3.5              | Performance results   | 46        |
| 3.6              | Concluding remarks  | 47        |
| 3.7              | Discussion  | 49        |
| <br>             |   |           |
| <b>Chapter 4</b> | <b>Linear Viscoelastic Characterization of an Ultra-high Viscosity Fluid</b>          | <b>53</b> |
| 4.1              | Introduction  | 54        |
| 4.2              | Damper hardware design  | 57        |
| 4.3              | Limits and assumptions  | 58        |
| 4.4              | RMD mechanism characterization  | 59        |
| 4.5              | Fluid model calculation   | 65        |
| 4.6              | Fluid model validation  | 72        |
| 4.7              | Concluding remarks  | 73        |
| 4.8              | Discussion  | 74        |
| <br>             |   |           |
| <b>Chapter 5</b> | <b>Damping Optimization of a Complex Motion Stage and Experimental Modal Analysis</b> | <b>75</b> |
| 5.1              | Introduction  | 76        |
| 5.2              | Stage and damper dynamic models   | 78        |
| 5.3              | RMD parameter calculation   | 85        |
| 5.4              | Damper design & validation  | 93        |
| 5.5              | Experimental modal analysis on the motion stage                                       | 96        |
| 5.6              | Concluding remarks  | 100       |
| 5.7              | Closing remarks   | 102       |

|                         |   |            |
|-------------------------|---|------------|
| <b>Chapter 6</b>        | <b>Closed-loop Performance Optimization and Experimental Validation</b> | <b>105</b> |
| 6.1                     | Introduction  | 106        |
| 6.2                     | Experimental motion stage   | 108        |
| 6.3                     | Closed-loop parameter optimization                                      | 111        |
| 6.4                     | Practical elaboration of the optimization procedure                     | 114        |
| 6.5                     | Optimization results  | 116        |
| 6.6                     | Experimental validation in closed loop                                  | 118        |
| 6.7                     | Advantageous side-effects of the RMDs                                   | 123        |
| 6.8                     | Concluding remarks  | 124        |
| 6.9                     | Discussion  | 125        |
| <b>Chapter 7</b>        | <b>Conclusions and Recommendations</b>                                  | <b>129</b> |
| 7.1                     | Concluding remarks  | 130        |
| 7.2                     | Possible RMD applications   | 133        |
| 7.3                     | Recommendations   | 134        |
| <b>Appendices</b>       |   | <b>137</b> |
| Appendix A              | Modal damping models  | 138        |
| Appendix B              | Improved LVE Rocol fluid model  | 141        |
| Appendix C              | Linear viscoelastic damping materials                                   | 145        |
| Appendix D              | Thermal effects   | 152        |
| Appendix E              | RMD design with two degrees of freedom                                  | 155        |
| <b>References</b>       |   | <b>159</b> |
| <b>Woorden van dank</b> |   | <b>169</b> |
| <b>Curriculum Vitae</b> |   | <b>171</b> |





# Introduction

**Abstract** - This chapter introduces the research objective of this thesis, which focusses on bandwidth limitations of high-precision motion stages. A brief overview is given regarding the history of IC production and the application of motion stages in this field. Performance limiters are listed, of which one is elaborated in this thesis. Specifically, the performance limiting behavior of the stage's mechanical design in terms of flexible modes and the relation with the modal damping of these modes is studied. Subsequently, the goals of the thesis are listed and research objectives are defined in order to structure the problem and present sub problems. Finally, the outline of the thesis is presented and the relations between the topics are visualized in a table.

## 1.1 IC production and lithography

In 1958, the first functional integrated circuit (IC) was presented and in the years afterwards the applications for these types of circuits grew enormously. Already in 1965, Gordon E. Moore wrote an article in which he predicted the increase of functionality of integrated circuits for the next decade [61]. This prediction estimated the miniaturization factor of components on integrated circuits, which proved to be correct, and after 1975, this observation became driving in further miniaturization. Nowadays, the idea behind 'Moore's law' is such widespread that planning trajectories for the development of these components were – and often are – based on this observation instead of technological possibilities and difficulties [62,80]. In this way it might be seen as a self-fulfilling prophecy. Since the publication by Moore, many publications have elaborated upon the difficulties in maintaining the miniaturization rate over time [45,56,73] and the new possibilities that have been developed to satisfy this prediction [96]. The miniaturization of ICs lead to 1) an increase of functionality per volume, and 2) a decrease in energy consumption per IC operation. In addition to the continuous miniaturization, 3) the cost price per integrated circuit has tremendously decreased, which enabled to implement these devices in a large part of industrial machines and consumer products.

The key production step determining the performance of ICs is the projection of the functional pattern on the surface of a substrate. The substrate is a thin round silicon disc called wafer.

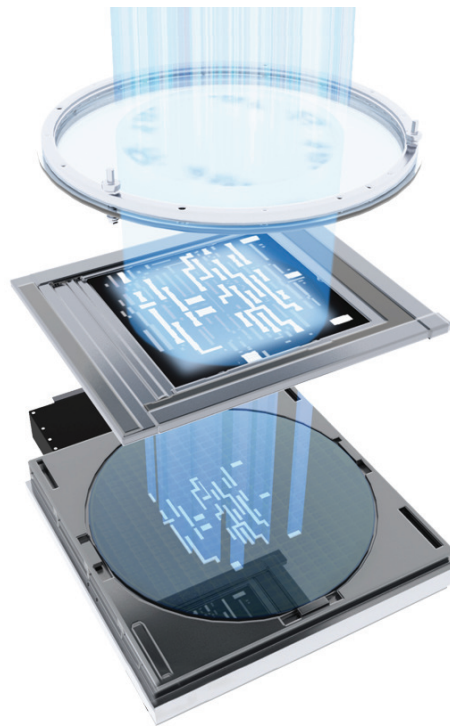


Figure 1.1: Image of the illumination process. The light beam subsequently passes: optical components to condition the light; the reticle which contains the pattern to be projected and, finally, illuminates the pattern on the surface of the wafer.

The functional pattern of an IC is projected in a scanning motion in a machine that is called a wafer scanner. See Figure 1.1 for an impression of the illumination process. The smallest feature size that can be produced is related to the wavelength of the light and the accuracy of the wafer scanner. These properties, therefore, determine the miniaturization rate. The scanner's throughput is related to the scanner's speed and therefore to the production cost of an IC.

The quality of the projected pattern is mainly a function of:

- the quality of the optical system, which includes 1) the light source in which the used wave length is important, 2) the optical path and the components that are applied in the optical column, 3) abilities to adapt the projection pattern by optical corrections and 4) the quality of the projection surface and the 5) properties of the photosensitive resist, and
- the accuracy of the motion system that takes care of the positioning of the wafer (and reticle, with the original image) with respect to the optical column.

The maximal throughput is mainly limited by:

- the sensitivity of the resist with respect to the applied wavelength of the projection light and, therefore, by the output power of the light source, and
- the velocity of the motion system and the achievable accelerations and related settling times.

The second points for both projection quality and throughput are related to the motion stage's performance and are further subject of this thesis.

## **1.2 Motion stages**

The performance of high-tech motion systems improved significantly during the past decades. Especially, in the field of lithographic systems, very fast and accurate motion stages have continuously been developed:

- the accelerations and velocities have been increased,
- the accuracies have been increased,
- the wafer diameter and therefore the wafer area has been increased.

It is expected that these trends will continue in the future. To enable these developments, the complexities of the systems have manifold during the past decades. Roughly 3 decades ago, a wafer scanner contained:

- a single level wafer stage with three in-plane position control loops,
- a single DoF controlled reticle stage.

Nowadays, this device contains:

- a serial double wafer stage principle with both stages fully position controlled (12 loops),
- a serial double reticle stage principle with both stages fully controlled (12 loops).

With all functionality included, over 40 simultaneously operating position control loops are present in a modern wafer scanner. The points above clearly show the increasing importance of the position control systems in the performance.

A high-precision motion system exists of a mechanical stage part, which accommodates for force actuators and position sensors. The acceleration forces are mainly created by an amplifier, with a setpoint trajectory and a feedforward control path. The system's stabilization and robustness against disturbances is provided by feedback control: position measurements enable to calculate position errors and apply actuator forces to suppress these errors. The higher the controller gain can be designed the smaller the position error due to low-frequency disturbances will be. This principle is known as high gain feedback.

### 1.3 Performance limiters

The controller gain in practical cases is limited by several factors:

- limitations in actuator forces and amplifier currents,
- the finite accuracy of the sensors,
- the presence of time delays,
- the presence of flexible dynamics in the mechanical components.

Especially, the presence of flexible stage dynamics is becoming more and more limiting for the performance. The natural frequencies of motion stages are designed as high as possible to enable high controller gains. Materials with high specific stiffness and low density enable these high frequencies. In future stage designs however, the mechanical design for high natural frequencies will be increasingly difficult: the stage accelerations have to increase further to enable larger throughputs. In case of larger actuator sizes the stage mass increases and more energy will be dissipated, which causes thermal problems. A decrease of the stage mass enables to obtain large accelerations, however, without decreasing the stage's outer dimensions, it limits the amount of structural material that can be distributed in the design phase and decreases the stage's static stiffness. This approach makes it more difficult to obtain high natural frequencies. An additional drawback in these types of precision designs is the low damping present at these frequencies. The prevalent materials for these applications contain low material damping and interfaces are designed with low damping, hysteresis and friction.

The resulting resonances can be counteracted by increasing the controller complexity with notch filters, however, the controller complexity is usually restricted by implementation limits and robustness problems at high frequencies. In addition, over-actuation and over-sensing can be applied in order to make non-rigid modes observable and controllable. These active

solutions however, lead to complex controllers and are able to cause unstable behavior of the closed-loop system.

#### **1.4 Thesis goals**

The goal of this thesis is to explore mechanical design in order to adapt the dynamical behavior in such a way that the stage becomes better controllable. The hardware for control is considered to be fixed to enable comparison between different plants. The hypothesis is that the performance of the motion system can be increased by increasing the modal damping of the non-rigid body modes by making use of passive (local) added mechanical dampers. Such dampers change the dynamics of the original system and, therefore, the resulting natural frequencies and mode shapes differ from the original ones. In case of relatively small damper masses however, most new frequencies and mode shapes are highly comparable to the original ones, except for the damping, which has been substantially increased. The idea in this thesis is to apply large damping values in these passive dampers. This results in broad band damping of the mode shapes. This solution is inherently stabilizing the system due to the principle of energy dissipation.

To enable investigation of the performance of a motion stage, firstly, a dynamic model of the stage is created and frequency responses are visualized. In this thesis, one of the most important assumptions is that the controller structure is fixed. This assumption allows investigating the performance increase that can be reached by adapting the plant characteristics. Design-specific performance limiting behavior is evaluated from a feedback control point-of-view. Secondly, the mechanical (passive) dampers are added to the stage model to improve the performance. The positions for these dampers is determined and properties for practical elaboration are included. Thirdly, the performance of the stage for one direction of motion is optimized.

Different levels of motion stage elaboration are shown in this thesis. Simple and abstracted stage models are used to illustrate the solution principle. In addition, complex motion stage designs are subject to performance optimization procedures with practical constraints included. Both open-loop and closed-loop improvements are shown to prove the value of the approach for realistic stage designs.

To meet the research goal, the following objectives are formulated:

##### **1. Development of broad banded damping devices**

Investigation of the ability to suppress resonances in a broad-banded manner by passive damping devices. These devices should contain robust behavior to be able to suppress more than one resonance.

## **2. Investigation of practical limitations**

Investigation of the practical limitations that arise due to differences between ideal theoretical dampers and an elaborated damper design. Realistic material properties have to be included to account for the difference in performance.

## **3. Performance optimization for full complexity motion stage designs**

Both open-loop and closed-loop performance optimization criteria have to be determined and optimization criteria have to be formulated in order to maximize the performance for full complexity motion stage designs.

## **4. Experimental validation**

Implementation of specific damper designs on motion stage experimental setups in order to validate the improvement factors and compare the theoretical improvements with the experimental results.

### **1.5 Outline**

The main content of this thesis is split into five chapters, which deal with the following topics:

Chapter 2 describes a concept to increase the modal damping of an abstracted motion stage over a broad frequency range and the term robust mass damper is introduced. Closed-loop improvements are demonstrated based on open-loop analysis with ideal dampers. The ability to create these robust mass dampers is proven by a test setup based on an ultra-high viscosity fluid.

A closed-loop performance criterion is presented in Chapter 3, based on the stage and damper models introduced in Chapter 2, and an iterative approach is elaborated which enables to improve closed-loop behavior. This chapter provides insight in the bandwidth limiting resonances and an approach to estimate the obtainable improvement factor.

Chapter 4 presents linear viscoelastic (LVE) characterization of the viscous fluid applied in Chapter 2 to estimate the frequency dependent material behavior more accurately. The damper setup presented in Chapter 2 is adapted to enable both fluid characterization and validation of the obtained models. For practical implementation, a multi-mode Maxwell model has been derived.

The fifth chapter describes the mechanical design of a complex motion stage with realistic natural frequencies. Optimal damper locations are investigated to obtain maximal resonance suppression. Subsequently, an open-loop optimization criterion is formulated to maximize the suppression of resonances in a specified frequency range. The LVE damper model as obtained in Chapter 4, is applied in this analysis to calculate realistic improvement factors. The analytical results are verified by experimental validation of the stage with dampers added.

Closed-loop performance optimization of a 6 DoF position controlled prototype motion stage setup is described in Chapter 6. Design parameters for the dampers including the LVE fluid

model obtained in Chapter 4, and controller parameters are combined in a global optimization formulation to improve the behavior of the single-input single-output (SISO) control loop in z-direction. The resulting parameters are used to elaborate the damper design. Experimental validation is provided by identification of the undamped and damped stage and, subsequently,

Table 1.1: Overview of the subjects included in this thesis, arranged by topic.

| Subject                      | Chapter number |   |   |   |   |            |
|------------------------------|----------------|---|---|---|---|------------|
|                              | 2              | 3 | 4 | 5 | 6 | Appendices |
| <b>Theory</b>                |                |   |   |   |   |            |
| Open-loop damping analysis   | ✓              |   |   | ✓ |   |            |
| Closed-loop damping analysis |                | ✓ |   |   | ✓ |            |
| Fluid characterization       |                |   | ✓ |   |   | ✓          |
| LVE damper model             |                |   | ✓ | ✓ | ✓ |            |
| Iterative approach           |                | ✓ |   |   |   |            |
| Optimization approach        |                |   |   | ✓ | ✓ |            |
| <b>Experiments</b>           |                |   |   |   |   |            |
| Robust damping               | ✓              |   |   |   |   |            |
| Fluid measurements           |                |   | ✓ |   |   | ✓          |
| Open-loop improvements       |                |   |   | ✓ |   |            |
| Closed-loop improvements     |                |   |   |   | ✓ |            |

high performance controllers are implemented to validate the gain in performance of the stage. Theoretical results are compared with the experimental results to complete the validation.

Finally, the main conclusions will be summarized in Chapter 7 and recommendations for future research will be given.

Table 1.1 presents the different topics included in this thesis and shows in which chapter these topics are described.

The five main chapters in this thesis are based on papers which are partially published and submitted. Therefore, they can all be read independently. This induces that, especially introductory parts, contain overlapping information. This is especially the case for Chapters 2 and 3, in which the abstracted stage model and modelling steps are similar. The approach to gain improvement however, is different in these two chapters: open-loop versus closed-loop analysis. In addition, Appendix C is in preparation for publication.





# Robust Mass Dampers and Broad Banded Damping

**Abstract** - In high tech motion systems, the finite stiffness of mechanical components results in natural frequencies which limit the bandwidth of the control system. This is usually counteracted by increasing the controller complexity by adding notch filters. The height of the non-rigid body modes in the frequency response function and the amount of damping significantly affect the achievable bandwidth. This chapter describes a method to add damping to the flexible behavior of a motion stage, by using robust mass dampers which are mass-spring-damper systems with an over-critical damping value. This high damping results in robust dynamic behavior with respect to stiffness and damping variations for both the motion stage and the damper mechanisms. The main result is a significant increase in modal damping over a broad band of resonance frequencies. For the decoupled frequency response functions in  $z$ -direction with a  $PID^+$  controller applied, this results in a bandwidth improvement of over 150%, which leads to a disturbance suppression of over 10 times for both force and displacement disturbances. A damper test setup has been realized and tested to validate the possibility to create dampers with such large damping values in a relatively small volume.

## 2.1 Introduction

In the industry of high-end manufacturing, for instance in the semiconductor market, various processing and measurement steps take place using positioning tables or stages. The throughput of these systems is directly related to the accelerations and velocities of the motion system. The functional density of the product, in other words, the minimum feature size, is related to the accuracy of the motion system. Both throughput and accuracy lead to conflicting requirements for the motion stage: high accuracies in combination with high accelerations. A positioning table is part of a system, in which mechanics, electronics, a control system, a measurement system and an actuation system have to work together properly for optimal performance [97]. In case of motion systems, the combination of the control system and the dynamics of the mechanical design often limits the performance of the system [16]. As long as accurate sensors are available and operating frequencies of the electronic subsystems are orders of magnitude higher than the natural frequencies of the mechanical system and, if the actuators are chosen correctly with respect to the motion task, these components may not limit the performance of the system. For now, assume the electronics, measurement system and actuators to be perfect, which leaves the combination of the mechanics and the control system to be analyzed in more detail. For such situations the motion system can be seen as a mechanical device with position measurements and force actuators. After decoupling into a preferred coordinate system, standard PID-type controllers are able to stabilize such a motion system. In practice however, more complex controller components, such as notch filters, are implemented to deal with the non-rigid body (NRB) dynamics [86]. A drawback of notch filters is that the robustness often becomes a point of concern: in case of shifting natural frequencies, the notch filter is not placed correctly anymore and the closed-loop stability of the system may become questionable. The amount of structural damping at the resonance frequencies determines the achievable bandwidth to a certain extent. However, high-precision designs often lack damping: monolithic stages have few mechanical connections, materials like aluminum or ceramics and vacuum environments devoid of squeeze film damping contribute to this property.

Many methods have been investigated to add damping to mechanical systems, components or materials. Materials have been developed that inherently display a high damping coefficient. External damping mechanisms are designed: passive examples are constrained layer damping and squeeze film damping [40]. An active solution is the use of additional actuators and sensors to make flexible behavior observable and controllable [82,105]. In some applications, structural mass is exchanged by additional actuators to provide active damping [74]. Although the damping can be increased, often a substantial stiffness decrease is resulting, which counteracts the advantages obtained by the damping increase.

This chapter proposes to make use of a few mass-spring-damper systems with over-critical damping values, to add broad band damping to the higher order out-of-plane dynamics of relatively flat positioning stages. The contributions of this chapter are to provide a design method and solution which has the following properties:

- create broad band damping to mechanical resonances,

- enable performance increase in z-direction (out-of-plane),
- increase the plant robustness.

Section 2.2 briefly introduces the traditional tuned mass damper concept. In Section 2.3 a simplified stage model with low modal damping is presented. A controller is designed and the performance of the system determined. Section 2.4 introduces the stage model with dampers added and the damping increase and performance increase is investigated. In Section 2.5 the performance increase in z-direction is presented in the frequency and time domain. Section 2.6 shows the results in the rotational  $\varphi$ - and  $\psi$ -direction of the motion stage due to the increase in modal damping. Section 2.7 presents the robustness increase of the plant. A mechanical design of a damper is discussed in Section 2.8 and measurements are presented. Finally, Section 2.9 enumerates the conclusions.

## 2.2 Tuned Mass Dampers

One way to add damping to a specific resonance frequency of a mechanical structure with low damping is by applying a tuned mass damper (TMD), as for instance described in [25]. A tuned mass damper is a passive device, consisting of a structural mass  $m$  mounted on a spring and damper in parallel. See Figure 2.1a and Figure 2.1b. Mass  $M$  represents the main structural mass and  $m$  represents the added mass of the TMD. The effectiveness of the TMDs is related to the mass ratio between  $m$  and  $M$ . To obtain a substantial suppression factor in combination with a relatively small increase in mass, the mass ratio is usually determined to be approximately 5-10 % of the main structural mass. The undamped natural frequency of the TMD is a function of the mass and stiffness of the TMD and has to be tuned close to the targeted natural frequency of the main structure. Subsequently, an amplitude reduction of the

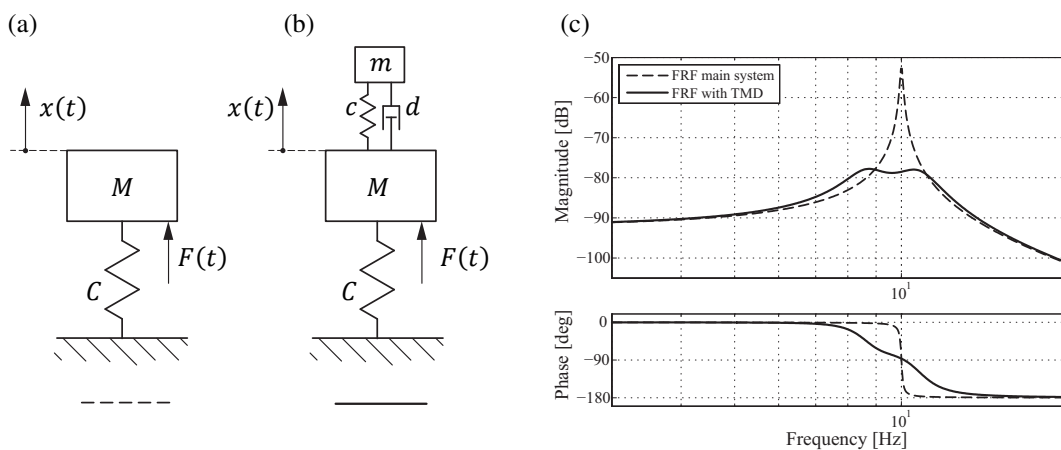


Figure 2.1a: Main structural mass model with force actuation  $F(t)$  and position measurements  $x(t)$

Figure 2.1b: Main structural mass with a TMD added to reduce the vibration amplitude

Figure 2.1c: Bode diagrams of the undamped and the damped system indicated with the dashed line and continuous line, respectively. The corresponding parameter values are a main mass  $M$  of 10 kg and a TMD mass  $m$  of 0.75 kg.

main structure is achieved at the resonance frequency by adjusting the correct amount of TMD damping, see Figure 2.1c. Equations for optimal stiffness and damping values can be found in [25]. A drawback of the TMD is the relatively large sensitivity of the suppression factor for variations in stiffness and damping values. An analysis and design method to deal with this sensitivity is presented in [109]. This sensitivity also holds for natural frequency variations of the main structure. The overall system performance will be strongly affected by parameter variations of the dynamics. One can think of variations caused by wear, temperature variations, varying frictions and position dependent natural frequencies of moving mechanical components. TMD's are well-understood and have proven to be useful in a widespread field of applications, for instance: automotive industry, buildings and structures, airplanes, machine frame designs and space structures, see for instance [34,46,72]. Different types of TMD's exist, depending on the field of application. In addition, more complex TMD configurations are investigated to achieve an efficiency increase per unit of damper mass [111]. Although TMD's are often designed as passive devices, also semi-active [53] and active variants are described [70]. A comparison between passive and active dampers can be found in [44]. A method to add damping within a frequency band with multiple TMD's is shown in [107]. A main advantage of the TMD damper configuration is that these structures do not introduce reaction forces in the machine frame. Notice that for all the mentioned applications of TMDs, the effects are always intended for damping of one specific frequency of the structure. This is what is different to the broadband method proposed in this chapter. To this end, a TMD with an over-critical damping has been developed and this device is called Robust Mass Damper (RMD). Before the details of such an RMD are described, firstly, the stage dynamics of motion systems have to be addressed.

## 2.3 The undamped stage model

### 2.3.1 Abstracted stage model

The goal of this chapter is to investigate and adjust the out-of-plane vibrational behavior of a motion stage with relatively large length-height-ratio. Especially, the bandwidth limiting high-frequency dynamic behavior is of interest. The most simple and abstracted three-dimensional model of such a table is a square plate. A characteristic property of a thin plate is the presence of mode shapes with relatively large out-of-plane displacements. The first three non-rigid-body (NRB) modes are presented in Figure 2.2: a) torsion mode, b) saddle mode

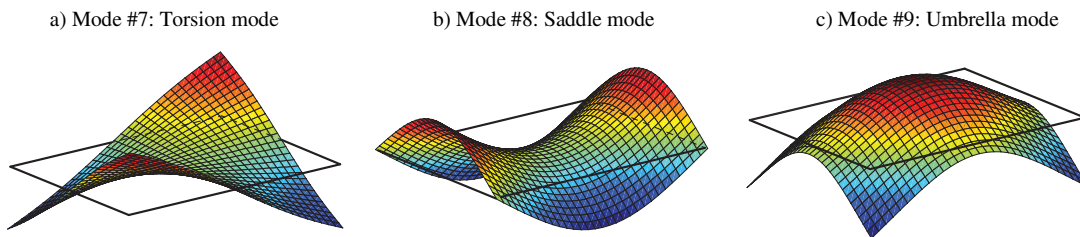


Figure 2.2: First three non-rigid body mode shapes of a square plate in order of appearance.

and c) umbrella mode, respectively. As model, an aluminum plate with dimensions of  $600 \times 600 \times 10 \text{ mm}^3$  is created and a modal analysis is performed. 3D shell elements are applied and subsequently the plate's free and undamped natural frequencies and corresponding mode shapes are calculated using NX 7.5 equipped with the NX Nastran<sup>®</sup> solver module. From the results of the modal analysis, the displacements of the first hundred mode shapes and the corresponding natural frequencies are exported, including the 6 Rigid-Body (RGB) modes. These RGB modes appear as low-frequency modes without deformation. The exported displacements are used to create a dynamic model of the plate in state space modal-1 description. The modal-1 description [33] is preferred because the modal-3 description results in larger condition numbers resulting in worse numerical accuracy for high frequencies. A modal damping of 0.003 is applied to the model, which is an experimentally determined damping value for a precision design operating in atmospheric conditions. The dynamic model and post-processing scripts are created in Matlab<sup>®</sup>. This model is further referred to as undamped model:

$$\dot{x} = Ax + Bu \quad (2.1)$$

$$y = Cx + Du \quad (2.2)$$

$$A = \begin{bmatrix} 0 & \Omega \\ -\Omega & -2Z\Omega \end{bmatrix} \quad B = \begin{bmatrix} 0 \\ \Phi B_{input} \end{bmatrix} \quad (2.3)$$

$$C = \begin{bmatrix} C_{outp\_q} \Phi \Omega^{-1} & 0 \\ 0 & C_{outp\_v} \Phi \end{bmatrix} \quad D = [0] \quad (2.4)$$

Matrix  $A$  contains the natural frequencies of the plate and its dimensions are  $(2 \cdot n_{modes} \times 2 \cdot n_{modes})$ . Matrix  $B$  is the input matrix with dimensions  $(2 \cdot n_{modes} \times n_{inputs})$  and matrix  $C$  is the output matrix with dimensions  $(n_{outputs} \times 2 \cdot n_{modes})$ . Matrix  $D$  is the direct throughput matrix and has dimensions  $(n_{outputs} \times n_{inputs})$ . Diagonal matrix  $\Omega$  contains the natural frequencies of the plate and diagonal matrix  $Z$  contains the modal damping values corresponding to these natural frequencies. The modal damping value amounts 0.003 for all resonances of the plate model. Matrix  $\Phi$  contains the mode shape displacements of the plate, calculated by FEM. Matrix  $B_{input}$  lists the nodes that are necessary as input, for both RMD's and actuators. Matrices  $C_{outp\_q}$  and  $C_{outp\_v}$  list the displacement ( $q$ ) and velocity ( $v$ ) output nodes respectively, for both the RMDs and the position sensors.

### 2.3.2 Actuators and sensors

Actuator and sensor locations are chosen to calculate frequency response functions (FRFs) for controller design purposes. Figure 2.3 presents the plate with the actuator positions, sensor

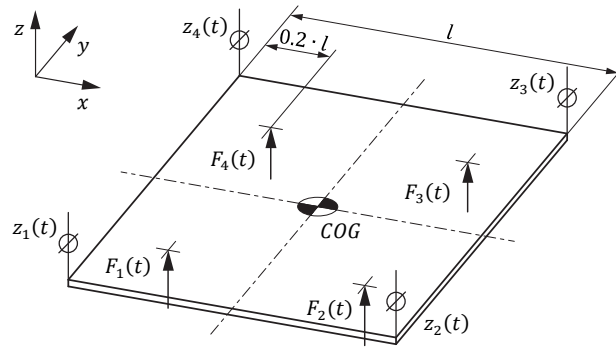


Figure 2.3: The square plate model with the positions of the force actuators ( $F_{1,\dots,4}(t)$ ) and sensor locations ( $z_{1,\dots,4}(t)$ ) indicated.

positions and the center of gravity (*COG*) indicated. The actuators and sensors act in  $z$ -direction. The sensors are placed on the outer edges of the positioning table because the table center is reserved for the process. Therefore, four position sensors are assumed to be present on the stage's corners. The actuator positions are located on the plate diagonals at  $0.2 \cdot l$  from the plate's edges. This is approximately the distance that minimizes the static deflection of the stage and is therefore often used in practical designs. For the investigation of bandwidth limitations it is of importance to note that the actuator and sensor positions are placed in a non-collocated configuration. The actuators are modeled as force inputs. These force inputs are specified in input matrix  $B_{input}$  (2.3) and the sensors are modeled as displacement outputs and are specified in output matrix  $C_{outp\_q}$  (2.4).

$$T_u = \begin{bmatrix} 1 & 1 & 1 & 1 \\ x_{a,1} & x_{a,2} & x_{a,3} & x_{a,4} \\ y_{a,1} & y_{a,2} & y_{a,3} & y_{a,4} \\ \Phi_{a,1}^{NRB,1} & \Phi_{a,2}^{NRB,1} & \Phi_{a,3}^{NRB,1} & \Phi_{a,4}^{NRB,1} \end{bmatrix}_{COG}^{-1} \quad (2.5)$$

$$T_y = \begin{bmatrix} 1 & y_{s,1} & x_{s,1} & \Phi_{s,1}^{NRB,1} \\ 1 & y_{s,2} & x_{s,2} & \Phi_{s,2}^{NRB,1} \\ 1 & y_{s,3} & x_{s,3} & \Phi_{s,3}^{NRB,1} \\ 1 & y_{s,4} & x_{s,4} & \Phi_{s,4}^{NRB,1} \end{bmatrix}_{COG}^{-1} \quad (2.6)$$

### 2.3.3 Decoupled transfer functions

A geometrical decoupling procedure with respect to the center of gravity of the plate is applied to obtain a plant transfer function matrix in which the rigid body behavior dominates at the diagonal components. This approach enables to apply diagonal controller design for the plants at the diagonal components. In this case, the  $z$ -,  $\varphi$ - and  $\psi$ -directions are decoupled,

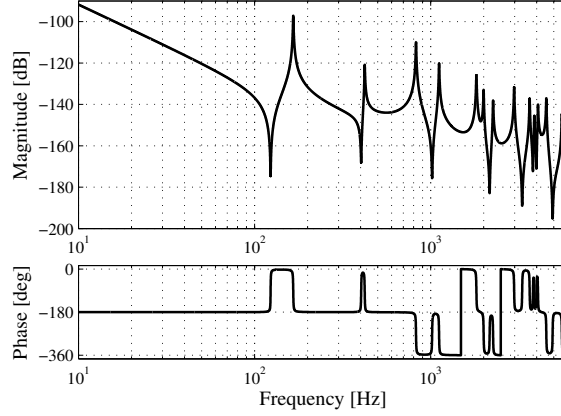


Figure 2.4: Bode diagram of the SISO frequency response function of the undamped plate in z-direction, obtained by geometrical decoupling around the center of gravity.

which represent the vertical direction of motion and the rotations around the horizontal  $x$ - and  $y$ -axis, respectively. In addition, the four actuators and sensors in  $z$ -direction enable to decouple the first non-rigid body DoF, which is the torsion mode for this plate. A figure of the torsion mode is presented in Figure 2.2a. The coordinates of actuators and sensors are used in decoupling matrices  $T_u$  (2.5) and  $T_y$  (2.6) to decouple the RGB modes. Components from the mode shape matrix ( $\Phi$ ), corresponding to the position of the actuator and sensor nodes, are used to decouple the torsion mode. In the resulting transfer function matrix, the diagonal terms are dominant for low frequencies. This phenomenon allows implementation of a diagonal controller matrix, preferably obtained by sequential loop closing: controllers can be designed for the separate loops independently and as a result performance can be determined independently for every decoupled loop. For this chapter, the focus is mainly on the transfer function in  $z$ -direction, of which the SISO frequency response function is shown in Figure 2.4. This FRF behaves collocated for the first two zero-pole-combinations. The phase drops to  $-360$  deg at the third resonance due to the actuator and sensor positions and the FRF becomes non-collocated. This behavior finally limits the bandwidth of the control system. The bandwidth is defined as the first top-down crossing of the 0 dB open-loop gain.

#### 2.3.4 Controller design

This chapter describes an improvement of a motion system's dynamical behavior. Firstly, a definition of performance has to be stated in order to quantify improvements. In this chapter, the performance indicator is defined as the bandwidth. This choice is justified by the relation between bandwidth and disturbance suppression and the ability to track setpoints. Closed-loop performance is evaluated using controllers of equal order to make plants comparable. In this chapter, relatively simple controllers are applied containing the following components:

- gain,
- integrator,



- lead filter,
- 1<sup>st</sup> order low-pass filter.

The combination of gain and lead filter stabilizes the system by creating a defined 0 dB crossing. An integrator is added to increase the realism of the analysis: the low-frequency open-loop gain is increased to suppress steady-state errors and the achievable bandwidth is restricted by the additional phase lag. For comparison reasons, the zero of the integrator is placed exactly at 1/5th of the bandwidth. A low-pass filter is added to create high-frequency roll-off. Figure 2.5a shows the Nyquist diagram and Figure 2.5b shows the open-loop FRF of the undamped plate. A modulus margin of 6 dB which is the peak value of the absolute sensitivity function, is used as design criterion. The resulting bandwidth is 28 Hz. The bandwidth-limiting resonances are visible in the Nyquist diagram. The first resonance around 160 Hz is not limiting, in contradiction to the resonances between 400 Hz and 2000 Hz. This range is indicated in the Bode diagram of Figure 2.5b. Note that the large amplification factor at the resonance frequencies is caused by the low modal damping that is included in the dynamic model.

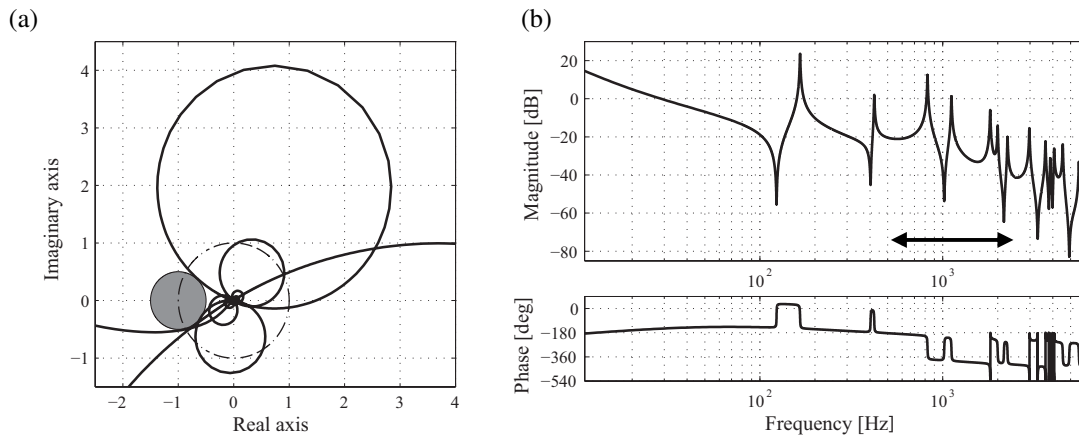


Figure 2.5a: Nyquist diagram of the open-loop of the undamped plate. The robustness margin of 6 [dB] is indicated by the grey circle and the bandwidth is indicated by the dotted line.

Figure 2.5b: Bode diagram of the open-loop of undamped plate with the range of bandwidth limiting dynamics indicated by the arrow.

## 2.4 The damped stage model

### 2.4.1 The damper model

To increase the modal damping and suppress the amplification of the resonances, dampers are added to the stage model. Caused by the presence of BW limiting behavior, the dampers are dimensioned to influence this behavior: especially in the frequency range between 400 Hz and 2 kHz. The damper consists of a mass, mounted to the plate model by a spring and dashpot placed in a parallel configuration. The RMD model is shown in Figure 2.6.

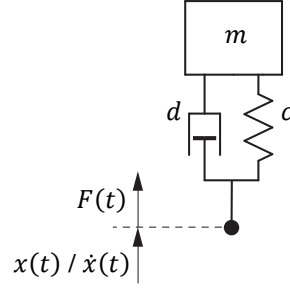


Figure 2.6: Dynamic model of the RMD with displacement and velocity inputs  $x(t)$  and  $\dot{x}(t)$  respectively, and force output  $F(t)$ .

Equations (2.7) and (2.8) show the system matrices of the nodal state space description of the damper:

$$A_{RMD} = \begin{bmatrix} 0 & 1 \\ -c/m & -d/m \end{bmatrix} \quad B_{RMD} = \begin{bmatrix} 0 & 1 \\ c/m & d/m \end{bmatrix} \quad (2.7)$$

$$C_{RMD} = [c \quad d] \quad D_{RMD} = -[c \quad d] \quad (2.8)$$

Matrix  $A_{RMD}$  contains the system properties or, describes the velocity and acceleration of the damper mass (damper states) as result of the displacement and velocity of the RMD mass. Matrix  $B_{RMD}$  describes the contribution of the input displacement and velocity to the damper states. Since the RMD is added to the plate, the reaction force of the RMD has to be calculated and fed back into the plate. Matrices  $C_{RMD}$  and  $D_{RMD}$  describe this part of the system, which results in output  $y$ : the damper reaction force acting on the plate.

#### 2.4.2 The damped plate model

Four damper models with equal parameter values are connected to the plate corners in order to preserve the stage symmetry. This is favorable in case of geometrical decoupling as discussed in Section 2.3.3. The specific resonances which limit the bandwidth of the system have relatively large displacements at the plate corners and therefore higher velocities are present there. These positions were hence chosen to connect the dampers to. Figure 2.7 presents the plate with four dampers added in  $z$ -direction. With respect to the RMD mass  $m$ , a tradeoff has to be made: a relatively large mass enables to influence the plate dynamics heavily. On the other hand, large RMD masses contribute significantly to the overall stage mass: therefore, it decreases the acceleration rate of the positioning table (if the actuators and electronics are assumed unchanged). Firstly, the RMD masses are determined at 0.35 % of the plate mass to avoid a large mass increase: the total mass increase is  $< 1.5$  % of the plate mass. Substantial damping can be added to a range of resonance frequencies with these amounts of

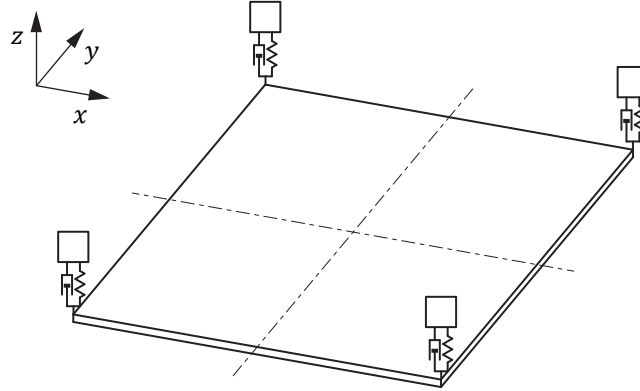


Figure 2.7: Model of a square plate with 4 dampers added on the corners. The DoF of the dampers is in  $z$ -direction. The four dampers have equal mass, damping and stiffness.

mass added. Secondly, the natural frequencies of the dampers are tuned equally around the lowest resonance frequency of the motion stage by tuning the stiffness parameter  $c$ . As last parameter, the damping value  $d$  should be determined. Figure 2.4 showed a Bode diagram of the SISO  $z$ -component of the plant without dampers. Figure 2.8 shows an extension of Figure 2.4 with an additional parameter: the RMD damping value.

The dampers are included in the dynamic model and the SISO frequency responses are

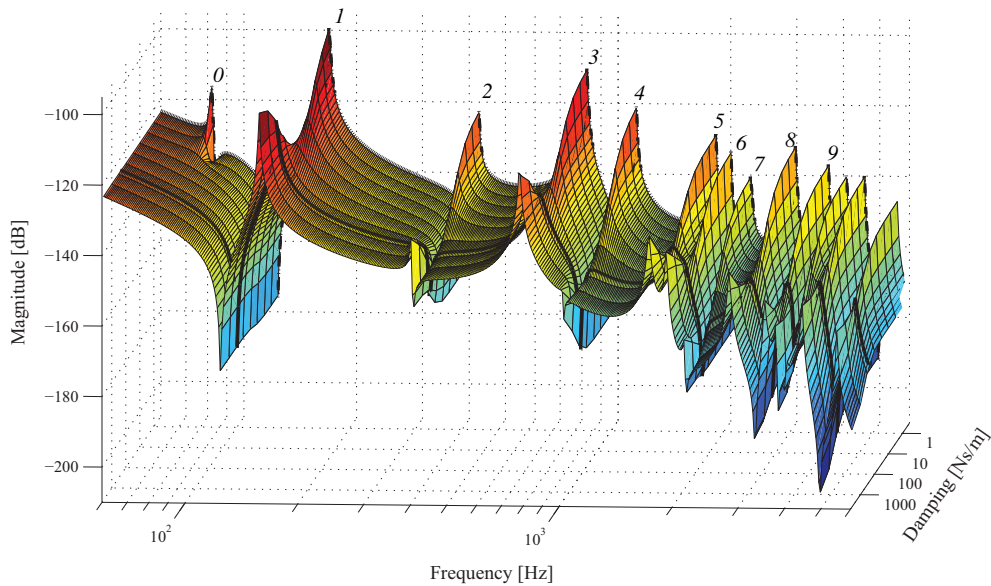


Figure 2.8: A 3-dimensional Bode diagram of the decoupled frequency response function in  $z$ -direction.

Only the magnitude part is shown. The additional axis shows the influence of the RMD's damping parameter on the dynamic behavior of the plant. The first nine visible plate resonances in this FRF are indicated by the numbers 1-9. The dash-dotted line presents the behavior of the stage with dampers with and very low damping value. This introduces additional dynamics at the damper frequency (Resonance 0 @ 90 Hz). The continuous line shows the behavior for a damping value of 250 Ns/m. The RMD dynamics disappears for larger damping values and is not visible in case of the continuous line.

calculated for different damping values. A range of Bode diagrams is shown for different damping values of the dampers. The dashed line shows the behavior of the undamped plant, as shown before in Figure 2.4. In this graph, the undamped plate resonances are visible of which the first nine are numbered. Resonance 0 was not visible in Figure 2.4 and indicates the dynamics added by the dampers itself. This RMD dynamics is visible as a pole-zero combination in the dashed line. This undamped RMD behavior disappears rapidly for higher damping values: for increasing damping values, one can see that the amplification at the resonance frequency is suppressed rapidly. Although for every single stage resonance an optimal damping value can be found, is the optimal damping value different for every resonance. For instance: for an optimal suppression at resonance 1 (@ 160 Hz), the damping should be adjusted to 30 Ns/m. For increasing damping values the suppression is sub-optimal for this resonance.

For bandwidth increase a range of resonances between 400 Hz and 2 kHz has to be suppressed. These resonances are numbered 2 to 6 in Figure 2.8. When looking in more detail, one can observe that resonance 2 and 4 are effectively suppressed in case of larger damping values. Resonance 3, 5 and 6 clearly show an optimal point, which is different for these three resonances. A damping of 250 Ns/m is applied at the dampers: the corresponding behavior is indicated in Figure 2.8 by the continuous line and shows a well-balanced suppression of resonance 3, 5 and 6 and a full suppression of resonances 2 and 4. The amplification of the resonances above 2 kHz is reduced as well, although less than in the frequency range mentioned. Figure 2.9 shows both FRF's again to show the gain difference at the resonance frequencies. The parameters used are listed in Table 2.1.

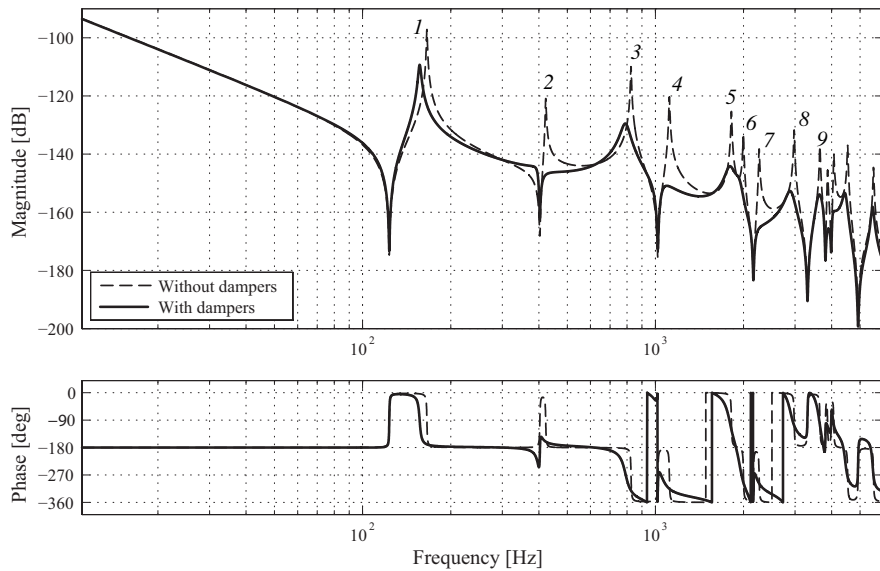


Figure 2.9: Bode diagram of the transfer functions of the plate without dampers and the plate with dampers (250 Ns/m), both in z-direction. These two Bode diagrams correspond to the dashed line and solid line as indicated in Figure 2.8. The resonances are numbered in the same sequence as applied in Figure 2.8.

Table 2.1: Data which correspond to the results shown in Figure 2.9.

|              | Name       | Value      | Unit |
|--------------|------------|------------|------|
| <b>Plate</b> | dimensions | 600×600×10 | mm   |
|              | material   | Aluminium  |      |
|              | mass       | 10         | kg   |
| <b>RMDs</b>  | number     | 4          | -    |
|              | mass       | 35         | g    |
|              | stiffness  | 9700       | N/m  |
|              | damping    | 250        | Ns/m |

### 2.4.3 Verification of the frequency response functions

The frequency response functions resulting from both the undamped model and the damped model are verified by FEM calculations. This enables to check if the coupling procedure between the plate model and the damper models is executed correctly. The dampers are added in the FEM model, with corresponding properties of the dampers added in the state space model. The frequency response functions from actuators to sensors are calculated using fully harmonic calculations, to compute the non-proportional damping in a correct manner and obtain the most accurate result. The resulting frequency response functions are compared with the ones obtained from the state space representation to verify the influence of the damping as function of the excitation frequency. After validation, the state space model is proven to be correct and, subsequently, it can be used in the analysis steps.

## 2.5 Performance improvement in z-direction

The goal of this research was to improve the modal damping of the higher order dynamics, especially between 400 Hz and 2 kHz. The Bode diagram of Figure 2.9 indicates that this goal is achieved based on the resonance amplitude suppression. In addition, the resonances above 2 kHz also display a damping increase.

### 2.5.1 Modal damping increase

To obtain a quantitative measure of the damping improvements, the modal damping of the system poles is calculated and the result is shown in Figure 2.10. The horizontal axis represents the frequency in Hz and the vertical axis represents the modal damping of both plate models on a logarithmic scale. The initial modal damping of 0.003, corresponding to the undamped plate model is indicated by the circles. The modal damping of the plate with dampers is indicated by the crosses. A minor part of the crosses is still on the initial modal damping value of 0.003. These unchanged poles can be divided in two groups. The first group comprehends the in-plane mode shapes of the plate. The four dampers are not able to add damping to these resonances, because the plate displacement is perpendicular to the damper DoF, i.e., they are unobservable and uncontrollable as seen from the RMDs.

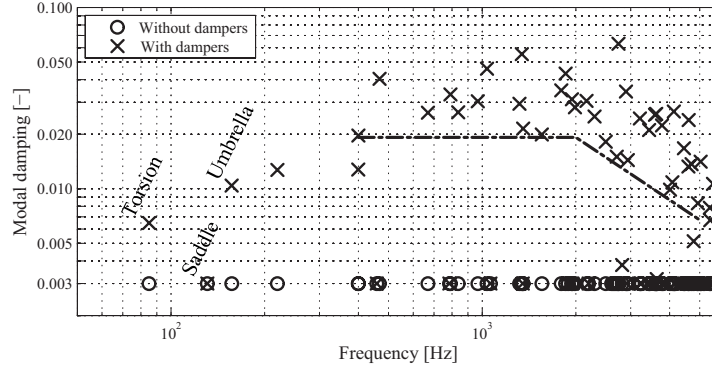


Figure 2.10: This figure shows the modal damping calculated from the system poles as function of the pole frequency. The circles indicate the modal damping of the initial plate. The crosses indicate the damping of the plate with dampers added.

However, these resonances do not appear in the frequency response function in z-direction. The second group of low-damped poles contains the mode shapes that do have displacements in z-direction, however, the displacement amplitudes at the corners are zero. The saddle mode, as shown in Figure 2.2b, is an example of such a mode. These modes do show displacements in z-direction, however, they are not visible in the decoupled frequency response function and are, therefore, not bandwidth limiting. Consequently, these modes are not included in the analysis. The modal damping of the modes visible in the frequency response function in z-direction is increased substantially: between 400 Hz and 2 kHz the modal damping is increased from 0.003 to 0.02. This improvement is indicated in Figure 2.10 and represents a modal damping increase of over 6.5 times.

### 2.5.2 Frequency domain performance

As a result of the increased modal damping, the Nyquist diagram shows a behavior in which fewer resonances limit the bandwidth. This Nyquist diagram is presented in Figure 2.11a and shows the product of the plate with dampers and a controller. The controller designed for this damped plate allows for a gain which is 7 times larger than the controller gain of the undamped plate. Therefore, the bandwidth has increased from 28 Hz. to 74 Hz. This indicates a bandwidth increase factor of 2.6. The resulting open-loop frequency response function shows a 17 dB larger magnitude for low frequencies than in the case without dampers, see Figure 2.11b. The SISO sensitivity functions of the undamped system and the damped system, both in z-direction (i.e.  $1/(1 + P_z(s)C_z(s))$ ) are shown in Figure 2.12a, in which  $s$  is defined as  $j\omega$ . The dashed line represents the behavior of the initial plate without dampers and the continuous line shows the plate with dampers added. This figure shows that the low-frequency disturbance suppression is improved substantially. Note that this low-frequency improvement is realized by taking advantage of the Bode-sensitivity integral. The sensitivity above the bandwidth ( $> 74$  Hz) is enlarged by changing the characteristics of the plant dynamics without crossing the modulus margin limit of 6 dB. The low-frequency part of a sensitivity function can be approximated by  $S_{LF}(s) = 1/P_z(s)C_z(s)$ .

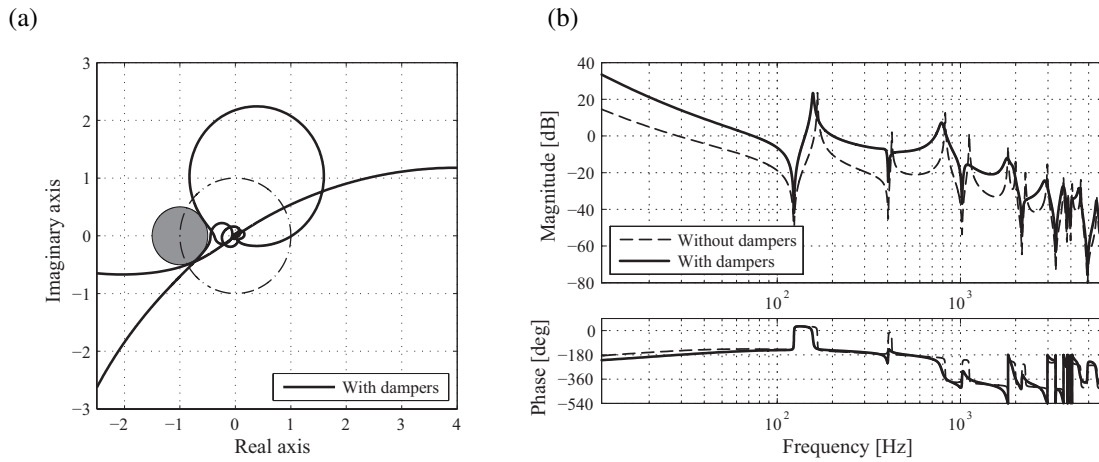


Figure 2.11a: Nyquist diagram of the open-loop of the damped plate. The stability margin of 6 [dB] is indicated, which is used for controller design.

Figure 2.11b: Open-loop Bode diagram of the undamped and the damped plate.

This indicates that the increased controller gain is directly visible in the disturbance suppression, because the difference between the low-frequency plant gains can be neglected (less than 1.5% difference caused by the added damper masses). At frequencies far below the bandwidth, the suppression of displacement disturbances is improved by 22 dB. This means a position error decrease of a factor 12. The process sensitivity,  $S_P(s) = P_z(s)/(1 + P_z(s)C_z(s))$  is calculated to investigate the system performance with respect to the suppression of force disturbances. The corresponding graph is presented in Figure 2.12b. The low-frequency part of  $S_P(s)$  can be estimated as  $S_P(s) = 1/C_z(s)$ , which means that the output error due to low-frequency force disturbances is also improved by 22 dB.

### 2.5.3 Time domain performance

In figure 2.13a, the step responses of both closed-loop systems are shown. The settling time is defined as the time needed to reach a relative servo error less than 10 %. The undamped system settles within 46 ms and the damped system within 17 ms. This means that the damped system reacts 2.7 times faster than the undamped system. Figure 2.13b presents the outputs of both systems in case of a 1 Hz displacement disturbance acting on the system. The magnitude of the output error is improved over 12 times. The tracking error in case of a sinusoidal input on the reference equals this factor ( $Sensitivity + Complementary Sensitivity = 1$ ). Figure 2.13c shows the output reduction in case of a 1 Hz disturbance is applied on the plant input. This improvement ratio is also 12 times.



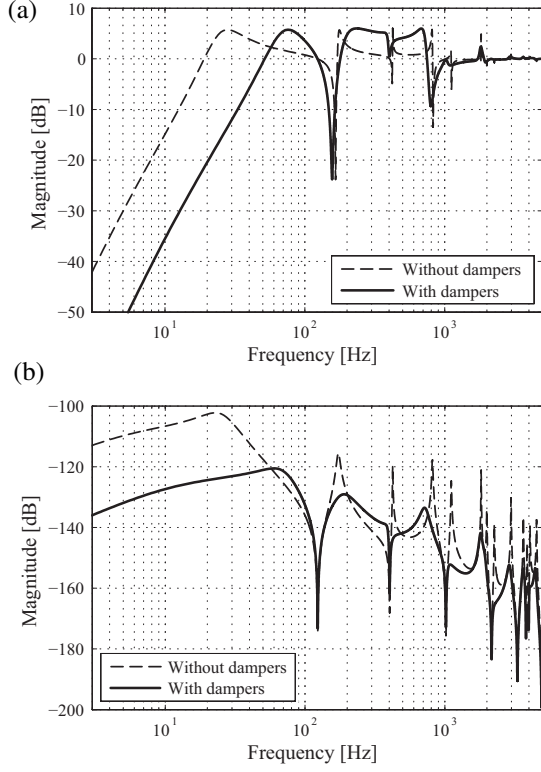


Figure 2.12a: Bode diagram of the sensitivity function.

Figure 2.12b: Bode diagram of the process sensitivity function.

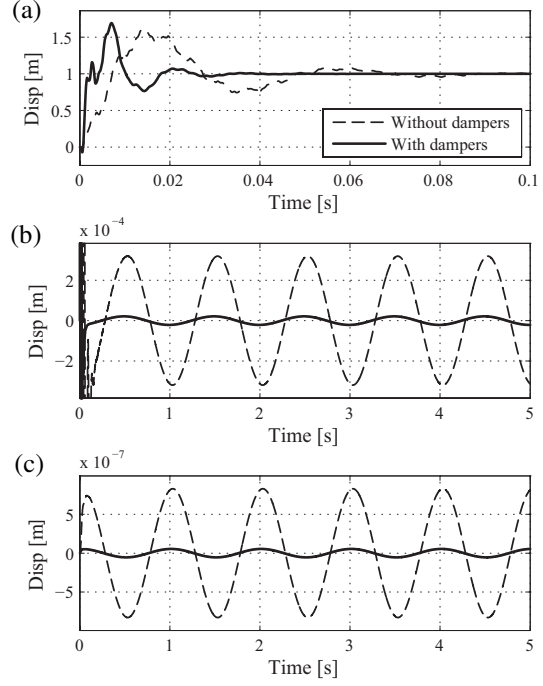


Figure 2.13a: Step response of the closed-loop system.

Figure 2.13b: Output  $y(t)$  in case of a position disturbance  $d_p(t)$  at 1 [Hz] with amplitude 1 [m].

Figure 2.13c: Output  $y(t)$  in case of a force disturbance  $d_F(t)$  at 1 [Hz] with amplitude 1 [N].

## 2.6 Performance improvements in $\varphi$ - and $\psi$ -direction

In the previous section, the results in the translational  $z$ -direction were evaluated. The plate model is equipped with four actuators and four sensors in  $z$ -direction. This enables to investigate the systems rotational behavior around the  $x$ -axis and  $y$ -axis as well. These axes are further indicated as  $\varphi$ - and  $\psi$ -direction, respectively. Figure 2.9 and Figure 2.10 showed that the modal damping is increased for the resonances visible in the  $z$ -direction frequency response functions from actuators to sensors. The decoupled frequency response function in  $z$ -direction as well as the decoupled frequency response functions in  $\varphi$ - and  $\psi$ -direction are linear combinations of these frequency response functions between actuators and sensors. Therefore, the damper influence is also visible in the  $\varphi$ - and  $\psi$ -direction. The decoupled frequency response functions of the plant in  $\varphi$ - and  $\psi$ -direction are similar, caused by the symmetry in terms of plate dimensions and TMD properties as well as in terms of actuator and sensor positions. Therefore, only the  $\varphi$ -direction will be investigated.

The open-loop behaviors of the plate with and without dampers, both in  $\varphi$ -direction, are shown in Figure 2.14. Two controllers are designed and performances determined. The damping increase of the plants and the difference in controller gains are clearly visible. The



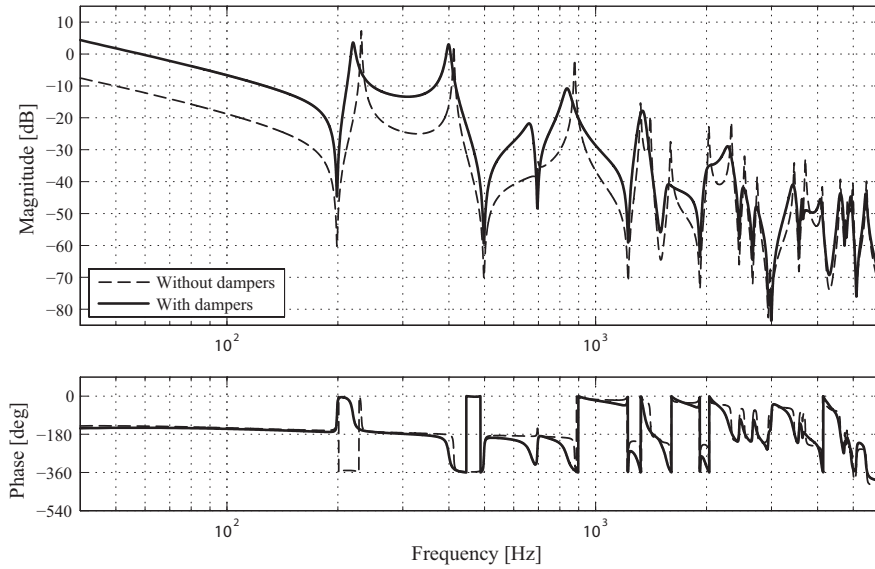


Figure 2.14: Bode diagram of the open-loop frequency response functions in  $\varphi$ -direction.

bandwidth is increased from 20 Hz in the undamped case to 58 Hz in the damped case. This increase is a factor 2.9. Note that although this bandwidth increase is substantial, the increase could be more if the dampers were designed specifically for this frequency response function: the dampers are designed to optimize the performance in  $z$ -direction instead of the  $\varphi$ -direction. In case of the  $z$ -direction the third resonance (around 800 Hz) is mainly limiting the bandwidth in contradiction to the frequency response function in  $\varphi$ -direction, in which the second resonance (around 400 Hz) is mainly limiting. To optimize the suppression of resonances in the  $\varphi$ -frequency response function, the dampers had to be designed to add damping at lower frequencies, instead of the higher frequency band that is desired in  $z$ -direction.

The Bode diagram of the sensitivity and process sensitivity are presented in Figure 2.15. The bandwidth increase improves the low-frequency disturbance suppression with respect to both force disturbances and position disturbances. The improvement factor equals 12 times (22 dB).

## 2.7 Plant robustness increase

The dampers as added in Section 2.4.2 have a relatively high damping value. This robustifies the damper behavior with respect to variations in damping coefficient and natural frequency. This property is contrasting with the sensitivity of a classical TMD w.r.t. parameter variations. In case of a damping increase of 10 % of the dampers, the sensitivity peak increases to 6.06 dB, which is a relative increase of  $< 1$  %. This insensitivity is an advantage with respect to the production of the dampers: in case a damper has a slightly different damping value, it will still work. Although the optimal behaviour will not be achieved, the overall dynamic behaviour is still influenced in a positive way.

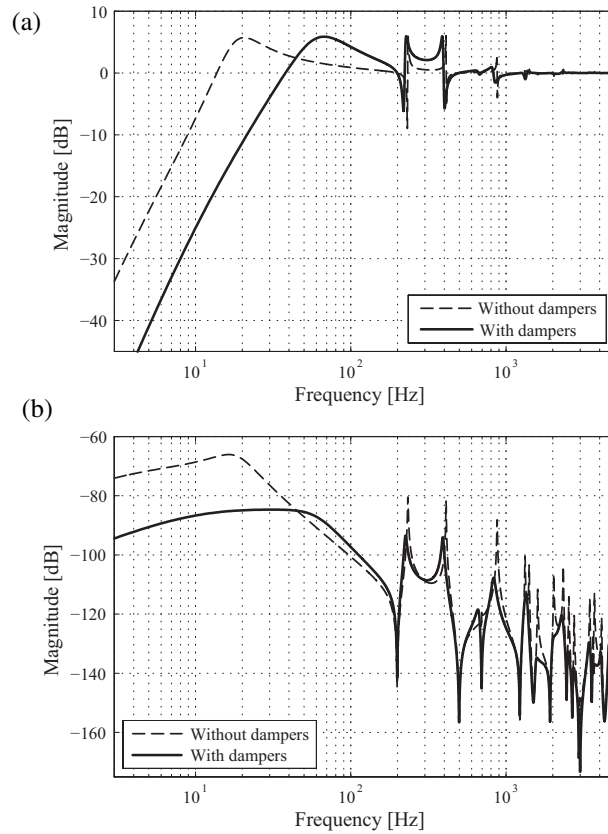


Figure 2.15a: Bode diagram of the sensitivity functions of the plate in  $\varphi$ -direction without and with dampers.

Figure 2.15b: Bode diagram of both process sensitivities in  $\varphi$ -direction.

Figure 2.16 presents the Bode diagram of the sensitivity function of the plate model without dampers and the plate with dampers added. In all previous calculations, the plate modal damping was assumed to be 0.003. To investigate the robustness of the system with respect to plate parameter variations, the modal plate damping is changed to 0.002, which means a decrease in modal damping of 33 %. The same controllers are applied as designed earlier. The dashed line shows the sensitivity function of the undamped plate. The sensitivity peak (modulus margin) amounts 8.31 dB in this case, which means an increase of 2.31 dB or 30 %. The continuous line shows the sensitivity function of the plate with dampers. The maximum value equals 6.05 dB. This is a sensitivity increase of 0.05 dB or, absolute, 1.1 %, caused by a decrease in plate damping of 33 %. Here, the modal damping increase, as mentioned in Section 2.1, becomes visible in terms of robustness. The dampers have a major contribution to the modal damping of the resonances that are visible in the frequency response functions. Therefore, the system becomes relatively insensitive to changes in the dynamical behaviour of the plate itself.

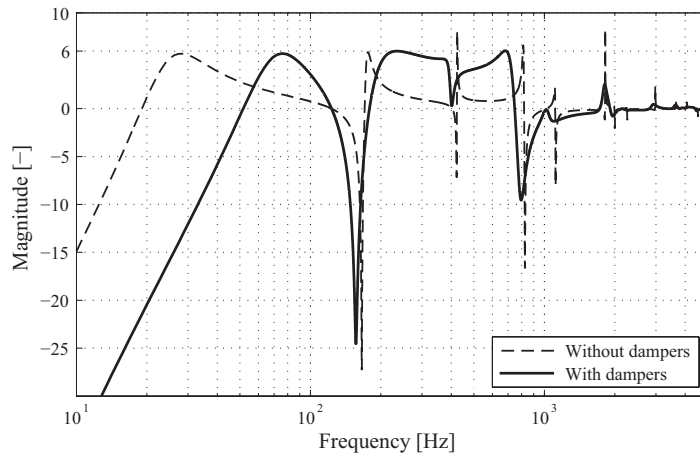


Figure 2.16: Bode diagram of the sensitivity functions of the undamped and damped plate in z-direction in case of lowered modal plate damping ( $\zeta = 0.002$  instead of 0.003).

## 2.8 Damper design & validation

This section describes the design and experiments of a one degree of freedom damper with a high damping coefficient. In the analyses as described in Sections 2.2-2.7, an ideal mass-spring-damper system is applied. This damper is designed and tested to prove that it is possible to create dampers with over-critical damping values and with natural frequencies that are high enough to be useful. The spring and damper are assumed to behave linearly: the spring provides a force proportional with the relative damper displacement and the damper applies a force proportional with the velocity difference between the plate corner and the damper mass. These assumptions allow Laplace transformations and allow performing analyses in the frequency domain. In addition, the vibration amplitudes of high-tech positioning tables are small, which allows for assuming linear system theory. These small vibration amplitudes lead to small damper strokes. Therefore flexures can be used to provide for the guidance of the RMD's moving mass. The dimensions of the flexures determine the spring stiffness and therefore the natural frequencies of the RMD. An additional advantage of flexures is the lack of hysteresis, which enables the damper to work even if the damper strokes are very small.

### 2.8.1 Natural frequencies

The dampers are intended to act purely in z-direction and the remaining directions are neglected. This can be translated in requirements with respect to the natural frequencies of the RMD in z-direction. The natural frequency in this direction is determined at 1250 Hz to validate the possibility of RMD design for stages with realistic natural frequencies. The natural frequencies in other directions should be as high as possible to avoid the addition of low-frequency parasitic dynamics to the plant. Figure 2.17 shows the FEM results of the damper design. The frequency in z-direction is shown in the left plot and is 1250 Hz. The second natural frequency is 8100 Hz and shows a rotation of the damper mass around the z-

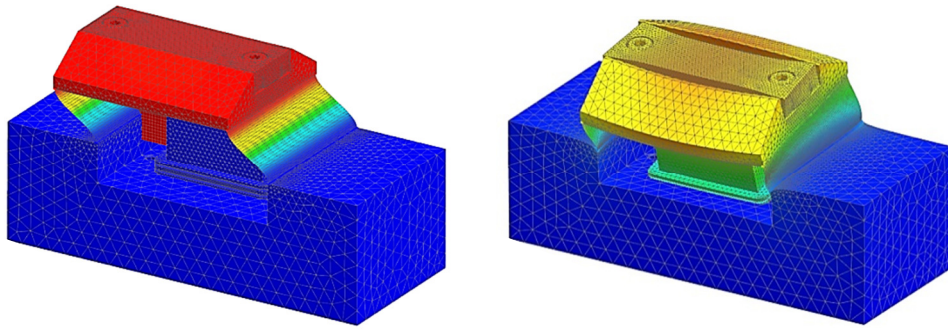


Figure 2.17: Natural frequencies of the damper mass. The first natural frequency is at 1250 Hz and the second at 8100 Hz. The bottom surface is constrained by a fixed displacement constraint.

axis. This shows that the natural frequencies in other directions are over 6 times higher than the main natural frequency and are assumed to be high enough, even for realistic implementation, to avoid problematic changes in stage dynamics.

The second challenge is to create a damping mechanism with a high damping coefficient in a relatively small volume. The damper is designed to be passive. This guarantees stability of the damper systems itself and preserves from increasing complexity. As damping concept a viscous fluid damper is chosen due to the following properties:

- the linear time-independent behavior,
- the ability to create an extremely large damping constant in a small volume,
- separation of stiffness and damping in the damper design, which enables to design mechanical properties for different directions independently,
- the supreme damping properties of fluids with respect to other damping materials: the phase of a fluid is close to 90 deg for a large frequency range, which indicates that viscous damping is included.

More information about the damper principle and the elaboration of the fluid damper is

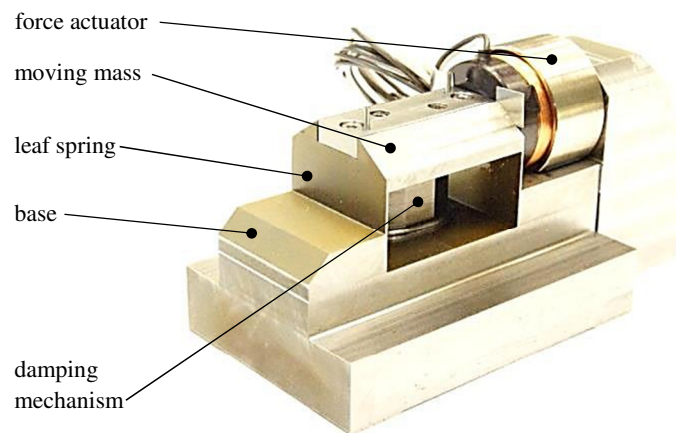


Figure 2.18: Damper test setup to measure the damping characteristics.

provided in Chapter 4. The fluid applied is Rocol Kilopoise 0868 and is chosen based on the extremely high viscosity of 220 Pas. The test setup is shown in Figure 2.18. A voice coil is applied as force actuator and the RMD position is measured optically by a laser vibrometer.

### 2.8.2 Damper measurements

The measured frequency response function is shown in Figure 2.19 and is represented by the continuous line. The dashed line represents the frequency response function of this mechanism without damping. Note that the undamped natural frequency is decreased to 1100 Hz due to the mass contribution of the voice coil. The measurement shows that the next natural frequency in this direction appears above 10 kHz. This is sufficient to be useful in case of a realistic damper implementation on a positioning stage. The measurement clearly shows that the damper mechanism is over-critically damped: the resonance amplification has disappeared in the measured response. Although the resonance frequency is located at 1100 Hz, the phase delay caused by the high damping value is visible from approximately 10 Hz. The frequency response function is measured with different force amplitudes as input to examine the linearity of the system behavior. The same frequency response function is obtained for different input amplitudes.

### 2.8.3 Improved damper model

The dash-dotted line represents a fit of the damping behavior. The simple mass-spring-damper model, as used in Sections 2.2-2.7 is not sufficient to create a good fit. Therefore, the model

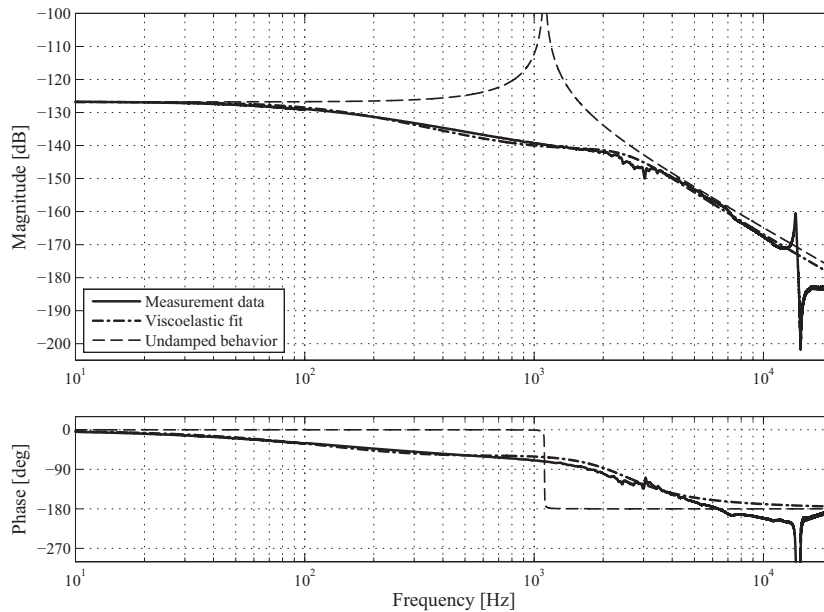


Figure 2.19: The solid line represents a measured frequency response function of the damper test setup. The dash-dotted line represents the behavior of the damper with the Burgers viscoelastic material model included. The dashed line represents the behavior of the damper without damping material.

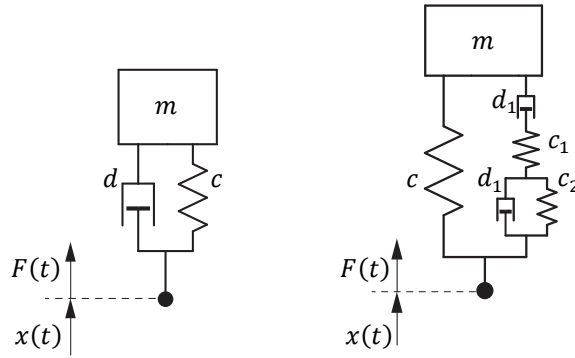


Figure 2.20: Dynamic models of the TMD with displacement input  $x(t)$  and force output  $F(t)$ . The left figure shows the ideal RMD model. The right model contains an extended model of the damping behavior which includes the Burgers viscoelastic model.

of the damping is extended to the Burgers viscoelastic model. This extension is visualized in the right part of Figure 2.20. The original model is shown in the left part of this figure. The dash-dotted line shows that it is possible to fit the damping behavior quite accurately with this damper model. The main behavior is still determined by the damper. The additional springs and damper are necessary to describe the magnitude and phase drop correctly. This damper model can be used in further analyses to improve the accuracy of the damped model and predict the performance increase of a positioning stage with dampers in a more accurate way.

## 2.9 Conclusions

This chapter presented a method to increase the performance of a positioning table with inherently low-damping in a robust manner. A performance increase in  $z$ -direction is achieved by adding robust mass dampers to the positioning table. The high damping value used, in contradiction to a regular tuned mass damper design, leads to improved dynamics from control point of view. The use of these damper structures with over-critical damping values is new and leads to amplitude reductions of resonances in a broad frequency band. In addition, the stage dynamics becomes relatively insensitive for variation in stiffness and damping of the damper itself, which is a well-known drawback of implementing regular TMD's. The modal damping of the positioning table increases, resulting in reduced resonance amplifications. This property allows for a higher controller gain and therefore a higher bandwidth. The potential of this advantage is shown elaborately in this chapter. The resulting system properties are a faster response, by a factor 2.7, and better disturbance suppression for both position and force disturbances. The suppression factors are both roughly 12 times. In addition, the  $\varphi$ - and  $\psi$ -directions benefit from this approach. The damping is increased in these directions as a consequence of the dampers added in  $z$ -direction. Although the damper parameters are not optimized for maximum performance increase in these rotational directions of motion, substantial advantages occur. The bandwidth is increased 2.9 times and the disturbance suppression is improved 12 times.

The system's performance is increased in a robust manner. This property holds for the dynamical behavior in  $z$ -direction as well as the  $\varphi$ - and  $\psi$ -directions. The RMDs are over-critically damped and therefore display a low sensitivity to parameter changes in terms of stiffness and damping. In addition the sensitivity with respect to changes in the plate dynamics is decreased. Even in case of more complex controller implementations, these properties will lead to performance and robustness improvements.

# Sensitivity Based Iterative Approach to Increase Closed-loop Performance

**Abstract** - In motion systems, high controller gains are beneficial to suppress low-frequency disturbances acting on the system. Low-damped non-rigid body resonances usually limit the controller gain. Robust Mass Dampers with a relatively high damping value have shown to be able to increase the damping of the non-rigid body resonances over a broad frequency range, hence enabling to increase the feedback bandwidth. The main challenge is to determine the optimal stiffness and damping values for these dampers to improve the closed-loop performance of the motion system. This chapter proposes a modulus margin based iterative optimization procedure which includes a square plate as plant model on which ideal dampers added. A PID<sup>+</sup>-type controller is applied to close the loop and calculate the performance. This gives optimal damper parameters – stiffness and damping – in combination with a high bandwidth controller, which results in an improved disturbance suppression at frequencies below the bandwidth and a faster setpoint tracking. The iterative approach is subject to a modulus margin and a stability constraint in order to guarantee stability in combination with a robust solution.



### 3.1 Introduction

In the industry of high-end manufacturing, for instance the semiconductor market, various processing and measurement steps take place on positioning stages. The number of products processed per unit of time (throughput) is directly related to the accelerations and velocities of these motion systems. The functional density of the product – the minimum feature size – and the accuracy of the process are related to the accuracy of a motion system. These two properties lead to conflicting requirements, like high accuracies combined with high accelerations [18].

A motion system can be seen as a mechanical device with position sensors and force actuators. The basis of the system's performance is governed by the mechanical design. Finite Young's moduli of materials result in non-rigid body (NRB) natural frequencies with their corresponding mode shapes. The natural frequencies are solely defined by the distribution of mass and stiffness, i.e., by the mechanical design of the components. These natural frequencies are included in the transfer function as poles. The frequencies at which resonances arise in the frequency response function, depends on these poles and the actuator and sensor locations on the mechanical structure. Both actuator and sensor should experience a displacement corresponding to a certain mode shape to make this resonance visible in a frequency response function. The natural frequencies arise in transfer functions as poles, and zeros arise at frequencies at which a combination of poles cancels each other's amplification magnitudes [86,97].

A complex motion system usually contains more than one actuator and sensor. One way to deal with such multivariable plants is by applying a decoupling procedure to obtain transfer functions in a preferred coordinate system [23]. Standard PID-type controllers are then able to stabilize the dominant components of the resulting transfer function matrix. In practice, more complex controllers, often extended with notch filters, are implemented to deal with the non-rigid body (NRB) dynamics [16,92]. A drawback of this solution is the decrease of the system's robustness: in case of varying natural frequencies, the notch filter is placed incorrectly and the stability margins might diminish and eventually may vanish, which means that the closed-loop behavior is destabilized. Besides the frequency of the resonance, in addition, the amount of structural damping affects the achievable bandwidth. High-precision designs often lack substantial damping. Monolithic stages have few mechanical connections, materials like aluminum or ceramics and vacuum environments devoid of squeeze film damping, which all contribute to this property. The results are resonances with large amplifications. Summarizing, the presence of NRB zeros and poles in a frequency response function and the sequence in which they appear finally limits the performance of the control system.

One of the most important properties of a control system, besides guaranteeing stability, is suppressing low-frequency disturbances that act on the motion system. The extent to which disturbances influence the motion system can be represented by the sensitivity function. In case of motion systems, the sensitivity function is typically low for frequencies far below the bandwidth. Above the bandwidth the controller is not able to suppress forces acting on the

system. In this thesis, the bandwidth is defined as the first top-down zero dB crossing of the open-loop frequency response function, i.e., also known as the cross-over frequency. The sensitivity function for frequencies below the bandwidth approximates the inverse of the open loop. According to the reasoning above, a high controller gain is desirable to counteract disturbances in combination with a stable closed-loop behavior. As a measure for stability and the corresponding robustness margins during controller design, the modulus margin is used. This margin can be interpreted as a bound on the sensitivity function. In case of a  $PID^+$ -type controller, this bound becomes limiting at frequencies above the bandwidth caused by the NRB natural frequencies. A solution to improve a motion system's bandwidth exists by adding damping to the – low-damped – NRB resonances in the plant. This leads to a suppression of the amplitude of these resonances. Therefore, the sensitivity function will decrease for frequencies above the bandwidth and additional room for controller gain improvement is created [104].

In addition to the ability to damp a specific natural frequency, Robust Mass Dampers (RMD's) are able to provide broad banded damping to a range of resonances if added to a motion stage. For this, the dampers should contain a high amount of damping. The question is, how to determine the mass, stiffness and damping of the RMDs to obtain the best closed-loop performance possible.

This chapter proposes an iterative approach to determine the design parameters of an RMD based on the modulus margin of the closed-loop system. Because the closed-loop behavior has to be optimized, the controller has to be included in the procedure. The contribution of this chapter is to provide a design method and solution which has the following properties:

- it creates broad band damping for mechanical resonances,
- it enables performance increase in z-direction (out-of-plane),
- the parameters of the dampers are determined such that the best closed-loop performance is obtained.

Section 3.2 briefly introduces the regular TMD and the robust variant called RMD. Section 3.3 presents the positioning table model which is used for simulation. A controller is designed and the performance of the system determined. Section 3.4 introduces the plate extension with dampers and the method to determine the damper parameters for optimal closed-loop performance. In Section 3.5 the performance increase in z-direction is presented. Section 3.6 enumerates the conclusions and, finally, Section 3.7 discusses about the results and the methods applied.

### **3.2 Undamped stage behavior**

A tuned mass damper (TMD), also known as harmonic absorber can be used to suppress a specific resonance amplitude [25]. A TMD is a passive device consisting of a structural mass which is connected to a mechanical structure by a parallel spring-damper combination, see

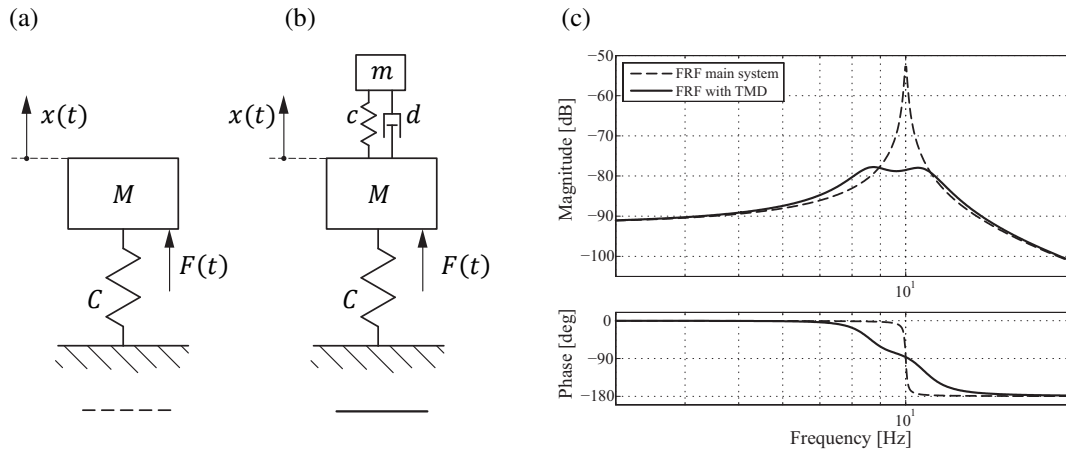


Figure 3.1a: Main structural mass model with force actuation  $F(t)$  and positions measurements  $x(t)$

Figure 3.1b: Main structural mass with a TMD added to reduce the amplitude

Figure 3.1c: Bode diagrams of the undamped and the damped system indicated with the dashed line and continuous line respectively

Figure 3.1a and Figure 3.1b. Mass  $M$  represents the main structural mass and  $m$  represents the TMD mass mounted on the spring with stiffness  $c$  and the damper with damping constant  $d$ . The mass contribution of the TMD is usually up to 10% of the main structural mass and is determined based on the required suppression factor. The undamped natural frequency of the TMD depends on its mass  $m$  and stiffness  $c$ . The natural frequency of the TMD has to be tuned close to the natural frequency of the main structure. Subsequently, an amplitude reduction of the main structure is achieved at the resonance frequency by adjusting the correct amount of TMD damping, see Figure 3.1c. Equations to calculate the optimal stiffness and damping values can be found in [25]. The modal damping value of a TMD is usually determined between 10 and 25 %.

A drawback of this type of TMD application is the relatively large sensitivity of the reduction factor to parameter variations of stiffness and damping of the TMD. This property also holds for natural frequency variations of the main structure: the overall system performance will be strongly affected by parameter variations of the mechanical parts. One can think of variations caused by wear, temperature variations and varying frictions as function of temperature and position. TMD's are well-understood and have proven to be useful in a widespread field of applications, for instance: automotive industry, buildings and structures, airplanes, machine frame designs and space structures, see [34,47,72]. In addition, more complex TMD configurations are investigated to achieve an efficiency increase per unit of damper mass [110]. Although TMD's are often designed as passive devices, also semi-active [70] and active variants have been described [63]. A main advantage of the TMD configuration is that these do not introduce reaction forces in other machine parts.

Notice that for all the mentioned applications of TMDs, the effects are always intended to damp one specific resonance of a structure. A previous study showed that substantial damping can be added to a range of resonance frequencies by adapting the properties of a TMD [104].

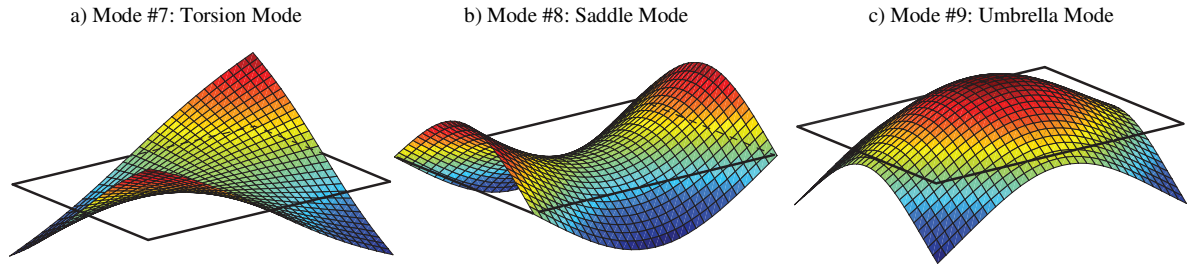


Figure 3.2: First three non-rigid body mode shapes of a square plate in order of appearance.

The modal damping value is increased to values larger than 50 %. This broadens the frequency range in which the damper efficiently suppresses resonance frequencies. In addition, the robustness of the damper increases as well as the robustness of the overall dynamics. This is important with respect to the loops that are closed by the controller: non-robust behavior might deteriorate the stability significantly. Therefore, this variant is called Robust Mass Damper (RMD).

### 3.2.1 Abstracted stage model

The goal of this chapter is to optimize the out-of-plane vibrational behavior of a motion stage with a relatively large length-to-height-ratio. Especially, the bandwidth limiting high-frequency dynamical behavior is of interest. The most simple and abstracted three-dimensional model of such a table is a square plate. A characteristic of a plate is the presence of mode shapes with relatively large out-of-plane displacements. The mode shapes of an aluminum plate with dimensions of  $600 \times 600 \times 10$  mm are calculated by means of Finite Element Method (FEM). Shell elements are applied to describe the behavior of the thin plate appropriately. A modal analysis is performed and the node displacements in z-direction of the first hundred mode shapes and natural frequencies are exported, including the 6 Rigid-Body (RGB) modes, and are stored in mode shape matrix  $\Phi$ . The geometric properties are listed in Table 3.1. The z-coordinates of the components are not listed due to the application of shell elements in the FEM-model: the thickness of the plate is zero and, therefore, all z-coordinates are zero.

The RGB modes appear as low-frequency modes without plate deformation. The exported modes are used to create a state-space description of the plate dynamics in modal form. A

Table 3.1: Stage information listed.

| Name                | Value                      | Unit            |
|---------------------|----------------------------|-----------------|
| Plate dimensions    | $600 \times 600 \times 10$ | mm <sup>3</sup> |
| Material            | aluminium                  | -               |
| Plate mass          | 9,85                       | kg              |
| Location actuator 1 | (180,180)                  | mm              |
| Location sensor 1   | (300,300)                  | mm              |

Table 3.2: Frequencies corresponding to the first 5 NRB mode shapes.

| Mode #  | Nat. freq. | Name          |
|---------|------------|---------------|
| Mode 7  | 89.4 Hz    | torsion mode  |
| Mode 8  | 130.8 Hz   | saddle mode   |
| Mode 9  | 165.8 Hz   | umbrella mode |
| Mode 10 | 231.5 Hz   | H.O.-mode     |
| Mode 11 | 231.5 Hz   | H.O.-mode     |

modal damping of 0.003 is applied to the NRB resonance frequencies. The dynamic model and post-processing scripts are created in Matlab<sup>®</sup>. Table 3.2 presents the natural frequencies of the first 5 NRB modes.

### 3.2.2 SISO frequency response functions

Actuator and sensor locations are chosen and frequency response functions are calculated for control design. The actuators and sensors operate in z-direction. Sensors are located on the outer edges of the positioning table as the center is reserved for the process. Therefore, four displacement sensors are modeled on the stage corners. Figure 3.3 presents the plate with the actuator positions, sensor positions and the center of gravity (*COG*) indicated. For the investigation of bandwidth limitations it is important to note that the actuators and sensors are placed in a non-collocated configuration.

A geometrical decoupling procedure is applied to the multi-input multi-output (MIMO) plate model to obtain a multiple single-input single-output (SISO) transfer function matrix with the rigid body motions, in logical coordinates, dominating in the diagonal components. In motion control this procedure is in fact a decoupling of the actuation/measuring directions. In this case the transformation is applied with respect to the plate's *COG*. The resulting rigid body motion directions are a translation in z-direction and two rotations around respectively the *x*- and *y*-axis. These rotational directions are denoted the  $\varphi$ - and  $\psi$ -direction. The four actuators and sensors enable to decouple a fourth degree of freedom, which is the torsion mode: the first NRB mode shape. Transformation matrices  $T_u$  and  $T_y$  are constructed from actuator and

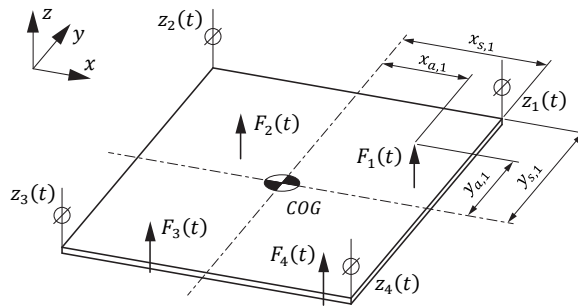


Figure 3.3: The plate model with the positions of the force actuators and position sensors indicated.

sensor coordinate information to decouple the RGB motion directions (3.1), (3.2), (3.3).

$$T_u = \begin{bmatrix} 1 & 1 & 1 & 1 \\ x_{a,1} & x_{a,2} & x_{a,3} & x_{a,4} \\ y_{a,1} & y_{a,2} & y_{a,3} & y_{a,4} \\ \Phi_{a,1}^{NRB,1} & \Phi_{a,2}^{NRB,1} & \Phi_{a,3}^{NRB,1} & \Phi_{a,4}^{NRB,1} \end{bmatrix}_{COG}^{-1} \quad (3.1)$$

$$T_y = \begin{bmatrix} 1 & y_{s,1} & x_{s,1} & \Phi_{s,1}^{NRB,1} \\ 1 & y_{s,2} & x_{s,2} & \Phi_{s,2}^{NRB,1} \\ 1 & y_{s,3} & x_{s,3} & \Phi_{s,3}^{NRB,1} \\ 1 & y_{s,4} & x_{s,4} & \Phi_{s,4}^{NRB,1} \end{bmatrix}_{COG}^{-1} \quad (3.2)$$

$$P_{decoupled}(s) = T_y \cdot P(s) \cdot T_u \quad (3.3)$$

This approach is called geometrical decoupling due to the geometric information of the stage that is used. In these matrices,  $x$  indicates a distance in  $x$ -direction between actuator/sensor and the  $COG$  and  $y$  corresponds with a distance in  $y$ -direction with respect to the  $COG$ . Subscripts  $a$  and  $s$  respectively indicate a distance to an actuator or sensor w.r.t.  $COG$ . The numbers in the subscripts  $(1, \dots, 4)$  correspond to the actuator and sensor numbers: see Figure 3.3 for the placement of actuator and sensor 1 with respect to the  $COG$ . Displacement components of the mode shape matrix  $\Phi$ , corresponding to the position of the actuator and sensor nodes, are used to decouple the torsion mode. For this chapter, the focus is on the transfer function in  $z$ -direction. The frequency response is shown in Figure 3.4. Note that this frequency response function contains 2 zero-pole pairs – collocated behavior – before the phase drops to  $-360$  deg. This non-collocated behavior is induced by the position difference

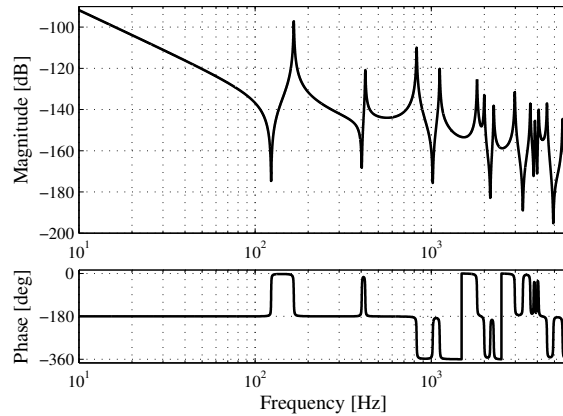


Figure 3.4: Decoupled transfer function of the undamped plate in  $z$ -direction. This transfer function is obtained by the geometrical decoupling procedure.

between actuators and sensors. It eventually limits the controller gain and therefore the bandwidth and the low-frequency sensitivity.

### 3.2.3 Controller design in z-direction

This chapter describes an improvement of a motion system's dynamical behavior by modifying the plant dynamics in a closed-loop analysis. This implies that the controller is included in the optimization. To obtain a comparable measure of the overall system improvement, controllers of equal order are designed for different plants and the closed-loop performance is evaluated.  $PID^+$  controllers are applied containing the following components:

- ( P ) proportional gain,
- ( I ) integrator,
- ( D ) lead filter,
- (  $^+$  ) first order low-pass filter.

To make cases comparable, the zero of the integrator is placed exactly at 1/5th of the bandwidth frequency (BW) in all cases (defined here as the cross-over frequency, i.e., the first open-loop top-down zero dB crossing of the open-loop gain). A low-pass filter is added to create high-frequency roll-off. Figure 3.5 shows the Nyquist diagram of the open loop of the SISO decoupled plant in z-direction with its controller. The achieved bandwidth is 28 Hz. A modulus margin of 6 dB is used. This modulus margin is the radius of the circle around the point (-1,0) in Figure 3.5. The distance of the open-loop frequency response function to the point (-1,0) is the inverse of the absolute sensitivity function and, therefore, this graph relates the open-loop and closed-loop behavior, see [86], Figure 2.16. The bandwidth-limiting NRB resonances are clearly visible in the Nyquist diagram by the circles starting at the origin [19,26].

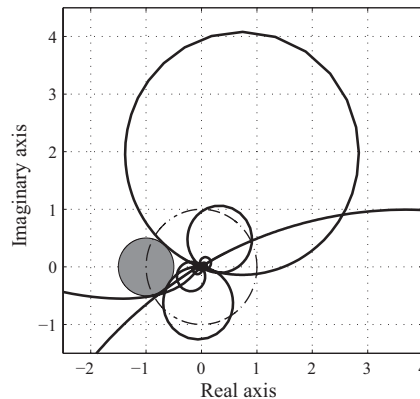


Figure 3.5: Nyquist diagram of the open-loop of the undamped plate with the modulus margin of 6 dB indicated by the circle.

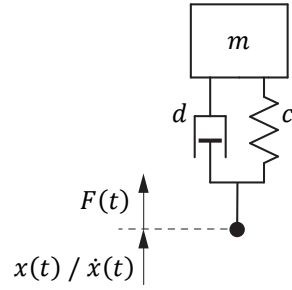


Figure 3.6: Dynamic model of the TMD with displacement and velocity inputs  $x(t)$  and  $\dot{x}(t)$ , respectively, and force output  $F(t)$  indicated.

### 3.3 The damped stage model

Four RMD models are added to the plate model. Figure 3.6 shows the damper model. The state space matrices are provided in Chapter 2. The specific NRB resonances which limit the bandwidth of the system have relatively large displacements at the plate corners and therefore relatively high velocities at those locations. Figure 3.7 presents the mode shape corresponding to the resonance frequency at 830 Hz, which limits the bandwidth by its non-collocated character. A large displacement of a certain mode is equivalent to a low modal mass of that particular mode at this position: this statement is further elaborated in Section 5.2.2. This implies that an RMD with relatively low mass can suppress a certain resonance more effectively at a location with relatively large displacements. Figure 3.8 presents the plate with four dampers added in z-direction. Chapter 2 showed that RMDs with a mass per unit of 0.35 % of the plate mass are able to create substantial suppressions. This increases the overall stage mass by 1.4 %.

The open-loop of Chapter 2 has shown that substantial damping can be added to a range of resonance frequencies. In this approach, the natural frequencies of the dampers were adjusted around the first resonance frequency of the plate by tuning the spring stiffness  $c$ . For the plate

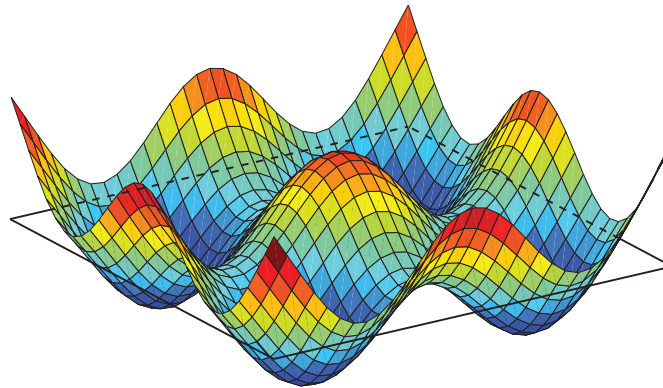


Figure 3.7: NRB mode shape at 830 Hz. Note the relatively large displacement amplitudes at the plate corners.



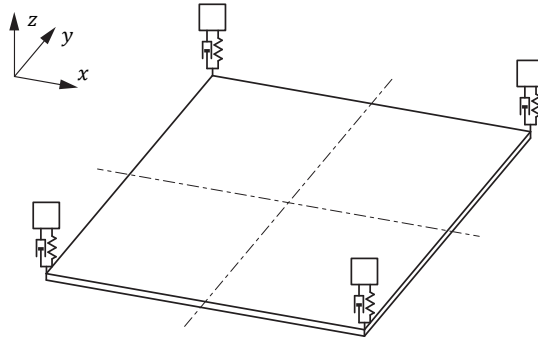


Figure 3.8: Model of a square plate with 4 dampers added on the corners. The degree of freedom of the dampers is in  $z$ -direction. The four dampers have equal mechanical properties: mass, stiffness and damping values.

this frequency is about 90 Hz, which corresponds to the torsion mode. A relatively high damping value is applied to achieve a modal damping increase of the plate between 400 Hz and 2 kHz. This damping appears as an amplitude reduction of the resonances. To find a suitable damping value, the damper constant  $d$  is increased and the frequency response functions are calculated and visualized in a Bode diagram, see Figure 3.9. This figure shows the diagram for a range of damping values. The damping value is mainly determined by the suppression factor of the resonance at 830 Hz. This point (250 Ns/m | 830 Hz) is indicated in the figure. The other resonances in the range of 400 – 2000 Hz are less sensitive to the damping value and are also damped. The approach as presented above contains two drawbacks: 1) the analysis is performed in open loop. Although the damping of the NRB resonances is increased, this is no guarantee for performance increase of the closed-loop system, and 2) only the magnitude information is taken into account. This latter is a major disadvantage, because the performance of a (motion) system is often more limited by the phase than it is limited by the magnitude: a perfectly collocated frequency response function does not limit the BW although magnitude differences are present. If the phase of a resonance allows, the magnitude will not be limiting at all.

Therefore, a closed-loop performance indicator should be determined to avoid these disadvantages and to be able to guarantee performance increase of the closed-loop system.

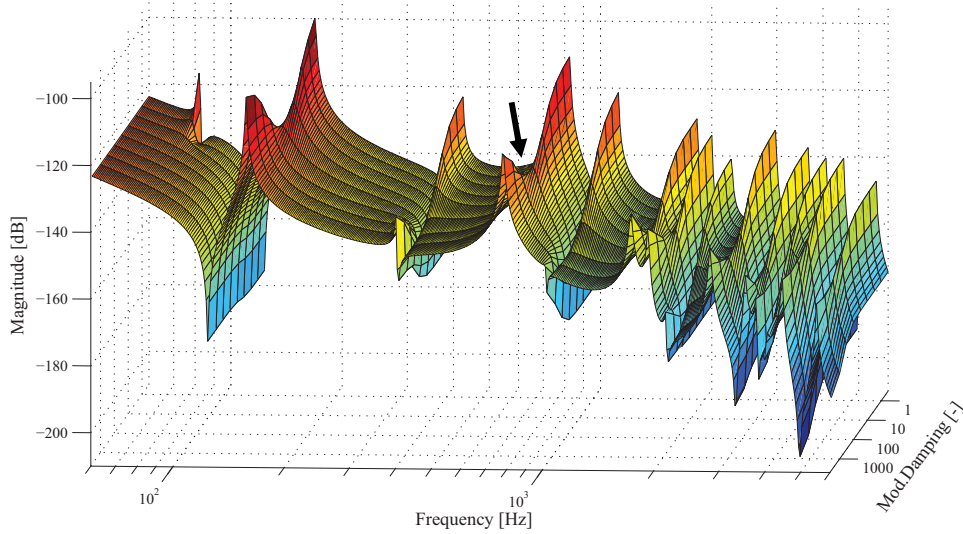


Figure 3.9: The magnitude part of Bode diagrams as function of the modal damping of the RMDs. The arrow indicates the minimum value for the BW limiting resonance, around 830 Hz. Note that this damping value is too large to suppress the first resonance effectively.

### 3.4 Closed-loop parameter optimization

#### 3.4.1 Sensitivity criterion

In the previous section an open-loop method was explained to determine the damper parameters. However, the positioning table will operate in closed-loop. Therefore, the damper parameters should be optimized for closed-loop behavior. A commonly used measure of the performance is the bandwidth, which indicates until which frequency the system will be able to follow the setpoint in case of a harmonic input. This is a relatively good measure of the performance if and only if the controller is designed well. If this is not the case, the BW is meaningless. For instance, if the -1 slope in the open loop lasts too long, a very high BW can be obtained, however, due to the differentiator and/or absence of an integrator, low

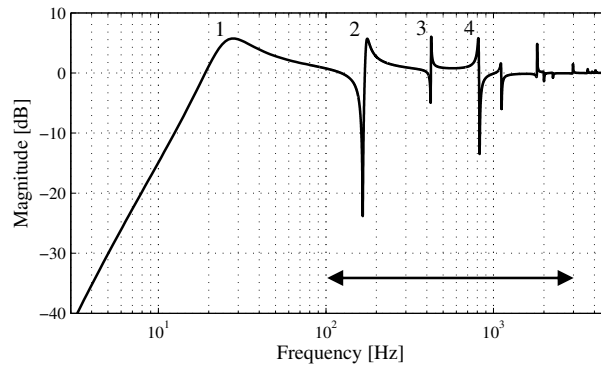


Figure 3.10: The sensitivity function of the closed-loop system. The frequency range with bandwidth limiting resonances is indicated by the arrow. The numbers indicate the points of contact with the modulus margin line at 6 dB.

performance is obtained in terms of low-frequency disturbance suppression and setpoint tracking. A good criterion of closed loop performance is given by the sensitivity function: the magnitude as function of the frequency describes the ability of the closed-loop system to suppress disturbances. This property is, besides stabilizing the closed-loop system, one of the most beneficial properties. In addition, the modulus margin is a robustness margin with respect to stability of the system. Therefore, in this chapter, the sensitivity is used as criterion to define the performance.

### 3.4.2 Approach

The frequency response function of the undamped plant in z-direction and the corresponding controller are taken as starting-point. The sensitivity FRF is calculated and presented as in Figure 3.10. The numbers in Figure 3.10 indicate the contact points of the sensitivity function with the modulus margin. Number 1 is induced by the controller and shows the phase lead at the mass line around the bandwidth. Numbers 2, 3 and 4 indicate higher order (NRB) dynamics, which limit a further increase of the controller gain. Damper mechanisms are added to the stage with a moving mass of 35 g per damper. This amount of mass is based on the modal mass of the BW limiting mode at 830 Hz, which approximately contains 2 kg moving mass. The damper masses of 35 g amount 7 % of this modal mass. In addition, less than 1.5 % mass is added to the stage.

The focus during damper parameter optimization is on the NRB resonance frequencies because these frequencies limit the bandwidth of the closed-loop system. The corresponding frequency range is indicated in Figure 3.10 by the arrow. The first sensitivity peak frequency,

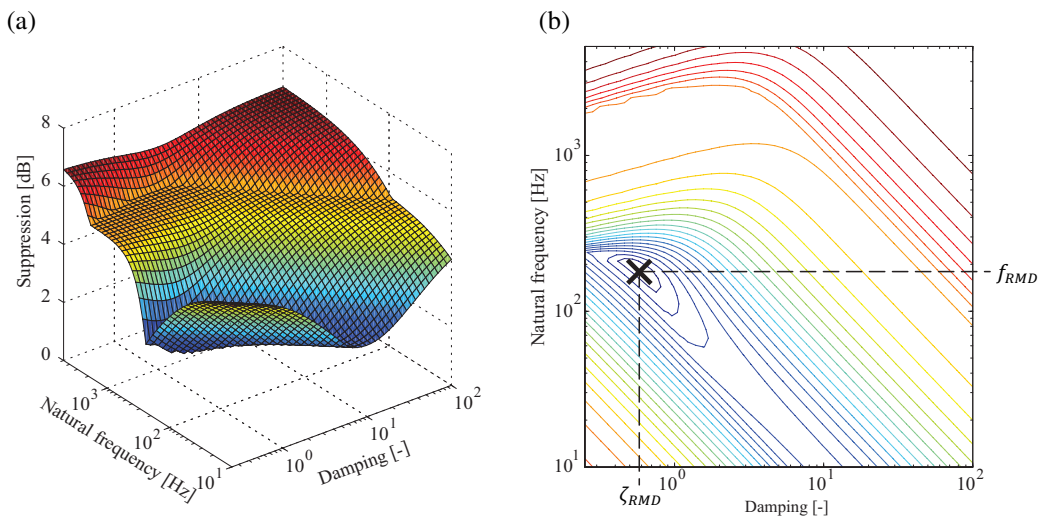


Figure 3.11a: The maximum values of the sensitivity function as function of the RMD natural frequency  $f_{RMD}$  and modal damping  $\zeta_{RMD}$  corresponding to the first iteration step. The figure is plotted on logarithmic axes.

The controller designed for the undamped plate model is included in this iteration step.

Figure 3.11b: A contour plot of the sensitivity landscape with logarithmic axes, with the minimum value indicated by the cross.

indicated by (1) is not included in the optimization because this peak is induced by the phase lead of the controller and is located around the bandwidth. Therefore this peak is adjustable by tuning the controller parameters. The goal is, firstly, to find damper parameters for which the sensitivity function in the NRB frequency range, with numbers 2,  $\dots$ , 4, shows an as low as possible maximum value with the controller fixed. The sensitivity function is calculated for a range of stiffness and damping values, and subsequently, for each sensitivity function the maximum value between 1000 Hz and 5000 Hz is stored in a matrix. This results in a matrix of peak values of the sensitivity functions in the specified frequency range. The corresponding 3D-graph is shown in Figure 3.11a. The corresponding equation is:

$$\min_{K,D} \|W(s)S(s)\|_{\infty} \quad (3.4)$$

This shows a minimization of a weighted sensitivity function as function of the damper parameters. The right part of Figure 3.11 presents a contour plot in which the minimum is indicated by the cross. The corresponding natural frequency  $f_{RMD}$  and damping value  $\zeta_{RMD}$  minimize the sensitivity function at the NRB resonance frequencies. The result of the controller and the new plant obtained by this iteration step is shown in Figure 3.12, which presents a Nyquist diagram that shows the contact points of the open-loop response line with the modulus margin circle and the room for increasing the controller gain. Note that the modulus margin, as used in the optimization above, includes both magnitude and phase information and therefore calculates the smallest distance between the high-frequency resonances and the point (-1,0) in the Nyquist diagram. This means that the plant is modified in such a way that the controller gain can be maximized.

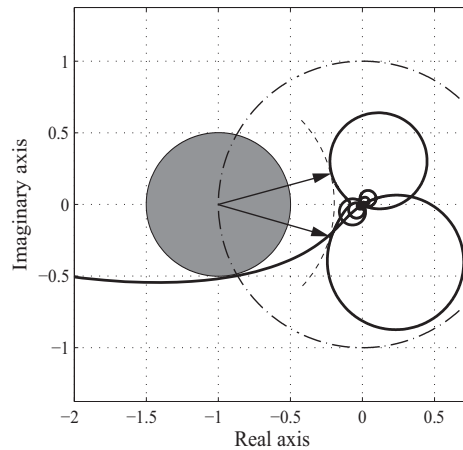


Figure 3.12: Nyquist diagram of the optimized plant – first iteration - in combination with the controller designed for the undamped plant. The achieved modulus margin improvement is indicated by the arrows and the concentric dashed arc w.r.t the point (-1,0).

### 3.4.3 Iteration procedure

Optimal damper parameters are determined to minimize the modulus margin at the higher order dynamics with a  $PID^+$  controller included. The next step is to design a new controller with a higher gain. This increases the bandwidth of the system and, more importantly, decreases the sensitivity value for low-frequency disturbances. The turnover frequencies of the lead filter should be shifted to higher frequencies according to the gain increase of the controller, to maintain phase lead at the bandwidth. This shift affects the phase at higher frequencies, i.e., in the specified frequency range of the HF dynamics. Although the controller gain can be increased and the plant-controller combination appears to be improved, the result is still sub-optimal. More iteration steps have to be made to deal with these characteristics: the new controller has to be used to calculate a second landscape. A further improved plant can be calculated with the resulting stiffness and damping values for the RMDs. The landscape of this second iteration step is shown in Figure 3.13. The overall procedure can be expressed by:

$$\begin{array}{l}
 \max_{C(s)}(\omega_{BW}) \\
 \downarrow (K, D) = \arg \left( \min_{K, D} (\|W(s)S(s)\|_{\infty}) \right) \\
 \text{end}
 \end{array} \quad (3.5)$$

### 3.4.4 Stability criterion

In the second iteration step, the controller might contain a substantially higher gain than in the first iteration step which included the undamped plant and corresponding controller. In this particular example, the proportional controller gain has been increased by a factor 13 at the first iteration step. This implies that the closed-loop system can become unstable by changing the RMD's stiffness and damping values. Therefore, a criterion on the closed-loop stability is

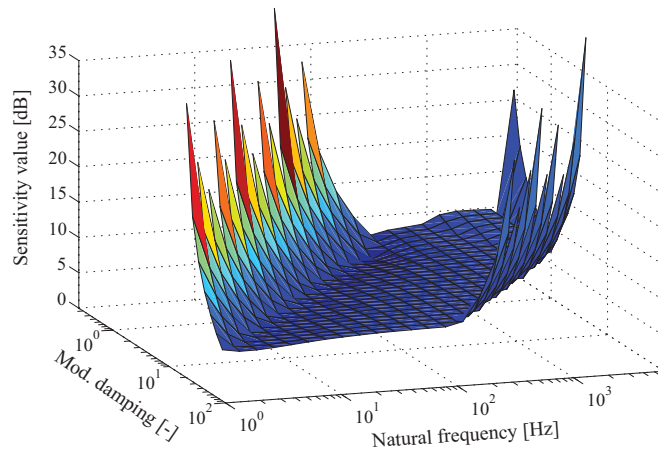


Figure 3.13: Sensitivity landscape of the second iteration step. Note the corners of the matrix in which no sensitivity value is stored. In these regions the closed-loop system is destabilized by the dampers.

included in the calculation of the sensitivity landscape. The closed-loop stability is checked by calculating the closed-loop poles and checking for right half plane (RHP) poles for every point in the sensitivity landscape matrix. If RHP poles exist, the particular point in the matrix is left empty. As visible in Figure 3.13, the two corners do not contain peak sensitivity values due to unstable behavior in these regions. This check is applied in all iteration steps. The steep derivatives towards the unstable regions already indicate that - at least one - pole pair is shifting towards the imaginary axis of the pole plot, indicated by the sensitivity value that is increasing rapidly. This phenomenon is visible in Figure 3.13. After adjusting the damper parameters, a new controller has to be designed to increase the controller gain further. In the first iteration step the overall system gain was too low to enable destabilization of the system by changing the stiffness and damping parameters, see Figure 3.11.

### 3.4.5 Iterative improvement

The calculation of the landscape, with enough points to create sufficient detail of the dynamics, takes some time. If the result is sub-optimal after controller design, the same landscape can be used to increase the iteration speed. To do this, the user should have an idea about the influence of parameter changes on the system, i.e., which resonances actually limit the performance. In that case, the damper parameters can be adjusted, based on the landscape of the previous iteration. This is mainly possible after the first iteration, as the parameters change more slightly. If the dynamics changes substantially, new landscapes have to be calculated. This is mainly the case in the first iteration steps. In order to obtain a final plant-controller combination, the plant and controller have to be recalculated a few times. The results for the plate model are listed in Table 3.3. In this example, the performance values saturate after three iteration steps. This does not guarantee that the global minimum is found, however, it is not possible to increase the performance further by this approach. The final step and corresponding controller determine the performance of the system.

A flowchart of the optimization procedure is shown in Figure 3.14. The first four blocks show the initial process of plant modelling, geometrical decoupling and controller design. After these steps, the performance limiting modes have to be studied and dampers have to be added. The moving mass has to be determined based on the modal mass of the main system. This enables to enter the loop and search for the optimal parameter combination.

The RMDs increase the modal damping of the out-of-plane resonances. These modes are visible in other directions than the  $z$ -direction too. The bandwidth development in these

Table 3.3: Bandwidth increase and damper parameters as function of the iteration steps.

| Case        | $f_{elg}$ [Hz] | $\zeta$ [-] | $z$ [Hz] | $\varphi/\psi$ [Hz] |
|-------------|----------------|-------------|----------|---------------------|
| Undamped    | -              | -           | 28,4     | 77,6                |
| Iteration 1 | 184,9          | 0,588       | 70,8     | 82,6                |
| Iteration 2 | 244,4          | 0,506       | 73,8     | 83,1                |
| Iteration 3 | 248,2          | 0,513       | 74,9     | 82,9                |

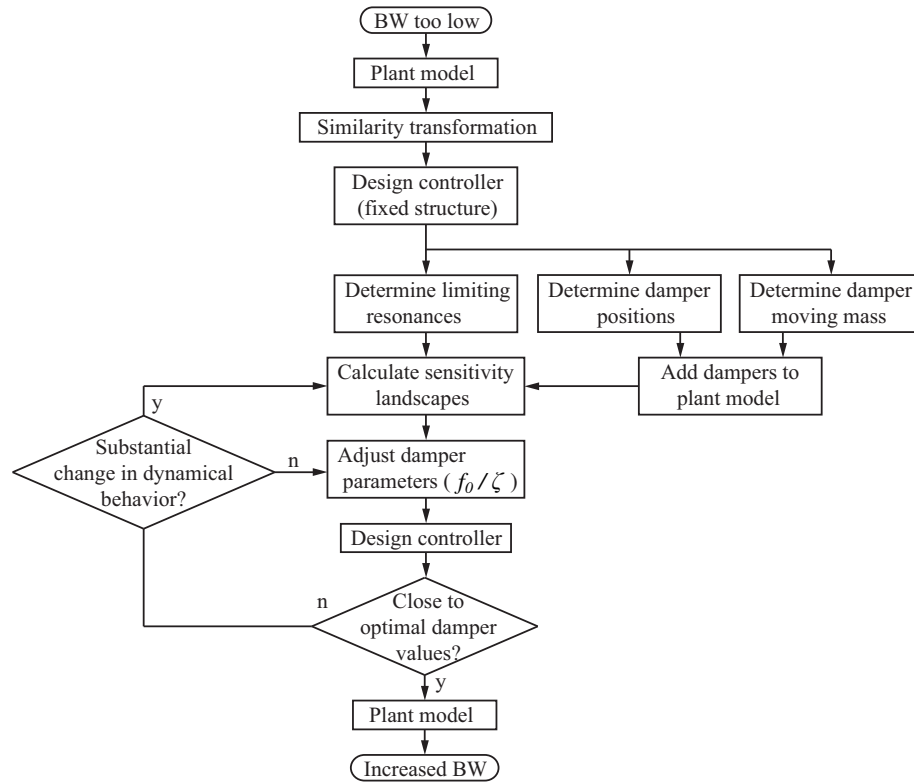


Figure 3.14: Flow chart that describes the iteration procedure.

directions is shown in the right column of Table 3.3. The advantages are only 7 % in contradiction to the z-direction, for which the increase percentage amounts 170 %. This is because these directions are not included in the optimization. Note that the  $\varphi$ - and  $\psi$ -direction show similar behavior due to the symmetry in stage design and damper locations.

### 3.5 Performance results

The initial bandwidth for the undamped plate model was 28 Hz. With this iterative approach, the bandwidth is increased to 75 Hz in 3 iterations. The controller gain is increased by a factor 6.4. Figure 3.15 presents the Nyquist diagram of the system after three iterations. It is visible that the open-loop curve is shaped close around the modulus margin circle of 6 dB. This indicates that the waterbed effect (Bode's sensitivity integral limitation) is fully utilized by the damper design. Figure 3.16 shows the sensitivity functions to illustrate this phenomenon. The sensitivity function of the system with dampers shows much more positive area above 100 Hz, which states that there must be more negative area at lower frequencies, which is clearly visible in the frequency range below 55 Hz. The low-frequency sensitivity function is decreased by 26 dB. Displacement errors with frequencies far below the bandwidth will therefore cause a 20 times smaller position error. The open loops of the damped and the undamped systems in z-direction are presented in Figure 3.17. This figure shows the higher controller gain of the damped system with respect to the undamped system at low frequencies.

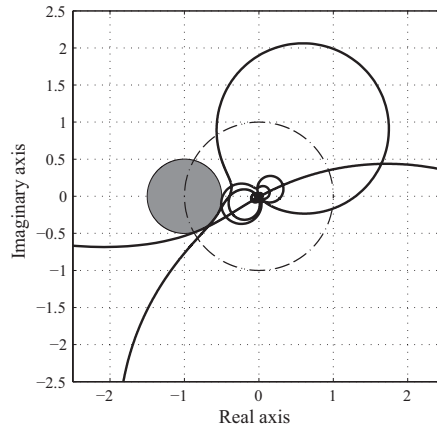


Figure 3.15: Nyquist diagram of the resulting plant after 3 iterations in combination with a controller specifically designed for this plant. The bandwidth amounts 76 Hz in this case.

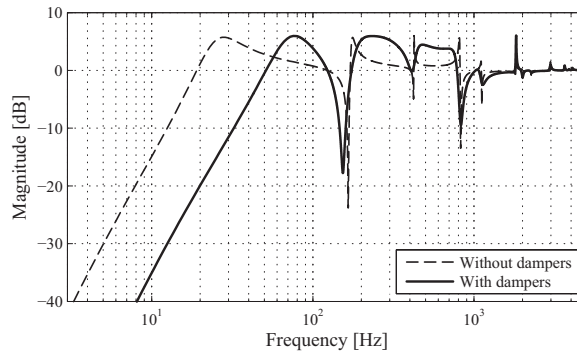


Figure 3.16: Magnitude diagram of both sensitivity functions. The dashed line represents the plant without dampers with its controller, and the continuous line represents the sensitivity of the plate with dampers with its controller.

Note that the amplitude values of the resonance peaks roughly show the same amplification for these open-loops.

The RMDs change the dynamic behavior of the stage. This is visible in the decoupled frequency response functions in  $z$ -direction. Therefore, the RMD dynamics can be expressed as a virtual filter that changes the undamped plant in  $z$ -direction. Figure 3.18 presents this behavior and shows a relatively complex response which is difficult to create by controller design and, if possible, it increases the controller complexity substantially. Moreover, this behavior is very robust due to the introduction by RMDs, in contradiction to a large number of notch filters.

### 3.6 Concluding remarks

This chapter presented an iterative method to determine damper parameters for closed-loop performance optimization based on a modulus margin criterion. Dampers are added with a joint mass of less than 1.5 % of the motion stage mass. This indicates that substantial bandwidth increases are possible with adding small amounts of mass. The controller gain is



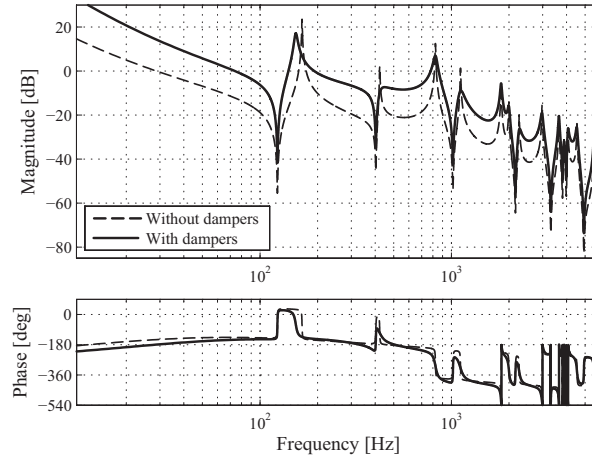


Figure 3.17: Bode diagram of the open-loops of the undamped and damped system. The low-frequency gain difference is clearly visible in this figure.

increased in three iteration steps resulting in a bandwidth increase from 28 Hz to 75 Hz. The difference in RMD properties with respect to the values presented in Chapter 2 mainly result in performances differences in the rotational directions.

The sensitivity based iterative method provides an analysis tool to adapt the plant with decoupling included. This adapts the SISO frequency response functions in logical coordinates.

The step responses are shown in Figure 3.19. This figure shows that:

- both systems are closed loop stable,
- the step response is more than 3 times faster for the damped stage, with the same amount of overshoot.

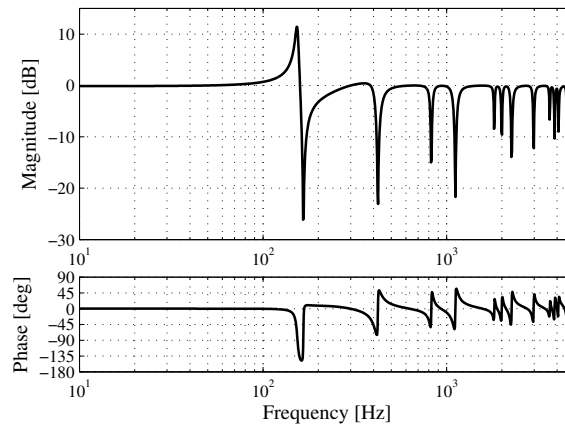


Figure 3.18: Bode diagram of the virtual filter in z-direction that is added to the plant by the dampers.

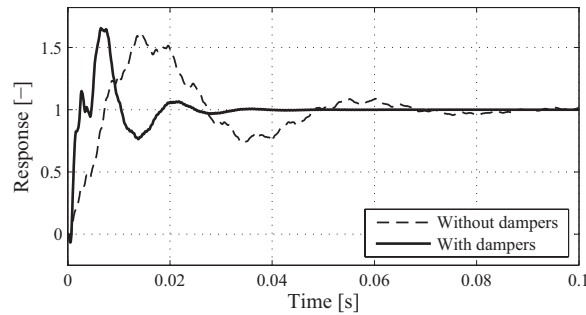


Figure 3.19: Step responses of both closed-loop systems.

### 3.7 Discussion

#### 3.7.1 Results and models

The result of the optimization procedure as shown is strongly plant dependent. In addition, it depends on the available RMD locations. Another point of view is that the amount of damper mass will strongly vary per plant: if a good damper location cannot be used, the damper mass should be increased to compensate for this effect.

The sensitivity landscape that is calculated during the last iteration step shows the robustness of the plant with respect to damper parameter variations. If the minimum value is located in a sharp notch, the behavior will vary strongly as function of parameter changes.

An advantage of this iterative approach, in contradiction to fully automated optimization, is that the user develops understanding of the plant limiting behavior by adapting its dynamical behavior during the iteration procedure, and obtains insight in the maximum suppression factor that can be obtained with the chosen damper parameters and locations. If necessary, the plant's mechanical design and input/output selection can be reconsidered to start the iteration procedure with a plant that shows already more desirable dynamical behavior and increases the effectiveness of the iteration procedure.

A certain suppression factor increase of the resonances is possible by adding dampers and a certain BW increase can be obtained. However, the damper models as used show a low level of realism. The models as applied in this chapter contain:

- purely viscous dampers,
- no mounting mass included.

The mounting mass represents structural material that is needed to connect the moving damper mass to the stage. This mass increases the undamped stage mass, which decreases the undamped natural frequencies and, therefore, increases the difficulty to obtain a high bandwidth.

The damping principle is assumed to show purely viscous behavior. Realistic applications of dampers often show non-ideal viscous behavior. If these properties are changed: i.e., materials with not purely viscous damping and increased mounting masses, the effect of the dampers

will decrease. The main question is to what extent these phenomena will affect the damper performance.

An advantage of this approach is that there is hardly any limit on the plant complexity. State space models of complex mechanical structures can be processed in the same way as the plate in this example.

The difficulties in more complex cases arise in the modal analysis. The  $A$ -matrix of the modal state-space description contains the natural frequencies and therefore will not be larger in case of a larger FEM model in terms of elements or nodes. The sizes of the  $B$ - and  $C$ -matrices are determined by the number of actuators and sensors, and are therefore also independent of the complexity of the FEM model. During the damper coupling procedure the  $A$ -matrix slightly increases in size: the natural frequencies of the damper mechanisms are added to the overall model and become represented in the  $A$ -matrix.

### 3.7.2 Approach

In the example as shown, the decision was made to fix the number of controller components on beforehand, i.e., to apply a fixed structure controller. This approach clearly shows the improvements that are obtainable by adapting the plant dynamics only. Each iteration step results in an optimal result for that specific iteration, which results in an improved behavior over all iteration steps. However, caused by the strong influence of the controller in the landscape calculation, every step results in a local minimum.

In the iteration phase there is no limit on the controller complexity. Although the example in this chapter is elaborated upon using a  $PID^+$  controller, more complex controller structures are applicable to perform the iterations. Even the case of changing the controller structure between two iteration steps is possible. In the first iteration step for instance a  $PID^+$  controller can be used and in the second iteration a  $PID^+$  with notch filter, if this seems to be useful. This might change the shape of the sensitivity landscape and, therefore, improve the performance further.

The presented approach has an iterative character and the controller is a main part of the iteration procedure. This implies that the results depend on the controller structure chosen. During iteration there is no guarantee that a global minimum of the sensitivity function is found. On the other hand, if the range of damper frequency and damping is chosen large enough – at least as large as the frequency range of the NRB dynamics – at least a global minimum is found in every single iteration step. Two important properties can be stated for this procedure:

- the performance cannot decrease in an iteration step with respect to the previous iteration. The worst case possible in a single iteration step shows a minimum value in the landscape of 6 dB. This means that no further improvement is possible and that this iteration step will result in the same frequency and damping values as the previous step. This approach guarantees that the robustness margins are satisfied after each iteration step,

- if the iteration procedure is started with a stable controller for the undamped system, the overall stability of the closed-loop system is guaranteed by the procedure.



# Linear Viscoelastic Characterization of an Ultra-high Viscosity Fluid

**Abstract** - This chapter presents the use of a state-of-the-art damper for high-precision motion stages as a sliding plate rheometer for measuring linear viscoelastic properties in the frequency range of 10 Hz – 10 kHz. This is an example of reversed engineering, i.e., turning a machine part into a material characterization device. Results are shown for a high viscosity fluid. The first part of this chapter describes the damper design based on a Newtonian, high viscosity fluid. This design is flexure-based to minimize parasitic nonlinear forces such as hysteresis and stick-slip. Design and the damping mechanism are elaborated and a model is presented that describes the dynamical behavior. The undamped behavior of the damper is characterized and next, the viscoelastic fluid behavior is included. In the second part of the chapter, linear viscoelastic fluid characterization by means of the damper setup is presented. Measurements are performed and model parameters are fitted by a global optimization algorithm in order to obtain the frequency dependent behavior of the fluid. The resulting fluid model is validated by comparison with a second measurement with a different damper geometry. This chapter shows that linear viscoelastic fluid characterization between 10 Hz and 10 kHz for elastic high-viscosity fluids is possible with a motion stage damper for which the undamped behavior is known.

#### 4.1 Introduction

The functionality of electronic devices has manifold over the past decades. Simultaneously, the cost of the electronic components, used to assemble these devices has decreased. The critical step in the production process of integrated circuits (ICs) is the illumination process of the IC pattern on the surface of a substrate, i.e., a wafer. These improvements – increased functionality and decreased production cost – are based on 1) a decrease in feature size which can be illuminated on the wafer surface and 2) an increase in throughput, respectively. Both accuracy and production speed have been increased continuously. This trend drives the performance of the lithographical devices to the limits of nowadays possibilities. The main part of a lithographical device is a motion stage, which positions the wafer with respect to the optical path. In order to guarantee further improvements, new technologies have to be developed in motion stage design and motion stage control. To explain one of the important limiting factors in more detail a schematic picture of a motion stage is introduced, see Figure 4.1.

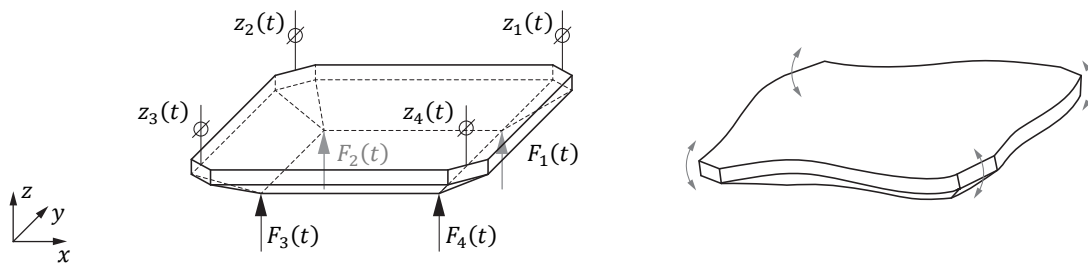


Figure 4.1a: Schematic representation of a motion stage. Actuators and sensors in z-direction are indicated in the figure.

Figure 4.2b: Impression of dynamic deformation of the motion stage during operation.

Figure 4.1a shows the mechanical structure of a motion stage with four force actuators, working in z-direction, indicated by the arrows, to position the stage. Four position sensors are indicated on the stages' corners. A feedback control system, not shown, is used to stabilize the motions and guarantee performance in terms of position accuracy. The controller uses the difference between the actual position and the desired position – the position error – as input, and transforms this information into an actuator current to force the position error to zero. The controller acts as a frequency dependent gain and ideally it should be designed as high as possible to prevent large position errors: the higher the controller gain, the faster the motion stage reacts on a position error. From a mechanical point of view, the motion stage can be assumed as a rigid body for low frequencies: the stage follows a set-point or reference signal without showing internal deformations. At higher frequencies, however, the stage structure shows flexible behavior [16], which is illustrated in Figure 4.1b. The flexible behavior is a result of the limited stiffness of materials in combination with the mechanical design of the motion stage and results in specific resonance frequencies, also called natural frequencies that correspond to deformation shapes, the mode shapes.

#### 4.1.1 Increasing the modal damping

Ultimately, the gain of the position controllers is limited by these natural frequencies. Therefore, these restrict the reaction speed of the motion system. Complex control approaches can be used to deal with this behavior to increase the bandwidth as far as possible [10,65], while retaining robustness [55,108]. In addition, optimization methods are applied to improve the controller performance [91]. The extent to which the resonances limit the controller gain depends on 1) the structural design of the stage [33], 2) the position of actuators and sensors [101], and 3) the damping present in the mechanical structure [22]. High natural frequencies and high modal damping values enable high controller gains. Current motion stage designs are designed to have high natural frequencies [69] and, therefore, are based on materials (i.e., ceramics) with a high specific stiffness. These materials, however, usually contain low material damping. A solution is to optimize the combination of natural frequencies and the controller [15]. Another way to improve a systems' behavior is by increasing the damping of the mode shapes. This type of damping is called modal damping. A drawback of low modal damping is that vibrations in the stage show large amplification factors and continue for a long time. This is detrimental to the transient response of the motion system. These observations lead to a continuous research effort to increase damping in mechanical designs [42,87]. One method to add damping to a range of resonance frequencies is by adding separate dampers [104]. This chapter shows a method in which the damping of the resonances is increased by adding mechanical damping units to the motion stages' corners. Figure 4.2 gives a schematic representation of this idea. Although this principle is known as tuned-mass damper systems in case of single mode suppression, here we use robust-mass dampers which have a very high damping and provide broad band damping effects. The units consist of a mass, mounted on a parallel spring-damper configuration. The frequency range in which the damping has to be increased for realistic applications is typically between 1 and 10 kHz. First of all, the damper behavior has to be linear in order to damp small as well as large amplitudes. This property is also beneficial for system analysis and design: non-linear analyses are more difficult and time-consuming. In addition, most practical control design strategies are based on linear theory [86]. This linearity requirement implies that viscous instead of structural damping has to be applied. The next challenge is the small volume in which the damping mechanism has to fit. The third challenge is the relatively high damping value that has to be realized in that small volume. As solution to these problems we propose a fluid damper design based on an ultra-high viscosity Newtonian fluid. The RMD's geometrical design in combination with the high fluid viscosity should result in the intended damping value.

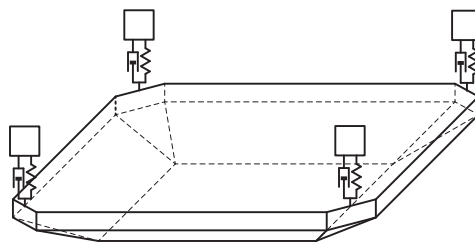


Figure 4.2: Schematic model of a motion stage with 4 dampers added on the corners.



#### 4.1.2 Linear viscoelastic fluid

This solution seems to be suitable to fulfill the three requirements, but it has to be taken into account that the properties of the damper, as function of frequency, might depend on the linear viscoelastic behavior of the applied fluid. Only linear viscoelastic (LVE) behavior is considered since the strains will be small. Therefore, the linear viscoelastic behavior of the fluids applied has to be determined. Different types of instruments are available to measure the LVE characteristics of a fluid, depending on the samples' viscosity and the frequency range of interest. In the low-frequency range (less than 10 Hz), different types of dynamic viscometers are applied [29,64]. In the high-frequency range (10kHz-200 kHz), generally used for the investigation of microstructures and their interactions, a number of instruments based on quartz crystals and nickel tube resonators are available [67,90]. These instruments however measure fluid characteristics at discrete frequencies. Extended setups are available to obtain data at multiple discrete frequencies [31,84,68]. The choice of instruments in the intermediate frequency range (10Hz-200kHz) is limited [12,94,49]. Although the frequency range of some instruments is close to the required range for this application, the range of applicable viscosities is often too low [14].

#### 4.1.3 Chapter outline

A mechanical damper design for broad banded damping based on the application of a high-viscosity fluid is presented in Section 4.2. It is demonstrated that this damper can be used as a (rather cheap) sliding plate rheometer to measure the LVE properties of ultra-high viscosity fluids ( $>100$  Pas) in the frequency range between 10 Hz and 10 kHz. Two different damping mechanisms are presented which enable to change the level of damping. The dynamic model of the damper is described in Section 4.3. The parameters in this model are characterized in Section 4.4 and Section 4.5 presents damped measurements and discusses the linear viscoelastic fluid characterization approach. Parameters for the full damper model are determined by fitting the model on the experimental data. Section 4.6 presents the validation of the resulting LVE spectra, i.e., relaxation times and moduli, for different numbers of Maxwell modes. The model is validated by calculating the behavior of the damper setup with a different damping mechanism inserted and comparing the results with measured data. Conclusions regarding the field of application and the elaboration of the damper setup are given in Section 4.7. Finally, in Section 4.8, the results and methods are discussed and

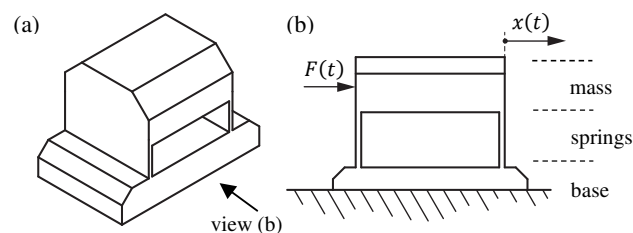


Figure 4.3: a) Isometric view of the main damper parts with the view direction of Figure 4.3b indicated. b) Side view of the damper, which shows the leaf springs.

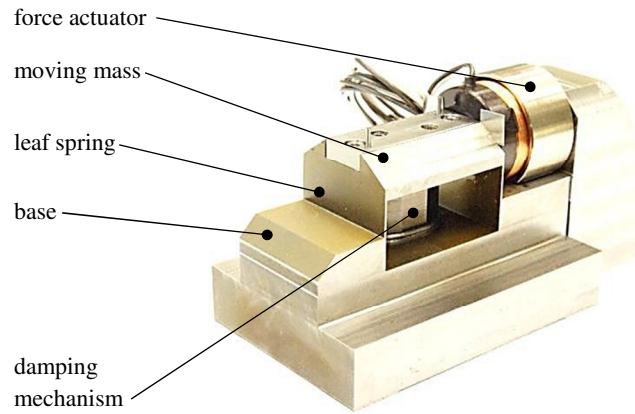


Figure 4.4: Photograph of the damper setup with the different components indicated.

improvements regarding the damper design are addressed.

## 4.2 Damper hardware design

The mass-spring part of the damper is shown in Figure 4.3. We do not elaborate on the underlying ideas for this design since this is outside the scope of this chapter. The full damper assembly consists of a mass, mounted on two springs and a damper in parallel configuration. The mass  $m$  can make small strokes, in the  $x$ -direction and is fixed in all other directions. The spring is a double leaf spring guide. The ratio between the mass  $m$  and the stiffness of the leaf springs in  $x$ -direction  $c$ , determines the natural frequency of the damper mechanism. To identify the behavior of the setup, a force actuator is added, indicated by  $F(t)$  and the position of the mass  $x(t)$  is measured optically. Figure 4.4 shows the final configuration of the damper setup, in which the main parts are indicated. The space between the leaf springs is used to accommodate for the damping mechanism.

A high-viscosity fluid is applied to create a velocity dependent force. For this purpose, the sliding plate principle is used which induces a shear flow: the fluid is placed between two slot

| Table 4.1: Parameters of both fin parts |              |                     |
|---|--------------|---------------------|
|   | Dimension    | Value [mm]          |
| Single fin                              | length - $l$ | 16                  |
|   | width - $w$  | 8.5                 |
|   | gap - $h$    | $120 \cdot 10^{-3}$ |
| Double fin                              | length - $l$ | 16                  |
|   | width - $w$  | 8.5                 |
|   | gap - $h$    | $50 \cdot 10^{-3}$  |

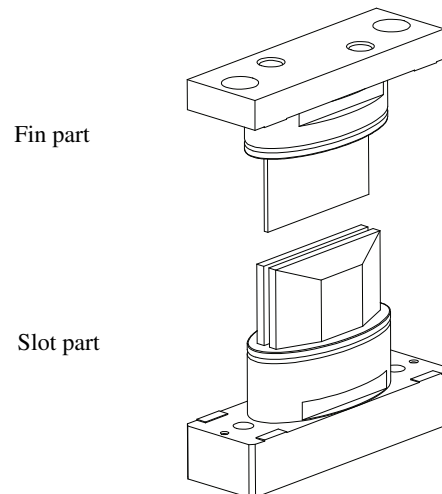


Figure 4.5: Exploded view of the damper parts.

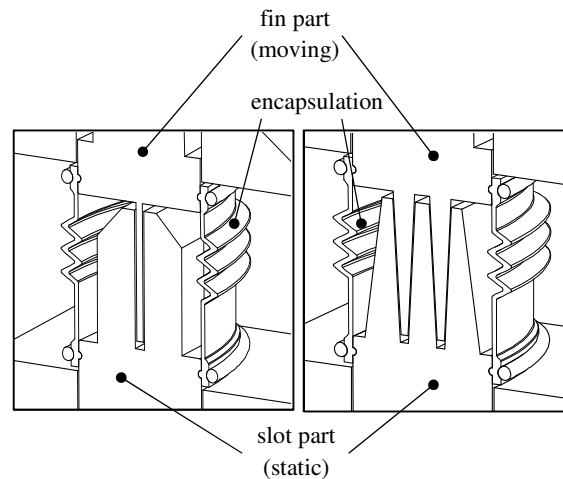


Figure 4.6: Cross-sectional views of the two different damping mechanisms. The single fin – as depicted in Figure 4.5 – is shown in the left figure and the double fin in the right figure.

plates and a fin is positioned between these two plates. These parts are shown in Figure 4.5. A flexible encapsulation is used to hold the fluid between fin and slot part. To study different damping values with the same fluid, two damper designs with different geometries are used. Cross-sectional views of both damper mechanisms are given in Figure 4.6. The left damper contains one fin: the right one two. In addition, the gap width is different in both cases. These two damping mechanisms are both mountable in the same setup as shown in Figure 4.4. The dimensions of these dampers are listed in Table 4.1.

To excite the damper mass, a voice coil is mounted to the hardware which is actuated by a current amplifier. The damper position is measured by a laser vibrometer and the data acquisition is performed by a Siglab system, which provides the signal for the current amplifier and samples the laser-vibrometer at 51.2 kHz. This input signal is also measured to calculate a frequency response. The fluid applied is Rocol Kilopoise 0868 which has a high zero shear viscosity of 220 Pas.

### 4.3 Limits and assumptions

A sliding plate damper for high frequencies introduces side effects which can be divided into two groups: 1) geometry related effects and 2) frequency dependent effects. A first geometrical effect is due to the finite length of the plates. From Table 4.1 it is seen that the ratio length/gap amounts 133 – for the single fin and 320 for the double fin. This ratio is so high that this effect can be neglected. A second geometrical effect is due to the difficulty to get the plates parallel to each other, especially with the normal forces acting on the moving fin, induced by the flow. This design counteracts this problem in two-ways: the damper part is symmetric, which means that the fin normal forces cancel each other. In addition, the double leaf spring mechanism has a very high lateral stiffness, which minimizes lateral displacements. A third geometrical effect is pumping of the fluid, which appears in the case of closed ends and introduces a flow opposite to the fin velocity, and therefore introduces a parasitic damping force. This problem is avoided by letting the gaps' ends open. The fin is shorter than the slot to maintain the same damping area over the damper stroke. The stroke is

assumed to be smaller than 0.5 mm. To avoid problems with the fluid running out, a flexible encapsulation is used which keeps the fluid inside. These effects all arise at low frequencies, at which the flow can be assumed homogeneous. The ratio between inertial and viscous effects determines up to which frequency the flow can be assumed homogeneous. A criterion for the time to establish homogenous, shear flow is given by equation (4.1) [57,85].

$$t_c = \frac{1}{\omega_c} \simeq \frac{10\rho h^2}{\eta} \quad (4.1)$$

in which  $\rho$  describes the fluid density in  $\text{kg/m}^3$ ,  $\eta$  the dynamic viscosity in Pas and  $h$  the gap width in m, Dimensions are provided in Table 4.1. This estimate results in a frequency estimate above 100 kHz for the largest gap width. It shows that high fluid viscosities and small gap widths enable high frequencies without losing homogeneous flow conditions.

#### 4.4 RMD mechanism characterization

##### 4.4.1 Undamped characterization

Two features mainly characterize the dynamical behavior of the setup:

- the mechanical design (mass & stiffness),
- the high-viscosity fluid damper.

In order to measure the behavior of the fluid damper independently, the dynamic behavior of the mechanical part is characterized in advance. For this purpose, two measurements have been performed: one without and one with the fin part mounted. This only changes the moving mass while the stiffness remains the same and therefore, the natural frequency of the mechanism changes. The frequency responses of these two measurements are shown in Figure 4.7. The dashed line shows the transfer function of the mechanism without fin part, and therefore has a higher natural frequency, the black line represents the measurement with fin part added. Different frequency ranges are indicated in the figure:

- the behavior in the low-frequency range is determined by the static stiffness of the leaf springs,
- the resonance behavior around the natural frequencies is clearly visible as peaks in the frequency responses,
- at higher frequencies the behavior is dominated by the moving mass,
- at even higher frequencies, higher order dynamics is observed.

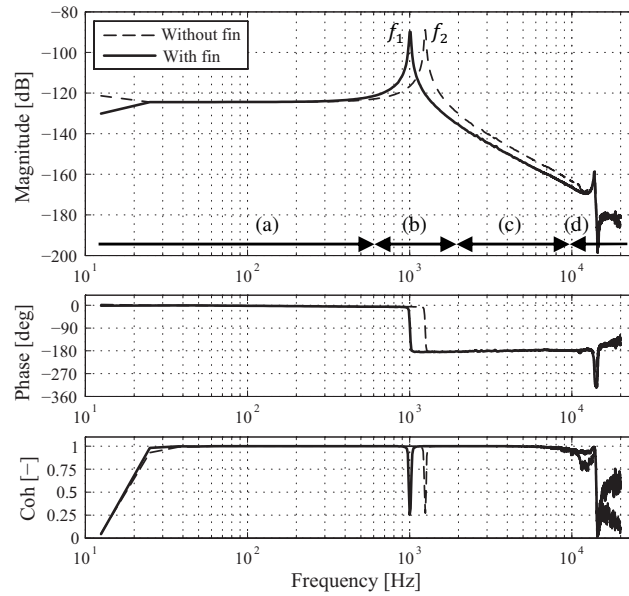


Figure 4.7: Two measured frequency responses of the undamped mechanism: without fin (dashed line) with fin (solid line). The natural frequencies are indicated by  $f_1$  and  $f_2$ . The middle figure shows the corresponding phase. The lower figure shows the coherence of the measurements. The upper plot indicates ranges in which the following system properties are dominant: (a) the stiffness, (b) the resonance, (c) the mass, (d) high order dynamics.

The lower figure shows the coherence of the two measurements, which is a measure of the quality of the measurement. The value of the coherence is close to 1 in the frequency region between 25 Hz and 15 kHz, which indicates that the measurement quality is quite good in this range.

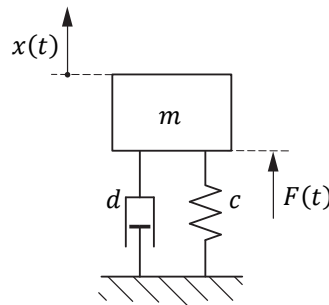


Figure 4.8: Simplified damper model with a mass, spring and dashpot.

#### 4.4.2 Lumped mass model

A simple lumped mass model, visualized in Figure 4.8, describes the behavior of the unit without the viscous damping mechanism. Due to the low damping of the mechanism, the behavior is dominated by the stiffness  $c$  and the mass  $m$ . Therefore, the two resonance frequencies,  $\omega_1$  and  $\omega_2$ , can be determined with high precision. These two frequencies, combined with the mass difference between the two measurements  $\delta m$ , contain enough information to calculate the stiffness  $c$  and mass  $m_2$  of the undamped setup without fin part, see (4.2) and (4.3):

$$\begin{bmatrix} 1/\omega_1^2 & -1 \\ 1/\omega_2^2 & -1 \end{bmatrix} \begin{bmatrix} c \\ m_2 \end{bmatrix} = \begin{bmatrix} \delta m \\ 0 \end{bmatrix} \quad (4.2)$$

$$m_1 = m_2 + \delta m \quad (4.3)$$

Subsequently, the modal damping can be determined by calculating the amplification factor at the resonance frequency. Table 4.2 presents the data as calculated from the measurements. This data is used in the subsequent steps as the model is extended. The modal damping can be estimated by the amplification factor at the resonance frequency, which is called the Q-factor. This equation reads:

$$Q = \frac{1}{2\zeta} \quad (4.4)$$

The amplification in both cases amounts 36 dB: this indicates that the modal damping of the system amounts 0.79 %. This damping is transformed into a physical damping value in Ns/m and included in the damper state space model.

Linear viscoelastic (LVE) rheological behavior of a fluid, i.e., the relation between stress and strain and strain rate, is described with the well-known multi-mode Maxwell model [57], see Figure 4.9 for a schematic picture. The Maxwell model is expressed in terms of material parameters for the elasticity  $G_0$  in Pa and the viscosity  $\eta_0$  in Pas.

Table 4.2: Parameter values of the undamped mechanism

|                   |          | without fin | with fin | Unit |
|-------------------|----------|-------------|----------|------|
| Natural frequency | $\omega$ | 1212        | 989      | Hz   |
| Stiffness         | $c$      | 1,67e6      | 1,67e6   | N/m  |
| Mass              | $m$      | 28,8        | 43,3     | g    |
| Damping           | $\zeta$  | 0,79        | 0,79     | %    |

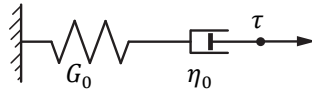


Figure 4.9: Single element Maxwell model in which the spring represents the fluid elasticity  $G_0$  in Pa and the dashpot the fluid viscosity  $\eta_0$  in Pas.

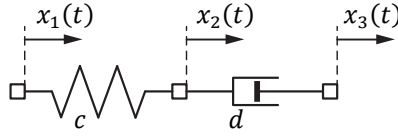


Figure 4.10: Single element Maxwell model in which the spring represents the stiffness of the fluid damper  $c$  in N/m and the dashpot represents the viscous damping  $d$  in Ns/m.

The model in Figure 4.8, however, was derived using equations of motion and describes the displacements and velocities of moving masses and the corresponding parameters are the system properties stiffness  $c$  in N/m and damping  $d$  in Ns/m. Therefore, the Maxwell parameters are transformed into system properties. The transformed single Maxwell element is depicted in Figure 4.10.

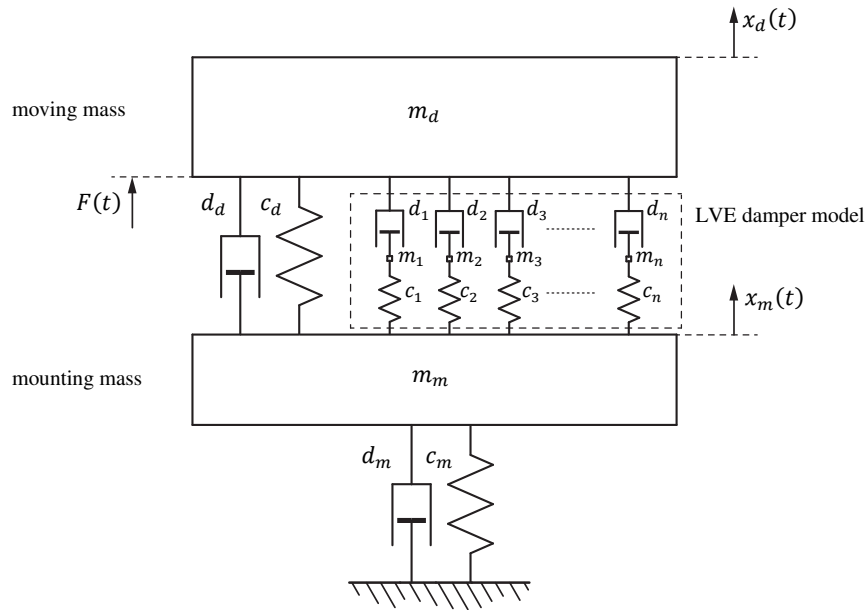


Figure 4.11: RMD model with LVE fluid behavior included in the damper model.

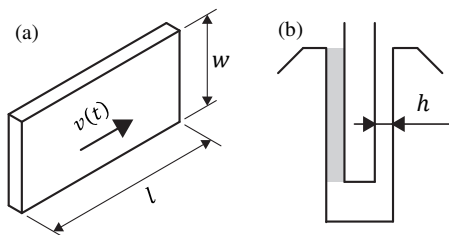


Figure 4.12 a) The fin area and corresponding geometrical parameters and b) the symmetric gap.

#### 4.4.3 Model extension with Maxwell elements

A schematic representation of the extended damper unit model is shown in Figure 4.11 with the Maxwell elements shown in the dashed square. An arbitrary number of Maxwell models can be added to describe LVE properties of the damping mechanism. An additional mass  $m_m$  is added to the model, which represents the mounting mass and contains the slot part. The spring with stiffness  $c_m$  and dashpot with damping  $d_m$  represent the connection to the fixed world or to a motion stage. The springs and dashpots in the LVE damper model create forces as a result of the position differences and velocity differences respectively between the degrees of freedom. In between the springs and dampers in the LVE damper model, additional degrees of freedom – with their corresponding masses ( $m_1, \dots, m_n$ ) – are added to enable the derivation of equations of motion.

These masses balance the force equilibrium between the springs and the dashpots and can be seen as the mass of the fluid. These degrees of freedom are necessary for interconnecting the spring and dashpot elements: the masses should be chosen relatively low to limit their influence and approximate the Maxwell model of Figure 4.9 closely. The corresponding state space matrices are presented in (4.5).

$$\begin{aligned}
 & \begin{matrix} A \\ C \end{matrix} \left[ \begin{array}{cc|cccccc|cc} 0 & 1 & 0 & 0 & \dots & 0 & 0 & \dots & 0 & 0 & 0 & 0 \\ -(c_i + \sum_{j=1}^n c_j)/m_i & -d_i/m_i & c_i/m_i & 0 & \dots & c_i/m_i & 0 & \dots & c_i/m_i & 0 & c_i/m_i & d_i/m_i \\ \hline 0 & 0 & 0 & 1 & & & & & & 0 & 0 & 0 \\ c_i/m_1 & 0 & -c_i/m_1 & -d_i/m_1 & & & & & & 0 & d_i/m_1 & \\ \vdots & \vdots & & & \ddots & & & & & \vdots & \vdots & \\ 0 & 0 & & & 0 & 1 & & & & 0 & 0 & \\ c_i/m_i & 0 & & & -c_i/m_i & -d_i/m_i & & & & 0 & d_i/m_i & \\ \vdots & \vdots & & & & & \ddots & & & \vdots & \vdots & \\ 0 & 0 & & & & & 0 & 1 & & 0 & 0 & \\ c_i/m_n & 0 & & & & & -c_i/m_n & -d_i/m_n & & 0 & d_i/m_n & \\ \hline 0 & 0 & 0 & 0 & \dots & 0 & 0 & \dots & 0 & 0 & 0 & 1 \\ c_i/m_m & d_i/m_m & 0 & d_i/m_m & \dots & 0 & d_i/m_m & \dots & 0 & d_i/m_m & \frac{-(c_i + c_m)}{m_m} & -(d_i + \sum_{j=1}^n d_j)/m_m \end{array} \right] \begin{matrix} B \\ D \end{matrix} \left[ \begin{array}{c} 0 \\ 1/m_i \\ 0 \\ 0 \\ \vdots \\ 0 \\ 0 \\ \vdots \\ 0 \\ 0 \\ 0 \\ 0 \\ 0 \end{array} \right] \\
 & \begin{matrix} C \\ D \end{matrix} \left[ \begin{array}{cc|cccccc|cc} 1 & 0 & 0 & 0 & & 0 & 0 & & 0 & 0 & 0 & 0 \end{array} \right] \begin{matrix} D \end{matrix} \left[ \begin{array}{c} 0 \end{array} \right]
 \end{aligned} \tag{4.5}$$

These matrices can be used in the definition of a state space model:

$$\dot{x} = Ax + Bu \tag{4.6}$$

$$y = Cx + Du \tag{4.7}$$

in which state vector  $x$  represents the vector with displacements and velocities of the masses as presented in Figure 4.11. Input vector  $u$  includes the input force and  $y$  represents the output displacement of the moving mass.



**4.4.4 Separation of geometry and fluid**

The damper model with Maxwell elements contains the system parameters stiffness and damping in N/m and Ns/m, respectively. These properties, however, depend on:

- damper geometry,
- fluid properties.

In order to obtain the fluids' physical parameters, the geometrical properties should be excluded from the solution. For that purpose, the rheological expressions, the storage  $G'$  and loss modulus  $G''$ , for the fluid behavior are introduced. The strain  $\gamma$  and strain rate  $\dot{\gamma}$  in a fluid under harmonic excitation with frequency  $\omega$  is described by:

$$\gamma = \gamma_0 \sin(\omega t) \quad (4.8)$$

$$\dot{\gamma} = \omega \gamma_0 \cos(\omega t) \quad (4.9)$$

in which  $\gamma_0$  is the strain amplitude. The shear stress in the fluid is described by:

$$\tau = \tau_0 \sin(\omega t + \delta) \quad (4.10)$$

in which  $\delta$  is the phase lag of the stress with respect to the strain. This equation can be rewritten as:

$$\tau = \tau_0' \sin(\omega t) + \tau_0'' \cos(\omega t) \quad (4.11)$$

The storage and loss moduli are defined by:

$$G' = \frac{\tau_0'}{\gamma_0} \quad (4.12)$$

$$G'' = \frac{\tau_0''}{\gamma_0} \quad (4.13)$$

For the multi-mode Maxwell model, these moduli can be calculated as function of frequency using:

$$G'(\omega) = \sum_{k=i}^n G_i \frac{\omega^2 \lambda_i^2}{1 + \omega^2 \lambda_i^2} \quad (4.14)$$

$$G''(\omega) = \sum_{i=1}^n G_i \frac{\omega \lambda_i}{1 + \omega \lambda_i} \quad (4.15)$$

in which  $\lambda_i$  presents the characteristic frequencies corresponding to the fluid modes. The magnitude and the phase are given by:

$$|G(\omega)| = \sqrt{G'(\omega)^2 + G''(\omega)^2} \quad (4.16)$$

$$\angle G(\omega) = \tan^{-1} \left( \frac{G''(\omega)}{G'(\omega)} \right) \quad (4.17)$$

The dynamic viscosity values  $\eta_i$  corresponding to the Maxwell modes can be calculated by:

$$\eta_i = G_i \lambda_i \quad (4.18)$$

Figure 4.12 shows the geometrical parameters ( $l, w, h$ ) of the damping mechanism (see also Table 4.1). The relation between the stiffness and damping values in Figure 4.11, and the fluid parameters elasticity and dynamic viscosity are, respectively:

$$c_i = \frac{2lw}{h} G_i \quad (4.19)$$

$$d_i = \frac{2lw}{h} \eta_i \quad (4.20)$$

in which the factor 2 comes from the double sided fin. Finally, the zero shear viscosity of the fluid can be calculated by:

$$\eta_{zs} = \sum_{i=1}^n \eta_i \quad (4.21)$$

i.e., the zero shear viscosity equals the sum of the dynamic viscosities.

#### 4.5 Fluid model calculation

Figure 4.13 shows three measured frequency responses. The solid line represents the undamped behavior with the fin mass added: see Figure 4.7. The other two lines show

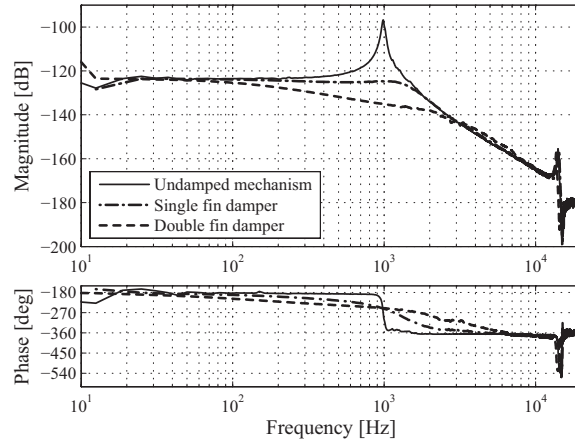


Figure 4.13: Bode diagram with three measurements included. The undamped measurement and two measurements with different damping units are shown. The phase diagram is corrected for time delays introduced during measuring.

measurements with the two different damping mechanisms (see Figure 4.6), including the fluid, inserted. The dash-dotted line shows the behavior of the single fin damper mechanism and the dotted line represents the behavior with the double fin applied.

#### 4.5.1 Model fit

To obtain the behavior of the damping mechanism, the frequency response of the Maxwell model is fitted to the measurement data. This results in the damping parameters, i.e., the stiffness and damping values. The parameters corresponding to the undamped mechanism are applied in the model. Stiffness  $c_m$  is chosen relatively high to simulate a stiff connection between the measurement table and the damper setup. To calculate the fluid behavior, model parameters have to be fitted on the measurement data and this is executed using an optimization algorithm. The complex response as function of the input frequency is measured and presented by the magnitude and the phase diagram. Additional time delays are present in the phase data, caused by finite time delays during measuring. Therefore, to use the phase for fitting, an estimate has to be made for the phase delay. To avoid this unnecessary estimate, the magnitude information is used in the optimization algorithm.

The cost function is defined as:

$$\min_x J(x) \quad (4.22)$$

In which parameter vector  $x$  contains the parameters for the springs and dampers:

$$x = [c_1 \quad \cdots \quad c_n \mid d_1 \quad \cdots \quad d_n]^T \quad (4.23)$$

The parameter space is defined as:

$$lb \leq x \leq ub \quad (4.24)$$

Further equality and inequality constraints are not included. In the definition above, the cost function is defined as:

$$J(x) = |(\|R_{meas}\|^2 - \|R_{mod}(x)\|^2)|_\infty \quad (4.25)$$

In this equation  $R_{meas}$  and  $R_{mod}(x)$  describe the vectors with complex response data of respectively the measurement and the model as function of the frequency. The maximum value of the absolute error between the vectors with model data and measurement data is used for cost function evaluation. The length of parameter vector  $x$  amounts two times the number of Maxwell modes: the stiffness and damping are included for every single mode. In this optimization criterion all spring stiffness values in N/m and damper values in Ns/m can be chosen freely which implies that the time constants of the fluid modes are not determined on beforehand. Although the best fit for a fixed number of Maxwell modes is guaranteed by this approach, it does not necessarily result in a frequency equally spaced distribution of the time constants of the modes. This optimization calculates  $c_1 \cdots c_n$  and  $d_1 \cdots d_n$  such that the magnitude of (4.5) fits on the magnitude plot of the damped measurement shown in Figure 4.13. Masses ( $m_1, \dots, m_n$ ) are determined beforehand and are not included in the optimization parameters.

#### 4.5.2 Optimization approach

An optimization algorithm has to be chosen to find the minimum value of the cost function as presented in (4.25). For this purpose, the properties of this function have to be investigated. The simplest function in this optimization formulation is a damper model with a single Maxwell element. This results in an optimization problem with two independent variables: a stiffness value and a damping value. The cost function for this 2-parameter problem can be visualized in a 3D-surface, which gives an impression of the complexity, continuity and convexity of the cost function. The resulting surface is shown in Figure 4.14, which shows the error of the fit with respect to the measurement for a grid of parameter values. The  $x$ - and  $y$ -axis are scaled logarithmically. The damper value ranges  $1e1 - 1e6$  Ns/m, the stiffness  $1e5 - 1e9$  N/m. The most important property regarding the choice of the optimization algorithm is the convexity property. Figure 4.14 shows that, within the parameter space studied, more local minima exist. To illustrate this in more detail, a contour plot of the error is given in Figure 4.15. Three gradient-based optimizations are performed with slightly different starting points, indicated by the arrow. The three resulting optima are different: only optimization path 3 shows the trajectory to the global minimum. This proves that this problem has a non-convex

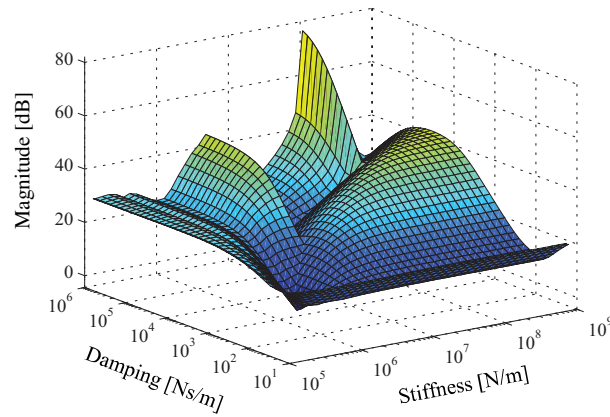


Figure 4.14: Error landscape between the measurement and the model for a single Maxwell element damper. The  $x$ - and  $y$ -axis represent the stiffness and damping values on logarithmic axes. The  $z$ -direction shows the absolute error  $J(x)$  in dB between the measurement and the fit in decibels.

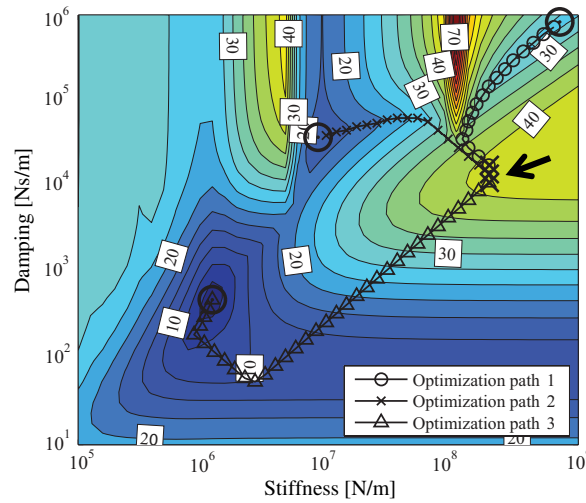


Figure 4.15: Contour plot of the error landscape of Figure 4.14. Three optimizations are plotted in order to show the non-convex behavior within the optimization field. The three lines start at slightly different points (indicated by the arrow) and end up in three different minima.

character, even in case of a single mode Maxwell description. Therefore, non-convexity is assumed in case of more Maxwell modes too. In addition, discontinuous behavior is visible within the parameter space. These properties: discontinuity and non-convexity, require a non-convex optimization algorithm in order to try to find the global minimum. A hybrid optimization procedure is applied, which starts with a genetic algorithm (GA) [9] to deal with the problem of multiple local minima. Although, in general, this type of algorithms do not guarantee that the global optimum is found, its efficiency can be influenced by choosing the correct algorithm parameters and initial population size [28]. After a number of iterations, the solution of the GA is assumed to be in the vicinity of the global minimum and is used as starting point for a gradient-based optimization procedure [75]. For this specific problem the parameter space is completely feasible. This is an advantage, just as the absence of equality

Table 4.3: Convergence of the error as function of increasing number of Maxwell elements.

| # Modes | Error [dB] |
|---------|------------|
| 1       | 3,32       |
| 2       | 0,94       |
| 3       | 0,40       |
| 4       | 0,41       |
| 6       | 0,41       |

constraints. This avoids problems how to deal with infeasible parts of the parameter space and increases the convergence rate of the algorithm.

#### 4.5.3 Resulting fluid model

First, a single Maxwell element has been fitted. An impression of the measurement and the model estimate are shown in Figure 4.16. The maximum value of the error, after optimization, amounts 3.35 dB. A part of the frequency range, between 2200 and 3400 Hz, is excluded from the cost function: the measurement shows parasitic dynamics in this frequency range due to the finite stiffness of the table on which the whole setup is fixated. To decrease the error, a 3

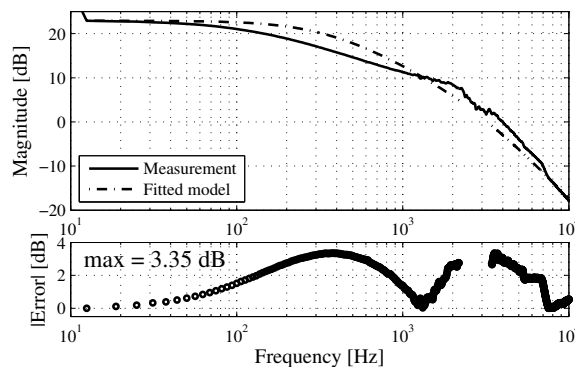


Figure 4.16: Bode diagram of the measurement and single Maxwell mode fit of the damped behavior with the double fin setup. The upper plot shows the magnitude. The fitted behavior is shown by the dash-dotted line. The lower plot shows the error as function of the frequency with a maximal error value of 3.35 dB.

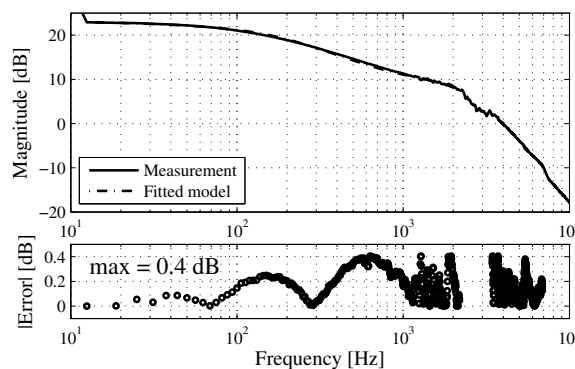


Figure 4.17: Bode diagram of the three Maxwell mode fit on the same measurement as shown in Figure 4.16. The maximal error value amounts 0.40 dB.

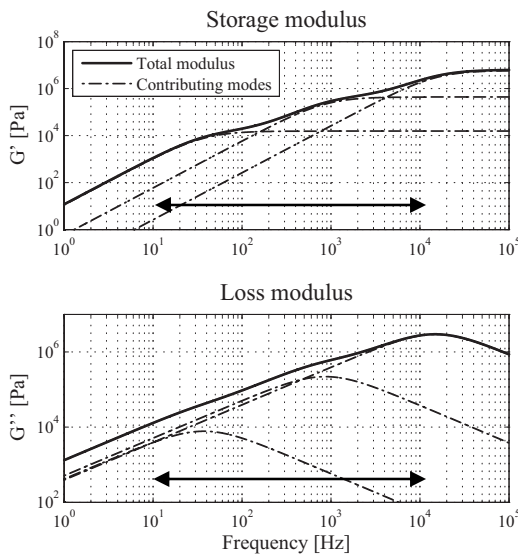
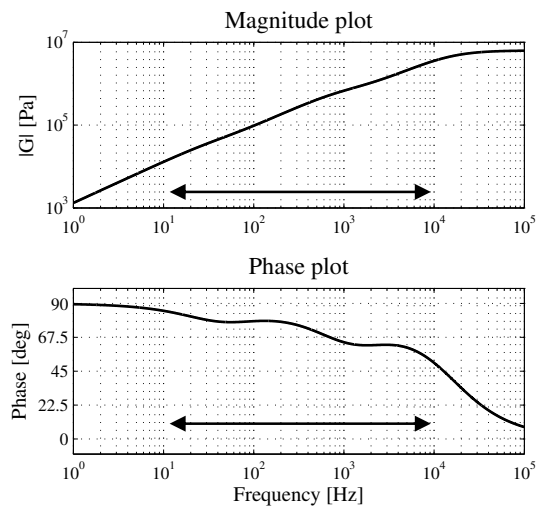
Table 4.4: Resulting parameter values for the springs and dampers and the corresponding fluid parameter values.

|                         | M#1    | M#2    | M#3     |      |
|-------------------------|--------|--------|---------|------|
| $C$                     | 1.51e5 | 4.29e6 | 5.72e7  | N/m  |
| $D$                     | 646.6  | 790.5  | 607.4   | Ns/m |
| <b>Fluid parameters</b> |        |        |         |      |
| $G$                     | 15538  | 4.41e5 | 5.87e6  | Pa   |
| $\eta$                  | 66.3   | 81.1   | 62.3    | Pas  |
| <b>Time constants</b>   |        |        |         |      |
| $\lambda$               | 4.3e-3 | 1.8e-4 | 1.06e-5 | s    |

element Maxwell model – 6 parameter optimization – is fitted on the measurement data. The result is shown in Figure 4.17. The error has decreased to 0.40 dB, which is a reduction of 8 times with respect to the result of the one Maxwell element model. The error development as function of the number of Maxwell elements is shown in Table 4.3, which shows that the error value saturates at three Maxwell elements. More elements do not improve the solution further and show a certain noise level with more than 3 modes. Figure 4.17 shows that the measured behavior is well captured.

As described in (4.19) and (4.20), the fluid parameters  $G_i$ ,  $\eta_i$  can be calculated using the geometrical data  $l$ ,  $w$ ,  $h$  of the damping mechanism. The time constants  $\lambda_i$  of the different modes are calculated using (4.18). The resulting fluid parameters are listed in Table 4.4.

The zero shear viscosity amounts 209,7 Pas, see (4.21). This value underestimates the specified value by 4.7 %. Figure 4.18 shows the storage and the loss moduli as function of the frequency. The compound behavior as well as the contributing modes are presented. The frequency range in which the measurement is taken with good quality is indicated in the figure. The magnitude and phase of the complex modulus  $G^*$  are given in Figure 4.19. The

Figure 4.18: Storage modulus  $G'(\omega)$  and loss modulus  $G''(\omega)$  with the separate modes.Figure 4.19: Magnitude and phase of modulus  $G(\omega)$ .

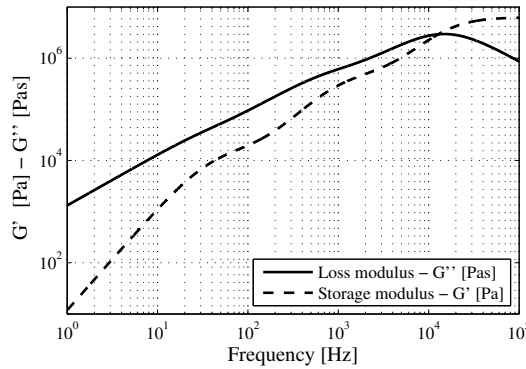


Figure 4.20: Storage and loss moduli.

Table 4.5: Resulting fluid model values for the single fin measurement

|        | M#1    | M#2   | M#3    |     |
|--------|--------|-------|--------|-----|
| $G$    | 3,49e5 | 30,35 | 2,72e9 | Pa  |
| $\eta$ | 69,5   | 5e-4  | 70,9   | Pas |

phase plot clearly shows the amount of damping as function of the frequency. At low frequencies the phase equals 90 deg, which implies pure viscous behavior. The phase decreases for higher frequencies, which indicates the linear visco-elastic frequency range. After 12 kHz, the phase crosses 45 deg and sharply decreases: the damping vanishes and the fluid becomes elastic.

This 45 deg crossing is also visible in Figure 4.20, in which the storage modulus exceeds the loss modulus after 12 kHz. Figures 4.18 – 4.20 show a frequency range between 1 Hz and 100 kHz to show the different Maxwell modes and their compound behavior. However, the cost function is defined between 20 Hz and 7 kHz, and the damper behavior is only fitted in that frequency region. Therefore, the fluid model should only be considered accurate in this frequency region only.

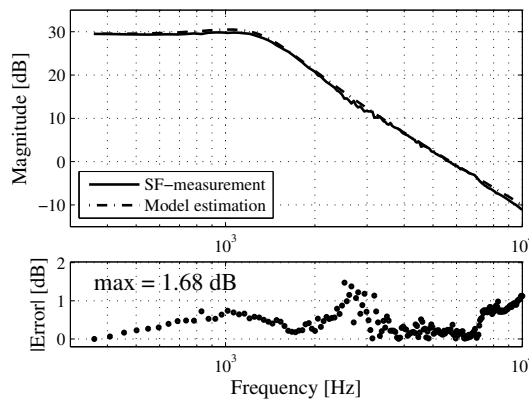


Figure 4.21: Damper measurement with the single fin mechanism – continuous line – and the predicted behavior with the derived fluid model shown by the dash-dotted line. The lower plot shows the error between the prediction and the measurement.



## 4.6 Fluid model validation

### 4.6.1 Double fin model validation

As shown in Figure 4.6 and 4.13, two damper geometries were designed and two measurements are performed: one with the double fin damping mechanism and one with the single fin damping mechanism. In the previous section, the double fin measurement was used to derive a fluid model. In order to validate this fluid model, the reverse approach is applied: the fluid model is used to predict the behavior of the damper with the single fin mechanism inserted and compared with the measurement. In Figure 4.21 both lines are shown. The magnitude figure shows that the model provides a quite good estimate of the measured behavior of the damper. The maximum error amounts 1.7 dB, see lower plot. This relatively small error indicates that the fluid model is good enough to predict the damper behavior over this frequency range.

### 4.6.2 Single fin fit and validation

The fitting procedure of Section 4.5 is repeated on the single fin measurement to obtain a second model of the Rocol fluid. The result is shown in Figure 4.22a. The maximal absolute error after optimization with three modes amounts 0.88 dB. The resulting fluid model parameter values are listed in Table 4.5.

The zero shear viscosity amounts 140,4 Pas. This value is 36 % lower than specified. This model is verified by estimating of the behavior of the double fin setup and comparing the result with the measurement of the double fin setup. Figure 4.22b shows this comparison. The maximal error between the predicted behavior and the measurement amounts 2.3 dB and appears at approximately 3500 Hz. This error is 36 % larger than the error in Figure 4.21, which shows predicted behavior with the double fin fluid model. The error plot in Figure

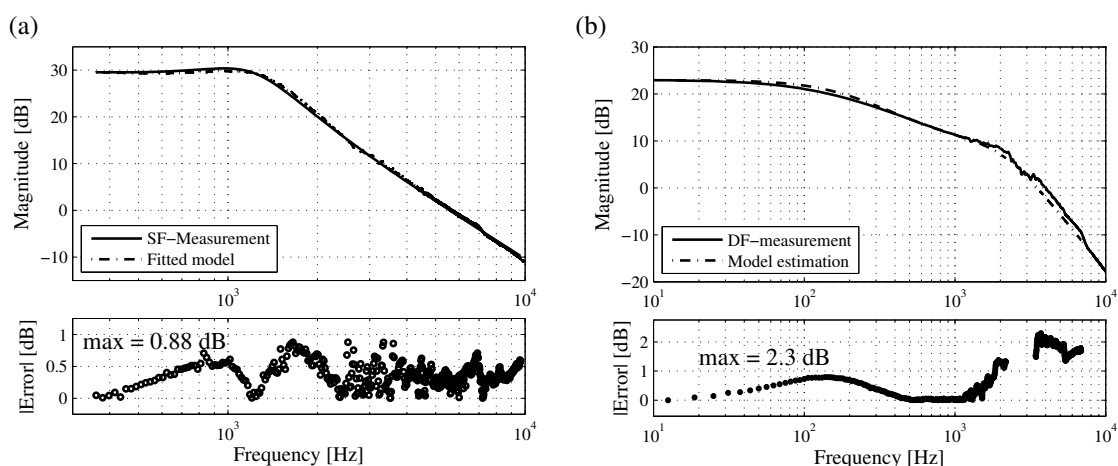


Figure 4.22a: Damper measurement with the single fin mechanism and the fitted behavior with a three mode model. The lower plot shows the absolute error between the measurement and the fit.

Figure 4.22b: Measurement of the double fin mechanism – continuous line – and the predicted behavior shown by the dash-dotted line. The lower plot shows the absolute error value between the prediction and the measurement.

4.22b shows an error increase for higher frequencies. Below 2 kHz the error value does not exceed 1 dB. Especially for frequencies between 3,5 and 7 kHz, the error value is fluctuating around 2 dB. This indicates that the fluid model is more accurate in the frequency range between 200 Hz and 2 kHz than it is for higher frequencies. This phenomenon can be understood when taking a closer look at Figure 4.13. This figure shows two damped measurements and one undamped measurement. At 2 kHz and above, the magnitude of the undamped measurement and the magnitude of the single fin measurement show the same behavior which is determined by the mass line. This indicates that there is hardly a difference between those two behaviors and, therefore, it is difficult to identify the fluid behavior in this frequency region.

#### 4.7 Concluding remarks

A design of a sliding plate damper that can be used to characterize LVE fluid behavior of high viscosity fluids in the frequency range between 10 and 10e3 Hz, i.e., it can be used as a rheometer, is presented. The drawbacks of standard sliding plate devices are taken care off by the mechanical design: elastic elements are applied to enable a measurement stroke combined with stiff guidance in other directions. This flexure mechanism very precisely determines the position of the fin with respect to the slot part. Linear viscoelastic fluid characterization of a high-viscosity fluid is performed in a frequency range from 10 Hz to 10 kHz. In this frequency range of 3 decades, a three-mode Maxwell model can accurately describe the behavior. The fluid model obtained by the double fin setup appeared to be much more accurate than the fluid model obtained by the single fin measurement. The fluid model resulting from the double fin measurement shows a zero shear viscosity of 209.7 Pas. This indicates that at least most of the linear viscoelastic behavior and, therefore, LVE frequency region of the fluid is captured in the frequency range that has been fitted. The obtained LVE fluid models are applicable in the design procedure of dampers for future motion systems.

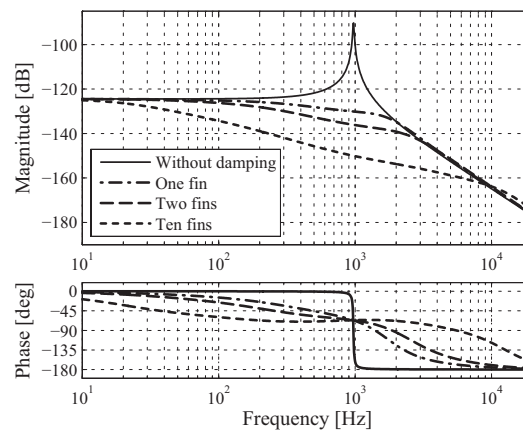


Figure 4.23: Damper transfer functions based on the three mode fluid model. The dotted line shows behavior for a damping mechanism with ten fins. This curve shows a larger frequency range that is dominated by the damping behavior.

## 4.8 Discussion

This chapter shows a sliding plate damper design that is used as a rheometer to measure the LVE properties of a high-viscosity fluid in the frequency range between 10 Hz and 10 kHz. Resulting fluid parameters, in terms of a Maxwell spectrum, of a high-viscosity fluid are presented.

Even in case of an underestimated zero shear viscosity, no fluid modes should be added above 7000 Hz if the measurement is not of good quality in that region. A lack of HF modes causes the phase to decrease after the last mode, and the model under-estimates the damping if a mistake is made: it is the safest mismatch with respect to model use in future motion stage design.

The resulting fluid models are applicable in the design of industrial dampers for motion stages. This is demonstrated in [104]. Although the presented fluid models are applicable in design procedures, improvements can be made regarding the damper design, which might improve the quality of the models further. To derive the fluid model the damper displacement is measured. The displacement graphs show, as function of frequency, successively, a region dominated by the stiffness, one dominated by the damping and one dominated by the mass. The damping behavior is dominant around the damper's resonance frequency. The single fin measurement and the double fin measurement and their validations show that a higher damping value leads to a larger damping dominated frequency region and, therefore, to a more accurate fluid model. Figure 4.23 shows model calculated behavior of respectively: the undamped, single fin and double fin displacements with an additional line for a hypothetical setup with 10 fins. This shows that the damping becomes more dominant and therefore can be separated from the measurement with higher accuracy, especially at frequencies further from the resonance frequency. Figure 4.23 shows that the damping behavior can be distinguished more accurately in the frequency regions 10-100 Hz and 3-10 kHz. This results in a higher quality of the fluid model, at least in these regions. Related to this observation is the question about the viscosity range of fluids that can be measured in this setup. Based on the previous statement about force dominated frequency regions, this setup is not suitable for fluids with a zero shear viscosity lower than 100 Pas. For lower viscosities, the damper design should be changed to obtain accurate fluid models. The RMD's geometrical damping factor can be changed to increase the influence of the damping forces with respect to the stiffness and mass forces. A more rigorous change is the design with a lower stiffness and moving mass to maintain the same natural frequency and decrease the stiffness and mass forces, which increases the sensitivity with respect to the damping behavior. In order to create LVE models over a different frequency range, setups with different natural frequencies can be designed to increase the sensitivity of the measurement and, therefore, the resulting LVE model quality in a specific frequency range.

# Damping Optimization of a Complex Motion Stage and Experimental Modal Analysis

**Abstract** - This chapter presents robust mass damper design for a complex motion stage design made of ceramics. The modes that have to be damped are determined in the frequency range between 1 and 4 kHz. The damper placement is elaborated upon and, subsequently, optimization algorithms are applied in order to calculate the maximum open-loop suppression factor of resonances over a specified frequency range. Damper hardware is designed based on the optimization results and the approach is proven by experimental validation. As a result, the equivalent modal damping of the resonances visible in the frequency response function is increased by at least 16 times between 1 and 4 kHz and, in addition, by 10 times up to 6 kHz. The time response with robust mass dampers shows an amplitude decrease rate which is 20 times faster with respect to the stage without dampers. The ability to crate broad banded damping by RMDs in case of realistic motion stage designs is explicitly proven in this chapter.

## 5.1 Introduction

### 5.1.1 The control problem of lightly damped systems

Motion systems are applied in many industries. One of these industries is the production of integrated circuits (IC's). The main step in IC production is the illumination of the IC pattern on the substrate's surface which is called a wafer [88]. For this purpose, the wafer is positioned on a motion stage which is positioned under an optical column. The illumination step is currently limiting the production of IC's for two reasons: 1) the minimum feature size is, among other things, limited by the positioning accuracy of the stage with respect to the optical column and 2) the throughput is limited by the maximum acceleration, velocity and settling times [43]. These properties are largely determined by the motion control system [18,58] and, therefore, much research is executed in the field of motion control. Different control strategies are applied to deal with specific problems. A control system normally consists of a feedback loop and a feedforward path. The function of the feedback loop is [30] suppression of disturbances and the creation of robustness against parameter changes. The function of feedforward is application of acceleration forces using a setpoint trajectory by using an inverse plant model [54].

Various control strategies are developed to increase the performance further:  $H_\infty$ -controller design for performance increase [83,102], and iterative learning control to track specific references and reject repeating disturbances [24,89].

A feedforward controller performs well only to the extent that the system's dynamical behavior is accurately known. Friction, nonlinear behavior, and disturbances can limit the effectiveness of feedforward control. A feedback controller counteracts the outgrowth of unmodeled system behavior and random disturbances acting on the motion stage. The suppression of disturbances is proportional to the controller gain, which is expressed with the term high-gain feedback.

The performance – maximum controller gain – of a control system is largely determined by the plant behavior [65]. The stage moves as a rigid body at low frequencies, in contradiction to higher frequencies at which multiple flexible eigen modes show their resonance frequency. The bandwidth limit is a function of: 1) the frequencies of these modes, 2) the actuator and sensor locations which determine which modes appear in the measurement and how they present themselves, and 3) the modal damping of the resonances. The displacements of the eigen modes appear as vibrations which persist in the stage as function of the damping value. High-precision motion stages typically contain low modal damping values. This results in large amplification factors at the resonance frequencies and therefore transient responses that hardly damp out.

Many methods are presented in literature to increase the modal damping. Different damping models for mechanical systems, with attention to viscously and non-viscously damped multiple degree-of-freedom (DoF) linear vibrating systems, is presented in [3,33]. One solution is to use materials with a high structural damping value [13,77]. Ceramics are often used in motion stage design because of their high specific stiffness and possibilities to create low thermal expansion coefficients [4,80]. However, these materials usually lack damping

[8,20]. Various approaches are available to increase the modal damping of structures. Constrained layers can be designed for vibration and sound control for specific frequency regions, in both passive and active variants [41,106]. Squeeze film dampers can result in very high damping values [35]. The Tuned Mass Damper (TMD) is a solution to suppress the amplification factor of a resonance frequency [25]. These devices range from a few grams to devices with a few hundred tons of moving mass for tall buildings and towers [51]. Especially in structural engineering such devices have proven to be very useful and have been developed for decades [11,52], with extensions to semi-active [2] and active devices [21] as well as multi DoF versions [6,111]. Multiple TMD's can be added to obtain a more broad-banded damping behavior [1].

To improve the modal damping over a broad frequency range, Robust Mass Dampers (RMDs) are proposed in Chapter 2. It was shown that the bandwidth of the motion system can be increased by adding dampers to a motion stage. For good results with a minimum number of dampers added, the dampers have to have a broad banded damping effect, which is created by relatively high modal damping values. This is the main difference with tuned mass dampers, which contain relatively low modal damping values (10-25%). Robust mass dampers typically show modal damping values larger than 0.5. In Chapter 2, broad banded damping was shown for a square plate stage model together with corresponding bandwidth improvements.

### **5.1.2 Contributions and approach**

This chapter presents the results of a robust mass damper implementation on a complex motion stage with realistic natural frequencies to increase the modal damping of the out-of-plane modes. Existing motion stage hardware is used as a starting point. RMD's are designed based on a shear loaded high-viscosity viscoelastic fluid to obtain a linear time-invariant damper. A design approach is presented which results in parameter values for the dampers to improve the modal damping over a specified frequency range. The RMD's are realized and characterized to validate their behavior. Experimental modal analyses are performed at stage level with and without RMD's added. The theoretical advantages of the implementation of RMD's are proven in practice, in particular for motion stages, and limitations and further challenges are observed and discussed.

The main question to be answered is how to determine the damper parameters for a complex motion stage with realistic dampers included. For this purpose, a complex motion stage with its dynamic model is presented in Section 5.2 and the damper structure is introduced. Section 5.3 shows the approach to determine the damper parameter values to obtain optimal modal damping over a specified frequency range. Damper parameters are presented and the damper design is elaborated in Section 5.4. In addition, it shows the characterization of the dampers after production. Section 5.5 presents the experimental validation of the stage with dampers added. Frequency domain results are given as well as time domain results. Section 5.6 concludes the chapter by summarizing the results and Section 5.7 discusses about the interpretation of the results.

## 5.2 Stage and damper dynamic models

To apply the approach to increase the modal damping of motion stages in full complexity, hardware is necessary as starting point. In this chapter, existing hardware is investigated to show that the approach is not design specific. This section describes the hardware and the problems that have to be solved.

### 5.2.1 Motion stage hardware

Figure 5.1 shows a photograph of an experimental motion stage design. This is a monolithic ceramic structure with a complex geometry. The design from top view is squared and the ratio between edge length and stage height is roughly 4.8:1. The top plate is supported by ribs to stiffen the structure. To increase realism, pockets are designed in the top plate in which measurement devices can be mounted. In addition, the corners show protrusions to accommodate for additional sensors. These features add a substantial amount of complexity to the stage design, which is beneficial for considering this design a complex stage model to validate the theory. An unassembled stage is analyzed in this approach. A computer aided design (CAD) model of this stage has been made and is presented in Figure 5.2.

A finite element model is created and an undamped modal analysis is performed. Properties of the model, the material and the software are listed in Table 5.1. The lack of material damping, the absence of part interconnections and the monolithic design justify an undamped modal analysis to calculate the stage's natural frequencies and corresponding mode shapes. The stage FEM model is unsuspended, which means the free natural frequencies are calculated. The material properties as listed above are used and the natural frequencies of the model are -



Figure 5.1: A photograph of the experimental stage design made of ceramics. This stage is used in order to prove the possibility of broad-banded resonance damping.

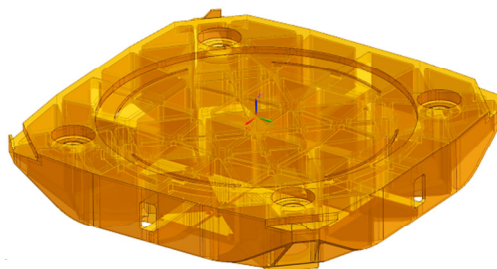


Figure 5.2: A CAD model of the motion stage, created by 3D-modelling software.

calculated up to 6 kHz. Subsequently, the natural frequencies and the nodal displacements corresponding to the mode shapes are exported and saved.

Figure 5.3 presents the first six flexible modes of the stage. Note that although this design is

Table 5.1: Material and model properties of the stage and the corresponding FEM model.

| Material properties        | Value              | Unit              |
|----------------------------|--------------------|-------------------|
| Material name              | Ceramic            | -                 |
| Specific density           | 2550               | kg/m <sup>3</sup> |
| Young's modulus            | 1,44e+11           | Pa                |
| Poisson's ratio            | 0,32               | -                 |
| <b>Software properties</b> |                    |                   |
| Software                   | NX 7.5.1 / Nastran |                   |
| Solver                     | 103 Modal Analysis |                   |
| <b>Model properties</b>    |                    |                   |
| Dimensions                 | 600 x 600 x 125    | mm <sup>3</sup>   |
| Volume                     | 8.98e6             | mm <sup>3</sup>   |
| Mass                       | 22,9               | kg                |
| Number of elements         | 804581             | -                 |
| Number of nodes            | 228294             | -                 |

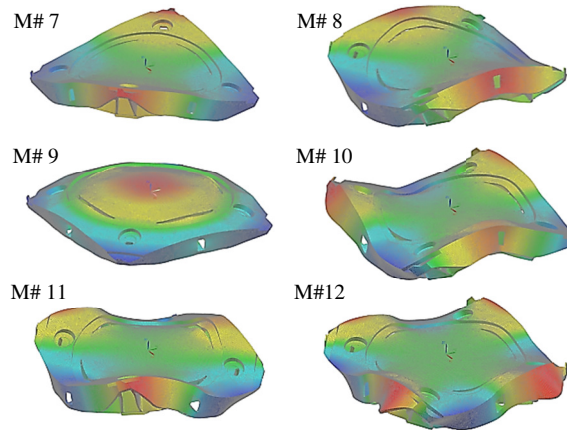


Figure 5.3: The first six flexible modes of the motion stage calculated with FEM.

Table 5.2: Natural frequencies of the first six flexible modes of the motion stage.

| Mode # | Mode name       | Frequency |
|--------|-----------------|-----------|
| M# 7   | Torsion Mode    | 1532 Hz   |
| M# 8   | Saddle Mode     | 1919 Hz   |
| M# 9   | Umbrella Mode   | 2552 Hz   |
| M# 10  | HO bending mode | 2760 Hz   |
| M# 11  | HO bending mode | 2760 Hz   |
| M# 12  | HO saddle mode  | 3538 Hz   |



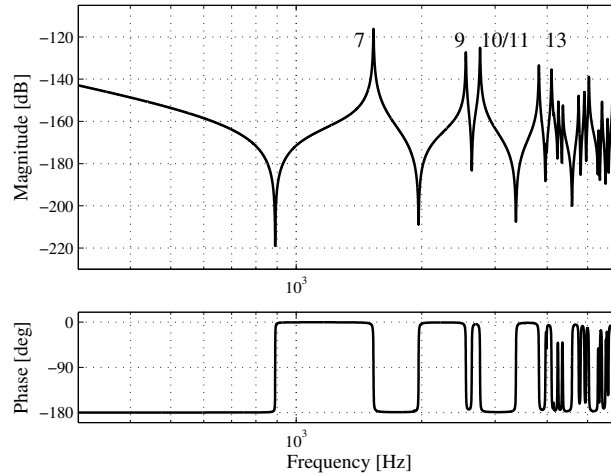


Figure 5.4: Collocated frequency response function at the stage corner in z-direction.

much more complex than a square plate (due to the complex geometrical design and the 4.8:1 length-height ratio), the first six modes show comparable mode shapes. The corresponding natural frequencies are listed in Table 5.2. The first six modes are rigid body modes that do not show internal deformation, which explains the mode numbering from 7 to 12 in Figure 5.3.

A motion stage with a configuration as presented in Figure 5.1, usually contains four sensors in z-direction which are mounted to the stage's corners to measure the vertical stage position. Therefore, the mode shapes that show amplitudes in z-direction at these corners are often limiting the bandwidth of the closed loop in z-direction. Figure 5.4 shows a collocated frequency response function of the stage's corner and therefore shows the resonances that are visible at the sensors. These modes are included in the observability of the control system.

Because the robust damper design is intended to improve the bandwidth of the control system, the dampers should be able to suppress the bandwidth limiting resonances maximally. Figure 5.4 shows an undamped, collocated frequency response function of the stage corner to visualize the resonances appearing at the corners. The first resonance at 1532 Hz belongs to the torsion mode and the second visible resonance at 2552 Hz belongs to the umbrella mode. Note that the saddle mode at 1919 Hz (mode 8) is not visible in this frequency response function because of the fact that this mode does not show displacements in z-direction at the corners, it is unobservable. See Figure 5.3 and Table 5.2 for the first six NRB mode shapes and corresponding natural frequencies. The goal of this approach, motivated by the position of the sensors on the corners, is to increase the modal damping of the modes that show displacements in z-direction at the stage's corners. The modes that have to be damped are, respectively, nrs: 7, 9, 10, 11, and 13.

### 5.2.2 Damper placement

The transfer function  $T_i(s)$  is defined as the contribution of a single mode  $i$  in an input/output transfer function and is presented in (5.1). It shows that the visibility of a certain mode in a transfer function depends on the modal factors of the actuator  $\Phi_i^{act}$  and the sensor  $\Phi_i^{sen}$ :

$$T_i(s) = \frac{\Phi_i^{act} \cdot \Phi_i^{sen}}{s^2 + 2\zeta\omega_i s + \omega_i^2} = \frac{1}{m_i s^2 + d_i s + c_i} \quad (5.1)$$

From this equation, by rearranging the second and third part, the result appears that the modal mass of a mode in a certain transfer function equals:

$$m_i = \frac{1}{\Phi_i^{act} \cdot \Phi_i^{sen}} \quad (5.2)$$

This equation shows that a certain mode's modal mass depends on the locations of the actuator and sensor. Since a robust mass damper can be seen as a local control loop, the actuator and sensor location are equal. This results in the following equation for the apparent modal mass for mode  $i$  at the RMD location:

$$m_i = \frac{1}{(\Phi_i^{RMD})^2} \quad (5.3)$$

It is known from literature that the efficiency of an RMD depends on the mass ratio of the RMD and the mode that has to be damped. From this and (5.3) it follows that the efficiency of an RMD to damp a certain resonance depends on the position of the damper on the stage in a quadratic sense. Figure 5.5 shows top views of the stage for mode 7 until 10 with the largest displacements indicated by the filled areas. The displacement based approach as shown,

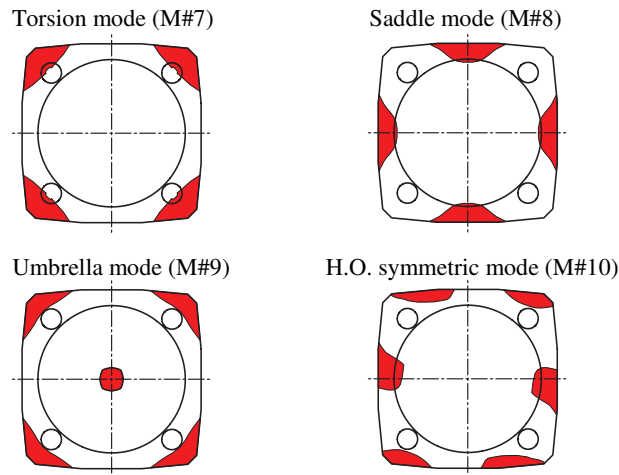


Figure 5.5: Top view of the stage of the four lowest NRB modes. The areas with the largest displacements in z-direction indicated for mode number 7, 8, 9, and 10.

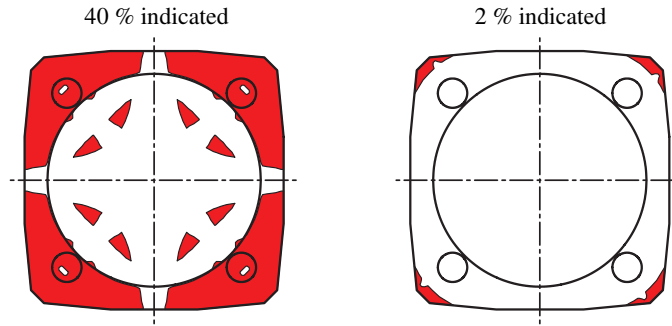


Figure 5.6: Top view of the stage with the largest displacements of the first four limiting modes indicated. The left figure shows a plot in which 40 % of the largest displacements is indicated. The combined shape of the contributing modes is visible in this plot. The right figure shows a view in which the largest 2 % of the displacement area is indicated. This refinement shows that the corners are the best mounting locations for RMDs for this specific motion stage.

however, shows that a stage location with large amplitudes can significantly decrease the damper mass needed to obtain a certain amount of suppression.

For this application, broad banded resonance suppression is intended, which implies that more than one resonance has to be suppressed. The argumentation of the position based apparent modal mass still holds, however, in this case an RMD location should be found that minimizes the modal mass of all modes that have to be damped. This implies that a stage location has to be found at which these modes all show displacements. Figure 5.6 shows the result of a search for large displacements in  $z$ -direction for mode numbers 7, 9, and a combination of mode 10 and 11, because mode 10 and 11 are symmetric modes with the same natural frequency. The left plot shows 40 percent of the largest displacements in  $z$ -direction which indicates that the center lines and the stage center should not be used to mount the dampers to. The right figure shows the 2 percent largest displacements and this figure clearly shows that the dampers should be mounted to the corners. Based on this analysis four dampers should be mounted in  $z$ -direction: one damper at each corner.

### 5.2.3 Dynamic models

A dynamic model is created in state space modal-1 form and implemented in Matlab. The corresponding mathematical expressions of the system triples component matrices of the  $i^{th}$  mode are presented in (5.4), (5.5), and (5.6).

$$A_{mi} = \begin{bmatrix} 0 & \omega_i \\ -\omega_i & -2\zeta_i\omega_i \end{bmatrix} \quad (5.4)$$

$$B_{mi} = \begin{bmatrix} 0 \\ b_{mi} \end{bmatrix} \quad (5.5)$$

$$C_{mi} = [c_{mqi}/\omega_i \quad c_{mvi}] \quad (5.6)$$

The separate modes form the state equations (5.7) and (5.8) and the summation results in the system behavior (5.9).

$$\dot{x}_i = A_{mi}x_i + B_{mi}u \quad (5.7)$$

$$y_i = C_{mi}x_i \quad (5.8)$$

$$y = \sum_{i=1}^n y_i \quad (5.9)$$

in which  $y$  describes the response of the overall system. The modal-1 model can handle large differences between natural frequencies, however, it does not allow to add pure rigid body modes ( $\omega = 0$ ). Therefore, these modes are implemented as low-frequency suspension modes. Finally, the modal damping of the stage has to be estimated and implemented in the model. For that purpose, the first five resonances of a frequency response function are fitted on a existing measurement data. These frequency response functions are shown in Figure 5.7. The modal damping value obtained with the fit equals  $8.8\text{e-}4$ . To avoid overestimation of the performance of the dampers in terms of amplitude reduction, the implemented modal damping in the dynamic model amounts  $1\text{e-}3$ , which is an overestimation of 13.6 % with respect to the fitted value and therefore underestimates the resonance amplification by 1.11 dB.

Now we will add an RMD model to the lightly damped stage model to increase the modal damping of a number of modes. The robust mass damper with an LVE fluid inserted is presented in Chapter 4. The dynamic model of the damper is shown in Figure 5.8.

The damper configuration consists of an inertial mass  $m$ , a translational flexible guide

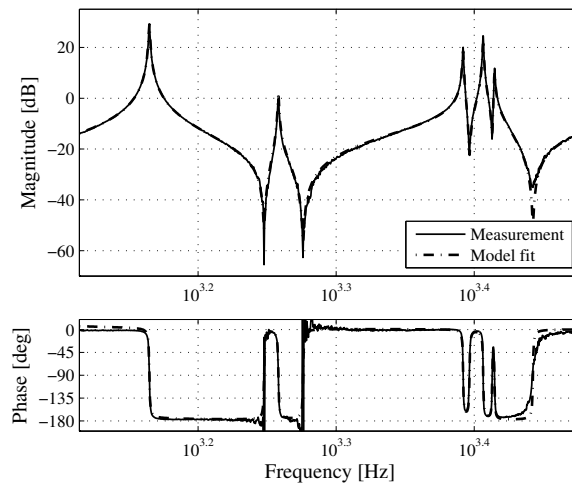


Figure 5.7: Bode diagram of a measured FRF and a fitted FRF to estimate the stages' modal damping. This fit is created with a modal damping factor of  $8.8\text{e-}4$ .

designed as a double leaf spring mechanism with total stiffness  $c$  and a part that creates the damping force with damping constant  $d$ . A complete system, containing all parts is called RMD. The dashpot is intended to create a velocity dependent force. This combination of components results in a linear time-invariant system behavior. The velocity dependent damper force is the result of two parameters:

- the fluid's mechanical properties,
- the damper geometry.

The behavior of the fluid used is measured and a Linear Visco-Elastic (LVE) 3-mode multi-Maxwell model is fitted on the measurement data. The fluid model is presented in Figure 5.9. This figure shows the viscous and elastic properties of the fluid as function of the frequency. A complete elaboration of the fluid model is provided in Chapter 4. The damper principle is chosen to be a parallel plate damper based on the shear principle with the viscous fluid in between the two parallel plates. In case of a velocity difference between these plates, a velocity gradient is created in the fluid causing a specific force per unit of area, which, multiplied by the effective area submerged in the fluid, leads to a damping force. This leads to the fact that the damping can be expressed with a geometrical damping factor (GDF) in m, which is defined as:

$$GDF = \frac{A}{h} = \frac{2nlw}{h} \quad (5.10)$$

In this equation,  $A$  is the total area of the damper fins,  $n$  is the number of fins,  $l$  is the fin length and  $w$  is the fin width. Finally,  $h$  is the effective gap width in which the fluid is

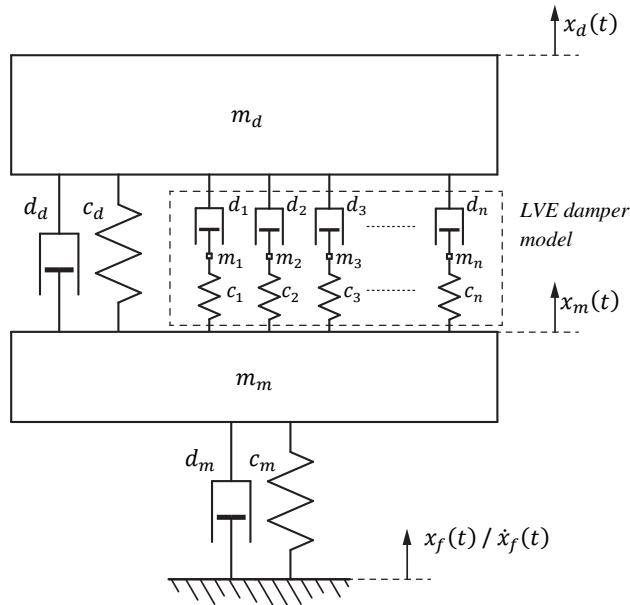


Figure 5.8: Damper model with multi-mode Maxwell fluid model included.

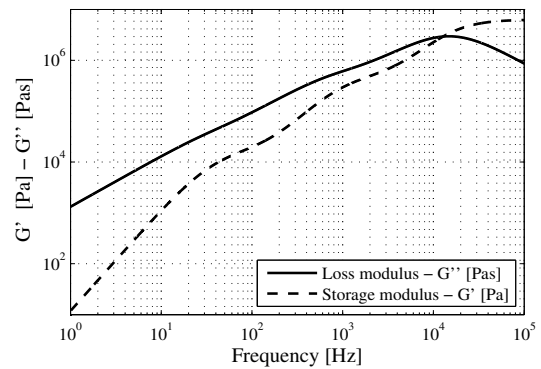


Figure 5.9: Storage and loss modulus of the 3 Maxwell mode LVE fluid model.

applied. This GDF, combined with the fluid properties in Pas and Pa, lead to a spring stiffness in N/m and a damping constant in Ns/m. This visco-elastic behavior leads to an extension of the RMD model and is shown by the extension with Maxwell models as indicated by the serially mounted springs and dashpots, visualized in the dashed box in Figure 5.8. Mass  $m_m$  represents the base part of the damper that contains the slot of the damping mechanism and provides the damper mounting to the motion stage. This coupling is modelled as an additional spring  $c_m$  and dashpot  $d_m$ . This mass is determined to be  $0.7 \cdot m_d$ . See Chapter 4 for a detailed explanation of the damper principle and the corresponding dynamic model. The question to be answered is: what should the damper parameters be for optimal suppression.

### 5.3 RMD parameter calculation

This section describes the approach to determine optimal parameter values of the robust mass dampers for resonance suppression. These damper parameter values are used in the hardware design phase. The RMD placement has been discussed in Section 5.2.2, therefore, the approach is described to determine the resonances of which the damping should be increased and an optimization technique is described to find the optimal parameter values.

#### 5.3.1 Damper parameters

Because of the specific locations of the dampers on the stage, the resulting model is non-proportionally damped, which means that the nodal damping matrix cannot be assembled from a linear combination of the nodal mass and stiffness matrices. This implies that the stage deformations no longer can be calculated by linear superposition of the undamped mode shapes. The real natural modes as shown in Figure 5.3 have changed to complex mode shapes and the system's response becomes complex. A few problems arise while calculating the modal damping by calculating the system's poles: firstly, not all modes are equally damped. This was already observed in Section 5.2 in which the damper locations are determined. An example of an 'undampable mode' with, therefore, a fixed pole pair are the poles corresponding to the saddle mode. Secondly, the non-proportional damping leads to resonance frequencies that interchange as function of the damper parameters. To deal with these properties, a modal damping criterion is applied based on observability of the limiting modes.

To find the optimal solution in terms of resonance suppression, the following properties have to be determined:

- the RMD locations,
- the number of RMDs,
- the moving mass ( $m_d$ ),
- the natural frequency ( $\omega_{RMD}$ ),
- the geometrical damping factor ( $GDF_{RMD}$ ).

The first and second point are related and are discussed in Section 5.2. Damper parameters have to be found to maximize the damping for a number of resonances. For this purpose, an optimization procedure is used. There are mainly three reasons for the application of such an algorithm:

- the complex stage dynamics: multiple modes are included in the model,
- the LVE fluid behavior of the damper,
- the broad banded suppression region.

The RMD's mass, stiffness and GDF are parameters that have to be determined to obtain optimal suppression values of the resonances. In general, larger suppression factors can be obtained with larger RMD masses. Therefore, if the RMD mass is included in the optimization procedure, it will result in a parameter value which equals its upper bound. Therefore, the damper mass is chosen to be fixed in this optimization. This enables to choose a damper mass, based on a modal mass approach and/or an overall mass limit. Subsequently, the natural frequency and the geometrical damping factor are optimized for the chosen damper mass. In this chapter, this approach is elaborated for a specific case, and afterwards the relation of the resonance suppression factor with the damper mass is shown.

In this case, the damper mass is determined based on both approaches: the frequency response function as shown in Figure 5.4 has a first resonance with a modal mass of 3.5 kg: this is calculated using the displacement results of the undamped FEM modal analysis and (5.5). The total stage mass is 22.9 kg, see Table 5.1. The total damper mass consists of  $m_m$  and  $m_d$ , see Figure 8:  $m_m$  is determined to be  $0.7 \cdot m_d$ . The damper active mass  $m_d$  is chosen at 65 g per damper: this means a total damper mass ( $m_d + m_m$ ) of 110.5 g. The mass percentage with respect to the first flexible mode amounts 7.5 % and an overall mass contribution of < 2 % with respect to the stage mass is realized with four dampers added.

### 5.3.2 Optimization formulation

The RMD's natural frequency  $\omega_{RMD}$  and geometrical damping factor  $GDF_{RMD}$  have to be determined for this specific problem. The cost function is defined as:

$$\min_x J(x) \tag{5.11}$$

subject to,

$$lb \leq x \leq ub \tag{5.12}$$

in which parameter vector  $x$  contains the undamped natural frequency of the RMD in Hz and the geometrical damping factor (5.10) in m:

$$x = \begin{bmatrix} \omega_{RMD} \\ GDF_{RMD} \end{bmatrix} \quad (5.13)$$

The suppression of the resonances in the Bode diagram is used as cost function  $J(x)$ . This cost function is visualized in Figure 5.10. The parameters that have to be set are the frequencies  $f_1$  and  $f_2$ , which determine the frequency range in which the cost function is evaluated. In between these frequencies, the resonances are determined and connecting lines are drawn between the resonance peaks. From  $f_1$  to the first resonance and from the last resonance to  $f_2$ , horizontal lines are drawn. This discontinuous curve is called  $M_u$ . Curve  $M_d(x)$  has the same shape and touches the damped FRF, and therefore, is a function of parameter vector  $x$ . The cost function is defined as the distance between lines  $M_u$  and  $M_d(x)$ . This criterion forces a maximal suppression in dB of the visible resonances in the specified frequency region. Equation 5.14 shows the cost function, expressed as the maximal difference between  $M_d(x)$  and  $M_u$ .

$$J(x) = -\min(M_u - M_d(x)) \quad (5.14)$$

Note that this cost function has a discontinuous character, due to the  $\min$  function. For the parameter upper and lower bounds, ample values have been implemented to find an optimal solution without being restricted by these bounds.

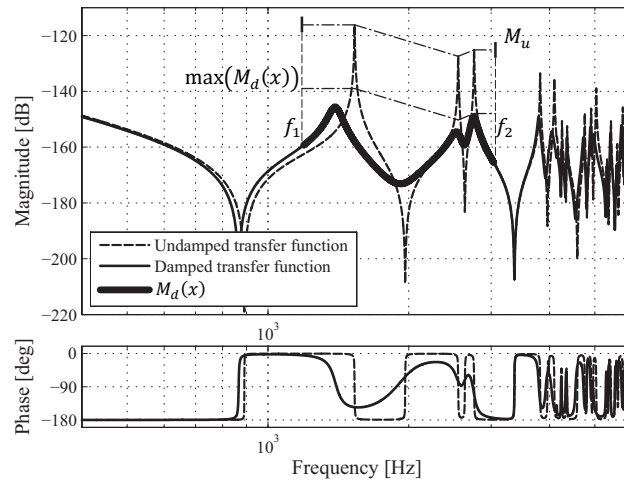


Figure 5.10: Graphical representation of the cost function. The resonances in the frequency range between  $f_1 < f < f_2$  are determined and a connecting line is drawn between the resonances. The left and right parts are described by horizontal line elements.



$$\begin{bmatrix} 250 \\ 0.01 \end{bmatrix} \leq \begin{bmatrix} \omega_{RMD} \\ GDF_{RMD} \end{bmatrix} \leq \begin{bmatrix} 5000 \\ 100 \end{bmatrix} \quad (5.15)$$

The upper and lower values for the parameters can be determined by the manufacturability of the damper parts. Constraints, both linear and non-linear, are not included in this optimization criterion. To find an optimal solution within the parameter space, a hybrid optimization algorithm is applied which firstly executes a genetic algorithm. The solution of this optimization, which is assumed to be close to the global minimum, is used as initial guess for a gradient based optimization procedure.

The following sections show two optimization cases:

- a small banded optimization which includes a single resonance,
- a broad banded optimization which includes a range of resonances.

The small banded example is provided to create a connection with the solutions that are known from literature which are typically small banded and to enable a comparison with the results of the broad banded optimization.

### 5.3.3 Small banded optimization

The algorithm is used to calculate the optimal parameters to suppress a single resonance frequency. The result is shown in Figure 5.11 and shows Tuned Mass Damper (TMD) behavior.

For this single frequency resonance damping, as widely described in literature, stiffness and damping values can be calculated by hand [25]. The symmetry of the stage design, combined with symmetrical damper locations, simplifies these calculations. Therefore, the results of both the optimization and of the calculations by hand are presented in Table 5.3 for

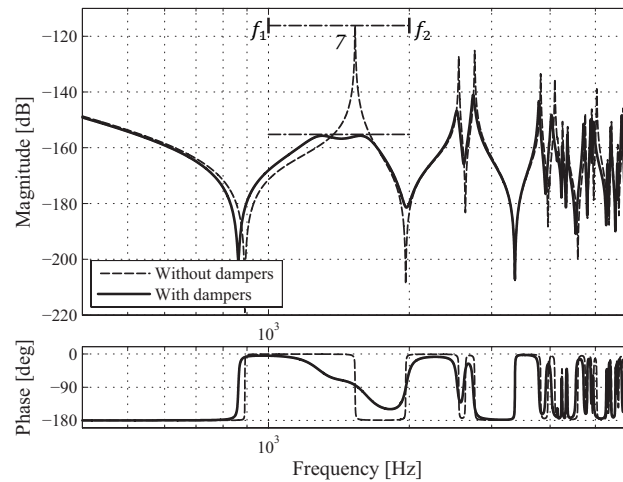


Figure 5.11: Result of the optimization procedure with the LVE fluid model included. The cost function is specified between 1000 and 2000 Hz. This implies that the first mode is suppressed by the dampers.

comparison reasons. Note that mass  $m_m$  belongs to the damper, but is connected rigidly to the stage and therefore, should be added to the stage's apparent modal mass. Table 5.3 shows the results for the optimization procedure with (1) the LVE fluid model, (2) calculations by hand, and (3) an optimization result for a purely viscous fluid. The last is added to explain differences between the results of cases 1 and 2. In the viscous fluid optimization case, a fluid model is used that contains only viscous behavior for the specified frequency range, elasticity is absent. These results do match the calculations made by hand by 0.1 dB, see Table 5.3, cases 2 and 3. This difference is due to the theory as described in [25], which only contains equations for a system with a single resonance, on which a damper is added. This frequency response function is a sum of over 45 modes. The LVE fluid optimization, however, shows different parameters for the dampers, and a slightly larger suppression is obtained. The LVE fluid optimization shows the following behavior with respect to the solutions with the pure viscous fluid:

- the suppression factor is 0.2 dB larger,
- the natural frequency is 8.8 % lower,
- the damper area is 2.76 times larger.

Table 5.3: Optimization results for single resonance suppression. The cost function is defined between 1000 and 2000 Hz. The results marked with a (\*) are calculated after optimization, using the zero shear viscosity.

| Stage properties               | Value | Unit |
|--------------------------------|-------|------|
| First natural frequency        | 1532  | Hz   |
| Eff. modal mass first mode     | 3,48  | kg   |
| Damper properties              |       |      |
| Mass $m_d$                     | 65    | g    |
| Mass $m_m$                     | 45,5  | g    |
| Coupling frequency             | 10e3  | Hz   |
| (1) LVE fluid optimization     |       |      |
| Natural frequency              | 1271  | Hz   |
| Geometrical damping factor     | 2,1   | m    |
| * Modal damping - ZSV based    | 0,445 | -    |
| Amplitude reduction            | -39,6 | dB   |
| (2) Calculations by hand       |       |      |
| Natural frequency              | 1394  | Hz   |
| Modal damping                  | 0,147 | -    |
| * Geometrical damping factor   | 0,76  | m    |
| Amplitude reduction            | -39,3 | dB   |
| (3) Viscous fluid optimization |       |      |
| Natural frequency              | 1390  | Hz   |
| Geometrical damping factor     | 0,81  | m    |
| * Modal damping                | 0,157 | -    |
| Amplitude reduction            | -39,4 | dB   |

The last two can be explained by the LVE fluid behavior: at 1500 Hz the fluid's phase has decreased to 65 deg, which reduces the efficiency as a damping medium. This phenomenon is compensated by the larger GDF. Due to the fact that the fluid is already partially elastic around 1500 Hz, an additional stiffness is introduced. This is compensated by the lower natural frequency. The larger suppression of 0.2 dB with respect to the viscous fluid is elaborated upon in Appendix C. This solution, with  $\zeta < 0.5$ , is typical for a tuned mass damper, which has to suppress one specific resonance and, therefore, contains a relatively low modal damping value.

#### 5.3.4 Broad banded optimization

To obtain broad banded damping, the cost function is redefined between 1 and 4 kHz. Figure 5.12 presents the resulting Bode diagram. This frequency range captures resonances 7, 9, 10/11 and 13, as used in Section 5.2.2, in which the damper locations are determined. It shows a suppression of -23.6 dB. The resulting parameters are listed in Table 5.4. Figure 5.12 shows that the suppression is limited by resonances 7 and 13, which both touch the cost function. Figure 5.13 shows the pole loci as function of  $GDF_{RMD}$  with the optimized values indicated. The mode numbers are added and the upper and lower frequencies of the cost function are indicated by  $f_1$  and  $f_2$ . Lines *a* and *b* show the modal damping lines of the original stage model (1e-3) and the damped stage respectively. Note that line *b* intersects with the crosses of modes 7 and 13. Mode 9 and mode 10/11 show larger damping values.

This observation corresponds with the result in Figure 5.12. Table 5.4 shows the typical behavior of a robust mass damper (RMD), which is characterized by a relatively high modal

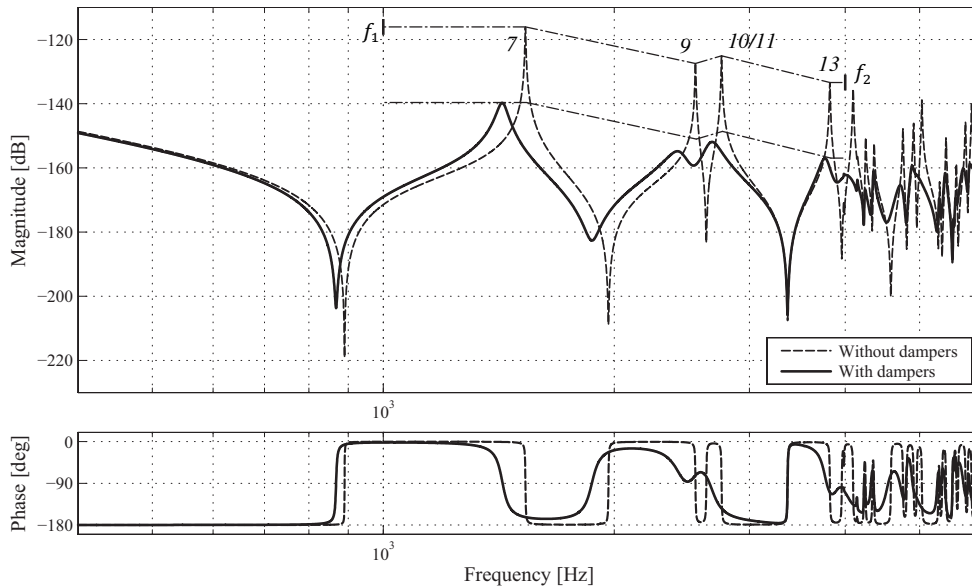


Figure 5.12: Result of the optimization procedure with the LVE fluid model included and the cost function specified between 1000 and 4000 Hz, containing resonances 7, 9, 10/11, and 13. The result is a range of resonances that are suppressed by the dampers.

Table 5.4: Results of the broad banded optimization for the LVE fluid and a pure viscous fluid. The result marked with a (\*) is calculated after optimization, using the zero shear viscosity.

| <b>LVE fluid optimization</b>     | <b>Value</b> | <b>Unit</b> |
|-----------------------------------|--------------|-------------|
| Natural frequency                 | 1270         | Hz          |
| Geometrical damping factor        | 14,33        | m           |
| * Modal damping - ZSV based       | 3,04         | -           |
| Amplitude reduction               | -23,6        | dB          |
| <b>Viscous fluid optimization</b> |              |             |
| Natural frequency                 | 2137         | Hz          |
| Geometrical damping factor        | 4,83         | m           |
| * Modal damping - ZSV based       | 0,61         | -           |
| Amplitude reduction               | -22,7        | dB          |

damping value: over 50 % modal damping ( $\zeta > 0.5$ ). The natural frequency and the ZSV estimated modal damping value amount 1270 Hz and 3.04, respectively. For comparison, an optimization result is included with the purely viscous fluid model, as used in Section 3.2.3. This fluid model contains only damping and, therefore, stiffness and damping are strictly separated. The results are a natural frequency of 2137 Hz in combination with a modal damping of 0.61. The geometrical damping factor of 14.33 m for the LVE optimization with respect to 4.83 m for the purely viscous fluid, shows the compensation for the elasticity of the fluid.

The natural frequencies of 1270 and 2137 Hz show that the mechanical stiffness compensates for the added fluid stiffness. In this broad banded optimization case, a 6.8 times larger geometrical damping factor has been calculated compared to the single resonance suppression, and therefore, a relatively high stiffness is introduced by the LVE fluid. This is compensated by the spring stiffness, which results in approximately equal natural frequencies for both cases. The results as presented above show that the optimization algorithm is very useful: the solution strongly depends on the LVE fluid properties. The algorithm calculates the best combination of parameter values for optimal suppression.

### 5.3.5 Mass dependence and robustness

Results of separate optimizations for increasing damper mass, in a range from 10 to 250 g per damper are shown in three graphs in Figure 5.14. The upper graph shows the suppression in dB, which increases as function of damper mass. This figure shows a positive relationship between suppression factor and damper mass over this mass range. The suppression amounts 12 dB per decade of damper mass, which means that the amplitude reduces by a factor 4 as mass increases by a factor 10. This shows the tradeoff between the suppression factor and the damper mass.

The robustness of both the small banded solution and the broad banded solution are calculated by varying both the geometrical damping factor and the natural frequency by 10 % and calculating the resulting suppression. Table 5.5 lists the resulting performance decreases for

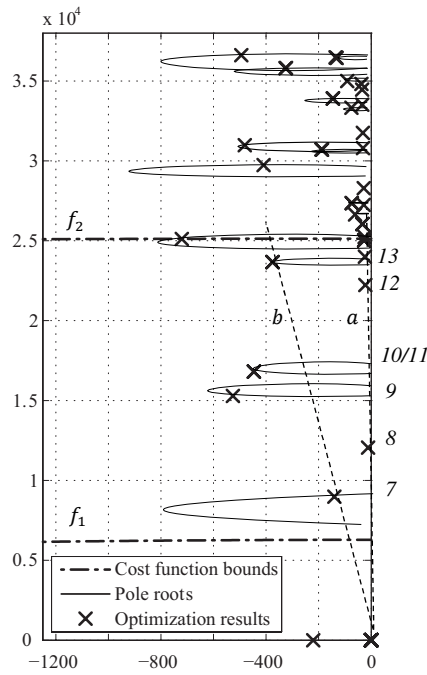


Figure 5.13: Root loci with the optimization result indicated by the crosses. The numbers represent the flexible modes. Line *a* represents the angle of initial stage damping and line *b* shows the minimal achieved damping increase.

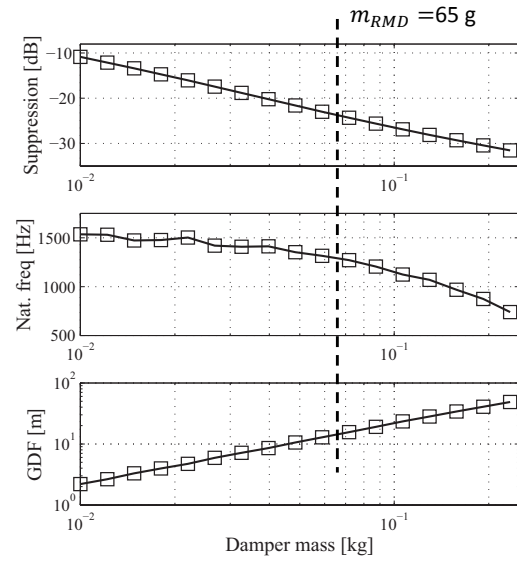


Figure 5.14: Optimal damper parameters for suppression between 1000 and 4000 Hz, as function of the damper mass. The upper graph shows the suppression factor in dB, the second graph shows the natural frequency of the damper in Hz and the lower graph shows the geometrical damping factor in m. The solution of 65 g is indicated by the vertical dashed line.

both the small banded solution and the broad banded solution. It shows that the robustness for parameter variations is 3.07 times better for the latter. This is an advantage from different points of view. Although not elaborated upon in this chapter, it will be advantageous in case of controlling the stage by position controllers. In addition, it is an important finding with respect to the production tolerances: the behavior of the broad banded damper is less sensitive with respect to variations in stiffness and damper geometry than the small banded one.

Table 5.5: The results of the robustness analysis of the cases presented in Sections 5.3.3 and 5.3.4.

| Robustness analysis           | Value    | Unit |
|-------------------------------|----------|------|
| Variation of $\omega_{RMD}$   | $\pm 10$ | %    |
| Variation of $GDF_{RMD}$      | $\pm 10$ | %    |
| <b>Small banded (1-2 kHz)</b> |          |      |
| Performance decrease          | 4,53     | dB   |
|                               | 40,65    | %    |
| <b>Broad banded (1-4 kHz)</b> |          |      |
| Performance decrease          | 1,23     | dB   |
|                               | 13,24    | %    |

## 5.4 Damper design & validation

A damper mechanism is designed which contains the following properties:

- a moving mass  $m_d$  of 65 g,
- a mounting mass  $m_m$  of 45.5 g,
- a natural frequency  $\omega_{RMD}$  of 1270 Hz (z-translation direction),
- other natural frequencies as high as possible,
- a geometrical damping factor  $GDF$  of 14.33 m,
- an encapsulation to contain the fluid.

Figure 5.15 shows an exploded view of the RMD design. The mechanism part is monolithically designed and consists of 1) a mounting side, 2) leaf spring pair, and 3) the damper side. The leaf springs enable a translation of the damping side with respect to the mounting side. The design of the leaf springs determines the stiffness between those two sides and therefore the natural frequency. The mounting part is connected to the stage interface by the RMD mounting bolts. A stage interface is glued to each stage corner. The slot part is assembled to the mounting side and the fin part is mounted to the damper side. These two parts contain fins with the fluid in between. A translation of the fin part with respect to the slot part, which implies a velocity difference, induces a shear rate in the fluid and therefore a velocity dependent force. The fluid is surrounded by a flexible encapsulation, which prevents it from running out. The RMD design is modelled with 3D modelling software which enables to calculate the part volumes and, combined with the material properties, the part masses.

### 5.4.1 Mechanism design

Figure 5.17 shows the results of a modal analysis of the RMD mounted to the stage. The damper is modelled as well as an interface part and a stage corner. An assembly is created and an undamped modal analysis is performed. The first natural frequency is the vertical translation of 1270 Hz. The leaf springs and their connection to the bulk material are critical

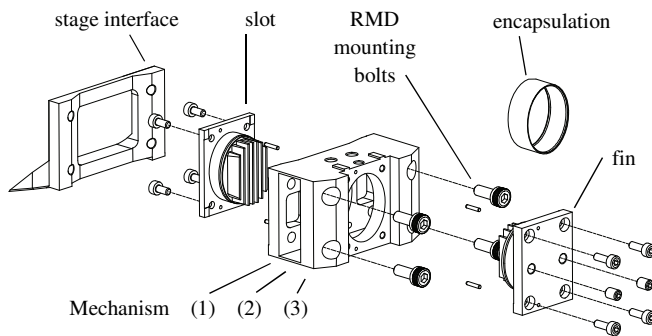


Figure 5.15: Exploded view of the RMD design with the different parts indicated.

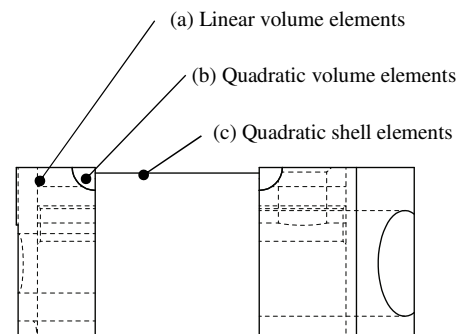


Figure 5.16: Side view of a leaf spring with the element regions indicated.

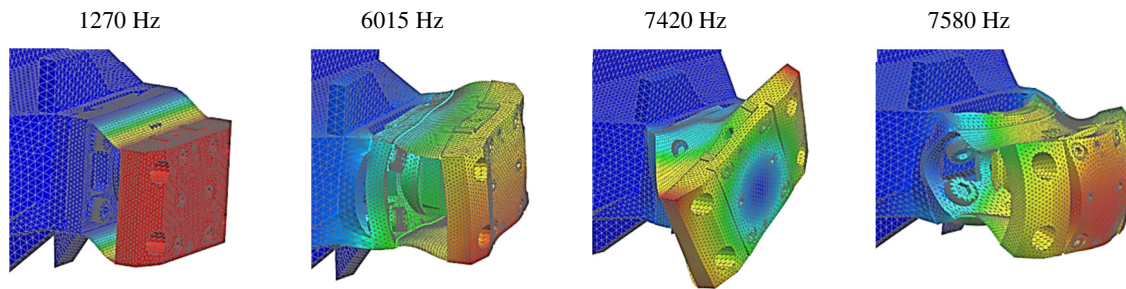


Figure 5.17: Four lowest natural frequencies and corresponding mode shapes of the RMD while mounted to a stage corner.

for a correct stiffness estimation. Quadratic shell elements are applied in the leaf springs because of the bending load. Different elements are used between these shell elements and the volume elements of the masses. Figure 5.16 shows the element regions. Quadratic shell elements (c) are applied in the leaf springs. These are modelled at the center line of the leaf springs. The masses are modelled with linear volume elements (a) as this introduces a minimum number of equations and nodes. The transition region (b) between the leaf springs and the rigid masses contributes significantly to the compliance of the leaf springs. Quadratic volume elements are applied in this transition region to model this correctly.

The element size in area (a) decreases towards area (b) to connect elements with equal sizes. Connection elements provide the coupling between the shell elements and the volume elements.

#### 5.4.2 Damping mechanism design

Figure 5.18 shows the LVE fluid damper fin and slot part. The upper part is the fin part and the lower part is the slot part. The fin part contains six fins with a tapered shape for stiffness reasons. The fins are of different lengths and contain fluid on both sides. See Table 5.6 for the dimensions. Dowel pins fixate the position of the fin with respect to the slot part. The position is locked by mounting bolts. A flexible encapsulation fits in the grooves to contain the fluid.

#### 5.4.3 Undamped characterization

A total amount of 5 dampers is produced and all 5 dampers are characterized: firstly, the frequency response functions of all dampers are measured without fluid applied. This results in an undamped frequency response function, which shows the natural frequency of the damper. Each damper is measured two times: with and without fin mounted. These measurements are presented in Figure 5.19. The mass difference results in separated natural frequencies from which the moving mass and stiffness can be derived. After correction for the actuator coil the damper mass results. Figure 5.21 shows all 10 measurements, 5 with fin and 5 without fin. It shows a natural frequency deviation less than 5 Hz, which is less than 0.4 %. Table 5.7 lists the resulting parameters.

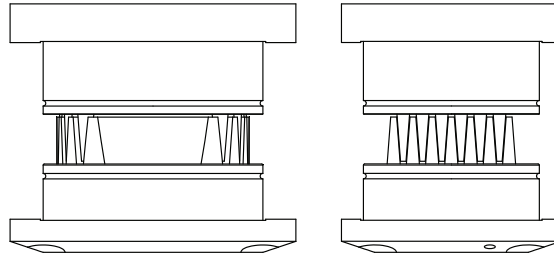


Figure 5.18: A side view and a front view of the fin and slot parts. The corresponding dimensions are presented in Table 5.6.

Table 5.6: Dimensions of the fins as shown in Figure 5.18.

| Damper dimensions          | Value  | Unit          |
|----------------------------|--------|---------------|
| Length fin 1               | 17,1   | mm            |
| Length fin 2               | 15,3   | mm            |
| Length fin 3               | 12,2   | mm            |
| Height fins                | 4,0175 | mm            |
| Gap width                  | 50     | $\mu\text{m}$ |
| Geometrical damping factor | 14,33  | m             |

#### 5.4.4 Damped characterization

The dampers are characterized with the fluid applied to validate the damping behavior. This measurement is compared with a prediction based on the LVE fluid model. Figure 5.21 shows both the measurement and the model predicted behavior. The upper plot shows the magnitude plot of the measurement and the lower plot shows the error between the fit and the model. This error plot also shows the fact that the frequency region between 3100 Hz and 8500 Hz is excluded from comparison, because of the higher order dynamics present in the measurement. The damper behavior is well estimated up to 2 kHz. The largest magnitude difference is shown in the figure and amounts 5.54 dB, which equals a factor 1.9. This difference is mainly due to the fluid model, which overestimates the damping between 2 and 5 kHz. This overestimation is induced by the measurement setup which is used to characterize the fluid.

The derivation of the fluid model is described in Chapter 4 and it discusses the low sensitivity of the setup at higher frequencies, which causes this error in the fluid model. In addition, a part of the frequency region was left out in the fitting procedure, caused by parasitic dynamics in that frequency range. The difference is elaborated upon in detail in Appendix B – Improved LVE fluid model.



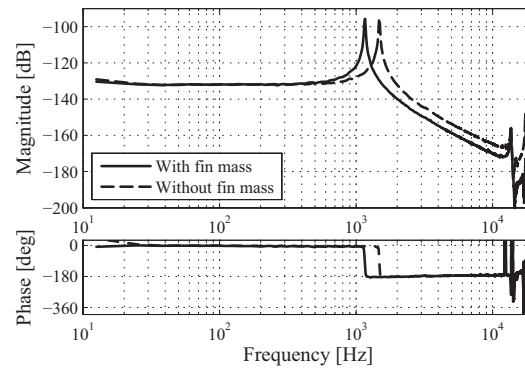


Figure 5.19: Measured FRFs of the RMD mechanism with and without fin. This difference in mass results in the shift in natural frequency.

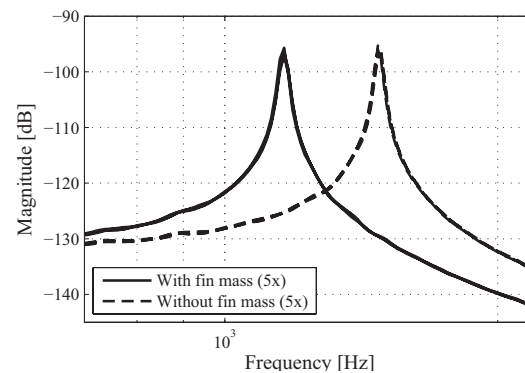


Figure 5.20: Detail plot of Figure 5.19 around the resonance frequencies. These measurements show the very small differences between the behavior of the mechanisms.

### 5.5 Experimental modal analysis on the motion stage

An experimental modal analysis is executed to validate the performance increase that has been calculated using the broad banded optimization as presented in Section 5.3.4. Firstly, undamped measurements are performed. The motion stage is excited by an impulse hammer to excite the high-frequency stage modes. An accelerometer is used as sensor. Three measurements are averaged per measurement location to obtain a qualitatively good

Table 5.7: Measured and calculated parameter values. Average values over the 5 RMDs are used due to the small differences in natural frequencies.

| Measured data                 | Value   | Unit |
|-------------------------------|---------|------|
| Natural frequency with fin    | 1160,3  | Hz   |
| Natural frequency without fin | 1478,2  | Hz   |
| Mass fin & bolts              | 28,84   | g    |
| Mass coil & screw             | 10,08   | g    |
| Calculated data               |         |      |
| Moving mass                   | 65,05   | g    |
| Leaf spring stiffness         | 4,0E+06 | N/m  |
| Natural frequency damper      | 1247    | Hz   |
| Error w.r.t. design target    | -1,81   | %    |

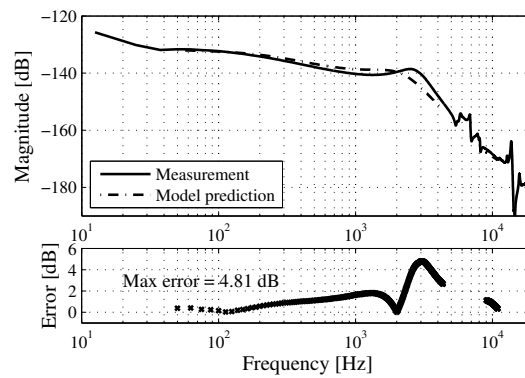


Figure 5.21: FRF measurement and model prediction of the RMD with fluid applied.

measurement. The undamped natural frequencies and corresponding mode shapes are calculated to validate the frequency response functions. Subsequently, the dampers are added and the frequency response functions are measured again. The assembled stage with dampers is presented in Figure 5.22.

#### 5.5.1 Frequency domain results

The accelerometer is added to the stage's corner to measure the flexible modes that are visible

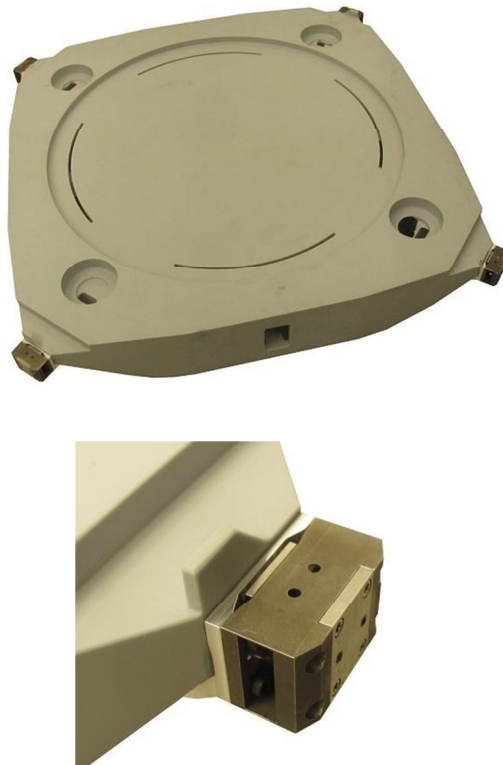


Figure 5.22: The upper plot shows a photograph of the stage with RMDs added. The lower plot shows a detail view of an RMD, mounted to a stage corner.

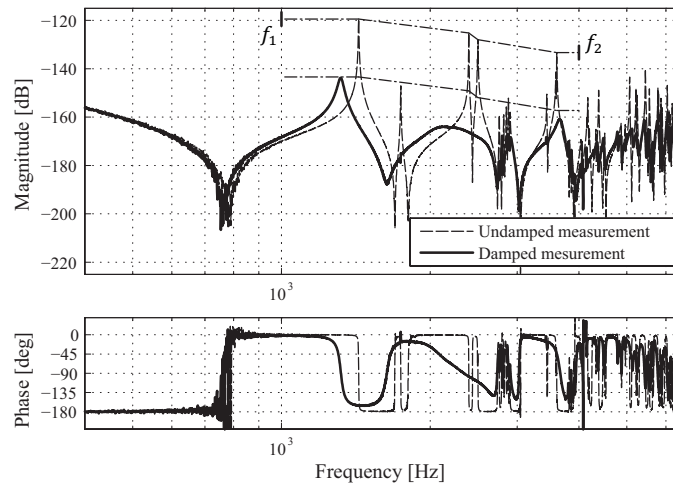


Figure 5.23: Measured FRF with the suppression factor between 1 and 4 kHz indicated by the two lines.

at the sensors during machine operation. To be sure that these modes are excited, the actuation point is at the same corner. This results in a collocated frequency response function. Figure 5.23 presents two of these frequency response functions, with the phase between -180 deg and 0 deg. The cost function is added in the graph, as in Figure 5.12, to facilitate comparison. The undamped frequency response function is measured with the accelerometer slightly off-diagonal to show resonances 8 and 12, which are excluded from the damped measurement by shifting the accelerometer to the stage diagonal. This sensor location clearly shows the damping of modes 7, 9, 10/11, and 13. The resonances shown in the frequency region slightly below 3 kHz are not visible in Figure 5.12. Two reasons can be found for this appearance: 1) in the results of the FEM analysis, these natural frequencies are overestimated. This might be due to the limited element size in the FEM model which introduces relatively large elements with respect to local plate thicknesses and feature sizes. An overestimation of the local stiffness will result and, therefore, an overestimation of the natural frequencies. A more likely reason is that 2) an asymmetry is present in the measurement due to a shift of the accelerometer with respect to the stage diagonal or production tolerances and damage that is present on the hardware which distorts the stage's symmetry.

Table 5.8: Table with suppression factors corresponding to resonance frequencies indicated in Figure 5.24.

| Mode number    | Value [dB] | Factor [-] |
|----------------|------------|------------|
| Mode # 7       | -24,3      | 16,4       |
| Mode # 9/10/11 | -38,7      | 86,1       |
| Mode 13        | -26,6      | 21,4       |
| Mode a         | -19,7      | 9,7        |
| Mode b         | -22,0      | 12,6       |
| Mode c         | -21,1      | 11,4       |
| Region d       | -14,9      | 5,6        |

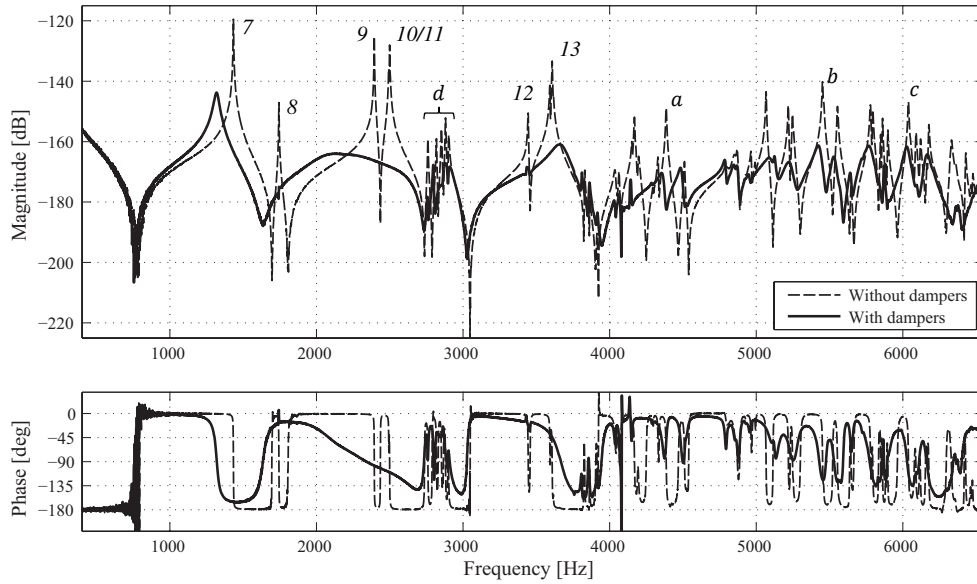


Figure 5.24: The measurement plotted on a linear frequency scale. The mode numbers are indicated in the graph. The undamped FRF is measured with the accelerometer slightly off-diagonal, which shows resonances 8 and 12. The damped FRF is measured with the accelerometer on the stage diagonal.

Table 5.8 lists the resulting suppression factors, which can be interpreted as estimations for the increase factors of the modal damping of these modes. The first three rows of Table 5.8 fit within the frequency range of the cost function. The suppression factor calculated by the optimization is 23.7 dB, see Section 5.3.4. The first value in Table 5.8 shows -24.3 dB. This value is larger than predicted. However, if the overestimation of the modal damping in the initial model of 1.1 dB is taken into account, this value is slightly lower than predicted. For the other modes within the cost function range, the suppression is higher than predicted. The prediction showed a higher suppression for mode 9, 10, and 11 than for mode 7 and 13. This is correct and visible in Figure 5.23. Above the cost function frequency region, three resonances are listed to show the high-frequency suppression: respectively, regions *a*, *b*, and *c*. The corresponding suppression values are listed in Table 5.8.

### 5.5.2 Time domain results

Figure 5.25 shows the time domain results for the undamped case and the damped case as measured by the accelerometer. Table 5.9 lists the corresponding values. The responses are normalized at their initial amplitudes and the settling time is defined as the time needed to decrease the amplitude by 95 %. The settling time ratio amounts 20 times. This shows that the damped response is decreased 20 times faster to 5 % remaining amplitude than the undamped response. This value is in the same order of magnitude as the first and third suppression factors in Table 5.8. It slightly depends on the adjusted settling time percentage. The total response is a superposition of the responses of all modes.

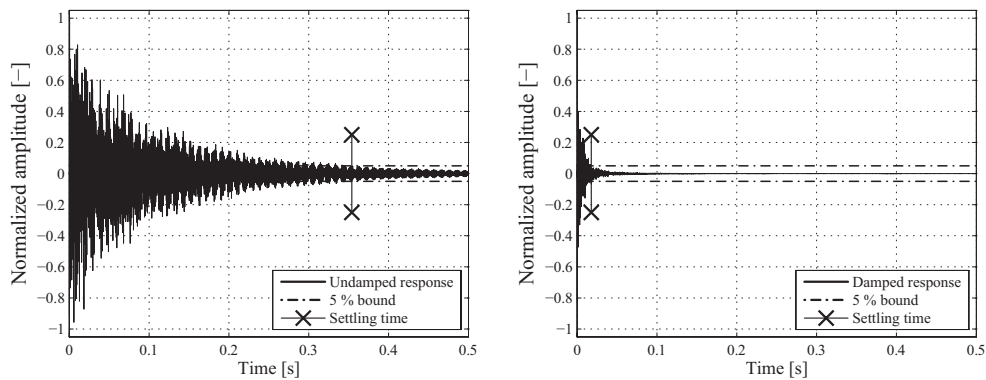


Figure 5.25: a) the undamped normalized time response. The line of 5 % amplitude is indicated. The vertical line represents the time at which the amplitude equals this 5 % of the initial amplitude. b) the behavior for the damped case with the same settling time criterion.

Table 5.9: Time domain results for the undamped and damped cases.

| Name                     | Value  | Unit |
|--------------------------|--------|------|
| Settling time percentage | 5      | %    |
| Undamped settling time   | 0,3540 | s    |
| Damped settling time     | 0,0177 | s    |
| Settling time ratio      | 20,0   | -    |

These modes all contain different modal damping factors. In addition, it includes the low-frequency suspension modes of the stage. These modes are visible in Figure 5.26, which shows a detail of Figure 5.25b. This rigid body response contains low-frequencies and low damping values. Therefore, this response remains over time as the other responses already have faded. Figure 5.26 shows that the amplitude has decreased to 0.1 % of the initial response after 0.17 s.

## 5.6 Concluding remarks

This chapter shows an approach to add damping to a range of resonances of a motion stage by adding robust mass dampers. Analysis is performed to calculate the damping increase

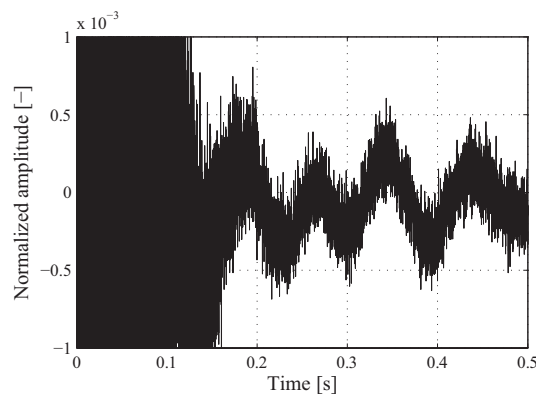


Figure 5.26: Detail of the transient response in which the suspension modes are visible with a frequency around 11.6 Hz.

beforehand, and experiments are conducted to validate the behavior of both 1) the damper behavior and 2) the stage with dampers added. The robustness of the dampers, i.e., the magnitude of the damper's modal damping value, is induced by resonances that are included in the frequency range that is set in the optimization. Both specific solutions (TMD) and broad banded solutions (RMD) can be obtained in this way by adjusting the frequency range. Analytical results of both solutions are shown. The linear viscoelastic fluid model is included in the optimization procedure.

The broad banded solution is elaborated in detail, in which a resonance suppression of at least 24.3 dB is realized between 1 and 4 kHz, with an overall mass increase of less than 2 %: 1.15 % as effective moving mass (4 x 65g) and 0.85 % as parasitic mass contributing to the stage structural mass. The transient time response of the damped stage is 20 times faster compared to the undamped stage. This corresponds to the increase in modal damping values.

The overall frequency response function of the damped motion stage showed predictable behavior: the suppression factors correspond well to the calculations. The amount of suppression between 1 and 4 kHz amounts at least 16.4 times (24.3 dB) and the measurements showed that the damping, in addition, is present up to at least 6 kHz by a factor 9.7 (19.7 dB).

The robustness, as one of the most important properties of the RMD, see Section 5.3.5 for the robustness analysis, is proven: the suppression factor is well predictable despite different errors and estimations:

- Stage model errors: the natural frequencies resulting from the FEM model are an overestimation of the real frequencies,
- The state space model is not corrected for modal truncation,
- Fluid model errors,
- A simplified 1 DoF model is applied as damper model,
- Production tolerances are not taken into account during analysis. These tolerances influence both the natural frequency and damping value of the damper design. The dampers as produced and validated however, show extremely similar behavior.

After comparison of the optimization results with LVE fluids and purely viscous fluids applied as damping material, it appears that LVE materials enable larger suppression factors than pure viscous fluids, using the same damper mass, see Section 3.2, Table 5.3 and Table 5.4. This is elaborated upon in more detail in Appendix B – Linear Viscoelastic damping materials.

## 5.7 Closing remarks

### 5.7.1 Discussion

The damping improvements as shown are very useful in the approach to design stages for motion control. The damper is designed such that the overall damped system remains as an LTI system. This enables the application of loop-shaping procedures for the damped stage.

In this chapter, the dampers are added to the stage as separate devices. This enables us to design a stage and increase the modal damping afterwards by adding RMDs. However, in existing mechanical designs in general, it might be possible that the most effective locations to add damping to a mode are not usable because of other devices that are mounted at those positions. Therefore, the RMD design should be included in an early stage design phase to have the most effective locations still available. A side effect of including the RMD design in an early design phase is that the mounting mass, needed to connect the moving mass to the stage and containing the slot part, can be more integrated in the structural mass of the stage and thereby the amount of passive mass decreases. In addition, the mass contribution can be decreased further if existing components are applied as damper masses.

An extension of this thought is ‘design for damping’: Section 2.1.5 showed the maximal suppression of a certain mode is determined by the squared amplitude of this mode at the damper location. This indicates that the stage can be designed in such a way that large amplitudes occur at the damper locations. An example is the build out of the stage’s corners: this enlarges the amplitude of the corners and therefore increases the effectiveness of the dampers.

### 5.7.2 Implications

Tuned mass dampers are well known in literature. The equations are proven to calculate the optimal suppression factor, natural frequency, and damping ratio. In these equations, the damper behavior is assumed to be purely viscous. We showed that larger suppression factors are possible than presented in [25] by using visco-elastic fluids as damping medium. Although this effect is relatively small for single resonance suppression, because of the small banded character, it is larger for broad banded resonance suppression. The damper benefits from the frequency dependent stiffness of the fluid. This is an additional reason, besides the complex stage dynamics, for the application of optimization algorithms: the damper properties vary as function of frequency.

The bandwidth of a closed-loop system can be increased by increasing the damping as shown in this chapter along two ways: 1) a suppression factor of 16.4 indicates that the diameter of the resonance circle in the Nyquist diagram has decreased by this factor, which creates room for more gain in the controller. In addition, 2) the robustness increase can lead to reconsideration of the robustness margins in controller design at specific frequency regions: if the robustness of the high-frequency modes is increased, the robustness margins can be adapted at these frequencies, which creates additional room for controller gain.

The effect of broad-banded resonance damping is shown on the basis of a motion control specific problem. However, this solution principle might be of value in other fields of application too. Examples are:

- space structures: these typically contain low damping and a broad frequency spectrum is applied during the launch,
- automotive applications: the excitation frequency depends on the velocity of the vehicle or on the engines' rotational velocity,
- structural engineering: tall structures often show one specific dominating natural frequency for which many types of TMD's have been designed. However, other structures like bridges often show many natural frequencies over a certain frequency range which are more related to the RMD as presented,
- wafer handler robots: these slender structures show position dependent natural frequencies, which can be counteracted by the broad banded dampers.

#### **5.7.3 Further research possibilities**

Linear viscoelastic fluids can be designed specifically for optimal resonance suppression over a certain frequency range. The viscosity and elasticity, as function of frequency, should be adjusted to obtain effective damping materials for a specific damper design. An easy way is possibly creating a blend of existing fluids with different properties. More complex procedures can be used to design problem specific fluids. Although this results in improved performance, the increase in suppression factor is expected to be relatively low.

To increase the bandwidth of a certain motion system maximally, closed-loop analyses should be performed: not all resonances in a frequency response function are BW limiting. Therefore, more specific frequency regions have to be determined to be affected by the RMD's in combination with controller design. For that purpose, optimization algorithms can be applied to optimize both the damper and the controller parameters simultaneously.

Another research path to increase the performance further is by topology optimization with damping included. State-of-the-art experimental optimization algorithms are intended to optimize the frequency response function of the plant based on the SIMP method. Damping is not specifically included in these types of optimizations. As a future approach, a number of RMDs can be optimized simultaneously with the stage design.





# Closed-Loop Performance Optimization and Experimental Validation

**Abstract** – This chapter presents closed-loop performance improvements obtained at a prototype motion stage design. A motion stage with low modal damping values is adapted by adding Robust Mass Dampers to enable a higher controller gain. An optimization approach is presented to determine parameter values for the RMDs in order to maximize the performance of the closed-loop system. Validation is provided by implementation on an experimental setup. A low-frequency sensitivity improvement of 9 dB is proven in the vertical direction of motion for a  $PID^+$  controller by experimental validation on a 6 DoF multi SISO experimental motion stage. This corresponds to an increase of the cross-over frequency of 50 %. In addition, two rotational directions benefit from the added dampers and show a sensitivity decrease of 3.5 dB. Finally, the torsion mode, which is not visible in the frequency response function in z-direction, shows a modal damping increase factor of 4.5. These improvements are established without changing the robustness margins.

## 6.1 Introduction

### 6.1.1 Position controlled stages

Precision motion systems are applied in different industries [27]. One of these is the semiconductor industry, in which position controlled stages are used in wafer scanners to position a wafer with respect to an optical column. Patterns of electronic devices or micro-electro-mechanical systems (MEMS) are projected on the surface of this wafer. Two key properties in these devices are velocity and accuracy. The first property contributes to the throughput and the second one to the smallest feature size that can be created with a wafer scanner. The motion stage in such a scanner is usually position controlled in 6 degrees of freedom by a motion control system [92]. This system contains two parts:

- a feedforward part, which uses the reference signal, combined with an inverse plant model to create large forces in order to accelerate the stage,
- a feedback part, which:
  - stabilizes the control loop,
  - counteracts unexpected disturbances,
  - compensates for mismatches in the feedforward model.

Although at least 95 % of the acceleration forces are generated by the feedforward path [17, 59, 77, 103], the feedback loop is indispensable to counteract all phenomena that are not included in the models. A measure of the reaction rate of the feedback loop is the bandwidth. The bandwidth is defined as the open-loop cross-over frequency and gives an indication of the frequency up to which the open-loop gain is larger than 1 and, therefore, the closed-loop gain is approximately 1. Up to this frequency, the closed-loop system is able to track a harmonic setpoint. This bandwidth is, in motion stages, limited by the flexible behavior of the mechanical stage design. Fundamental performance limitations for two-degree-of-freedom systems are derived in [38, 60] and the limitations of multivariable systems are addressed in [37, 78].

These flexibilities appear at specific frequencies, depending on the mechanical design of the motion stage and the mechanical properties of the material applied. The higher the natural frequencies can be designed, the higher the bandwidth that can be reached: this argues for light and stiff mechanical designs. Another factor that influences the reachable bandwidth is the modal damping that is present at these resonance frequencies. Low modal damping factors result in large amplification factors of the steady state vibration amplitudes. Larger modal damping values limit the resonance's amplification factor and, therefore, higher bandwidth values can be obtained. Some solutions from a control point of view are:

- the addition of notch filters to the controller structure, which changes the open-loop characteristics in a specific frequency range. Although this solution is effective, it is often non-robust: if the structure's dynamics changes by for instance temperature differences, wear and tear, etc. the notch is not placed correctly anymore and the advantages vanish [81],

- the placement of additional actuators and sensors. This enables to close additional control loops and is called over-actuation [39,82]. In these approaches often decoupling strategies are applied, which enables for SISO controller design [93].

In addition, robust modeling and robust control strategies have been developed to counteract the drawbacks of the above mentioned solutions [66,98,99,100].

This indicates that a lot of effort is put in controller design for complex mechanical systems, however, the largest amount of poles and zeros of the system is introduced by the mechanical design. Therefore, a systematic way of improving the closed-loop behavior by adapting the open-loop damping characteristics can be very useful.

A way to increase the modal damping of a motion stage is by adding Robust Mass Dampers (RMDs) at specific stage locations. The RMDs are based on a linear viscoelastic fluid in order to create damping behavior. The advantages of RMDs on the open-loop characteristics are elaborated upon in Chapter 5, in which the RMD parameters are determined based on an open-loop criterion in order to introduce broad banded damping to the flexible behavior.

#### **6.1.2 Performance optimization**

In order to address the problem of bandwidth limitation, the closed-loop behavior has to be investigated. The closed-loop behavior can be described by the plant and the controller. Therefore, a controller structure has to be defined in order to specify the bandwidth limitations. For motion control problems, the  $PID^+$  controller is widely used, which mainly acts as a parallel spring-damper combination due to the proportional gain and the differentiator. An integrator is applied to force the steady state error to zero and a low-pass filter is used to suppress high-frequency noise and suppress high-frequency resonances. The proportional gain and differentiator are able to stabilize the closed-loop system, due to the phase lead introduced by the lead filter. In general, not all resonances are limiting the bandwidth: an example is given by a collocated frequency response function, in which the bandwidth is not limited at all by the resonances for the controller structure as discussed. Bandwidth limits arise due to non-collocated resonances at which the phase decreases to  $-360$  deg: a  $PID^+$ -type controller is not able to compensate for this phase lag and a BW limitation is included in the system. In practical motion stage designs, actuators and sensors are usually not installed on the same locations and, therefore, bandwidth limits are present. The bandwidth itself is a meaningless measure due to the uncorrelated behavior with the disturbance suppression at low frequencies: a high bandwidth can be obtained by a broad lead filter frequency range and lower controller gain. However, the corresponding controller gain contributes importantly to the disturbance suppression factor at low frequencies. Therefore, the sensitivity at low frequencies is used as performance criterion. This is elaborated on an iterative basis in Chapter 3.

### 6.1.3 Chapter contributions & Content

This chapter shows a performance improvement of a motion stage in z-direction. An optimization approach is given which enables to calculate this improvement factor beforehand. In addition, an improvement is presented in the rotational directions and a modal damping increase is obtained for the torsion mode, which is excluded from the previous results due to actuator and sensor placement in combination with design of the decoupling matrices. To prove these improvement factors, experimental validation is presented and a detailed analysis of the behavior is given.

The problem formulation for a specific stage design and damper configuration is given in Section 6.2. The optimization procedure, including the dynamic models, is presented in Section 6.3. An example of the optimization procedure is elaborated in Section 6.4 and optimization results are shown and compared in Section 6.5. The experimental validation is presented in Section 6.6: measurement results, both in the frequency domain and time domain support the theoretical results. Additional advantages of the application of RMDs are described in Section 6.7. Section 6.8 presents concluding remarks and Section 6.9 presents a discussion, in which special attention is paid to the optimization approach as used in this chapter and the other approaches that can be used.

## 6.2 Experimental motion stage

### 6.2.1 Stage design

Figure 6.1 shows an experimental motion stage setup. This is a 6 degree of freedom (DoF) motion system which can travel over small strokes to investigate the dynamical behavior. The motion stage is shown in Figure 6.1b and shows a relatively large length-height ratio, which makes it difficult to design high out-of-plane natural frequencies. In total, 8 actuators are present: 4 in horizontal direction and 4 in vertical direction. The in-plane displacements are measured by 3 horizontal sensors and the vertical displacements are measured by 4 sensors at the stage's corners. The stage's corners show pockets which enable to mount dampers without crossing the outer contour of the stage.

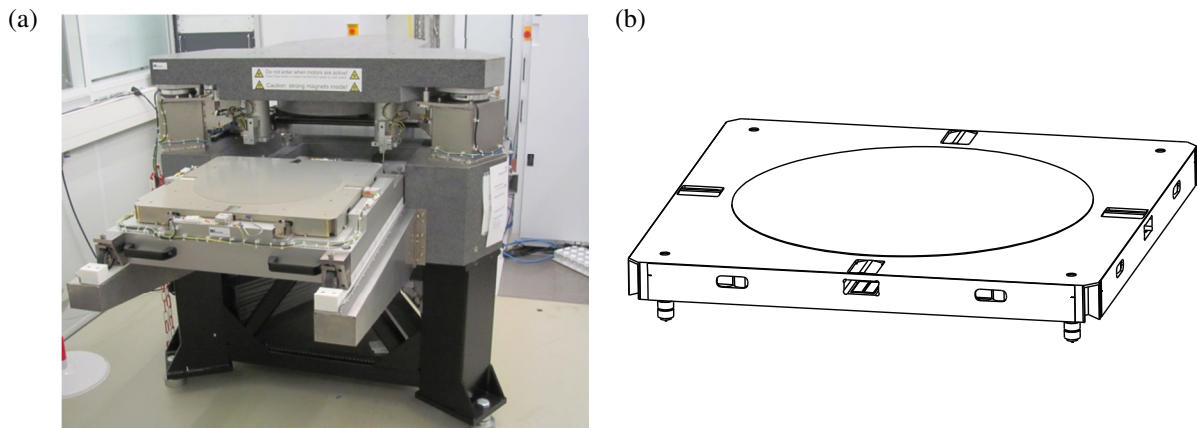


Figure 6.1: a) Photograph of a 6 DoF experimental motion stage setup. b) View of the motion stage's CAD model.

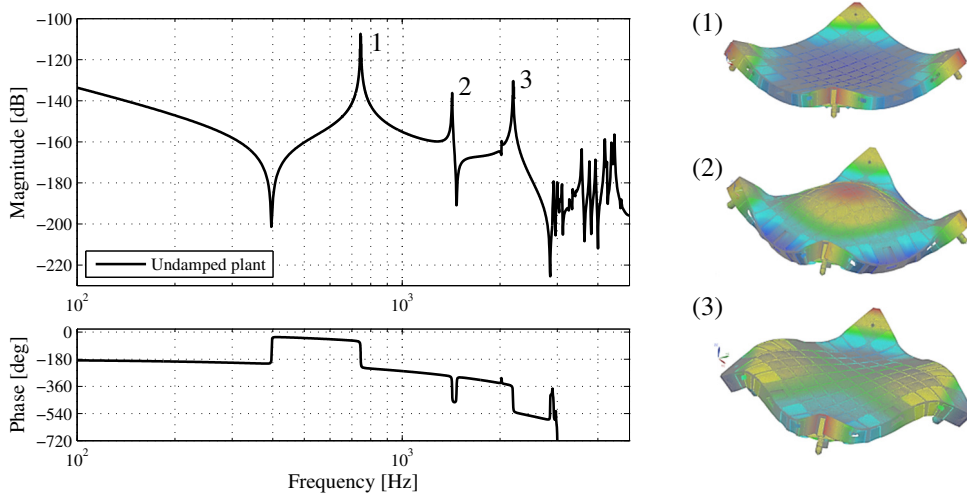


Figure 6.2: Discrete-time SISO frequency response function of the stage in z-direction after decoupling. Note the phase delay due to the time delay included in the model. The first three resonances that are visible in this frequency response are presented at the right.

A CAD model of this stage is created. It includes the structural stage parts and the locations of functional components such as actuators and sensors. A FEM model is created based on the CAD model and an undamped modal analysis is performed which results in the stage's undamped natural frequencies and mode shapes. In this FEM model a combination of volume elements and shell elements is used, to represent the mechanical behavior in a correct way. The natural frequencies and mode shapes are used to create a 6 DoF state space model in modal coordinates [33]. This dynamic model is a multi-input/multi-output state space model containing 7 outputs and 8 inputs. This model is validated by calculating these frequency responses by superposition of the responses of the undamped modes in FEM.

Actuator transformation matrix  $T_u$  and sensor transformation matrix  $T_y$  are applied as pre- and post-multiplication matrices for geometrical decoupling. This results in a transfer function matrix with 6 in- and outputs with the RGB motion directions as dominant behavior on the matrix diagonal components. This enables to design SISO controllers for the plants as present on the diagonal components. The gains in the transformation matrices are validated by calculating the height of the mass lines in the SISO frequency responses for low frequencies. These lines represent the moving mass of the SISO motion directions.

The control system shows a time delay due to sampling and internal delays. This delay is estimated from a measurement and is included in the model by transforming the model from the continuous  $s$ -domain to the discrete  $z$ -domain. In case of a zero-order-hold discretization, this introduces a time delay of half the sampling time. The remaining delay time is included in the model as internal delay.

Figure 6.2 shows the SISO frequency response function of the motion stage in z-direction. In addition, the first three appearing non-rigid body modes are visualized. The first non-rigid body mode of a plate-like structure as this stage design is usually the torsion mode, which is not visible in Figure 6.2. This is due to the four actuators and sensors in z-direction, which

enable to decouple the torsion mode in a seventh SISO loop and control it with a separate controller. This specific controller is not applied in this chapter.

### 6.2.2 Damper design

Figure 6.3a presents a robust mass damper design that can be mounted in the pockets at the stage's corners. The damper mechanism is based on monolithically designed flexures which introduce forces based on relative displacement differences and connect the moving mass with the base part. The mechanism that creates the velocity dependent damping force is located between the two flexures. This damping mechanism is based on the shear principle and contains a high-viscosity linear viscoelastic fluid inside to generate the damping force. The different functional parts are indicated in Figure 6.3a. Figure 6.3b shows the position as mounted on the stage's corner. The behavior of the RMD as shown above can be characterized by mainly three parameters:

- the moving mass  $m_{RMD}$ ,
- the natural frequency  $\omega_{RMD}$ ,
- the modal damping factor  $\zeta_{RMD}$ .

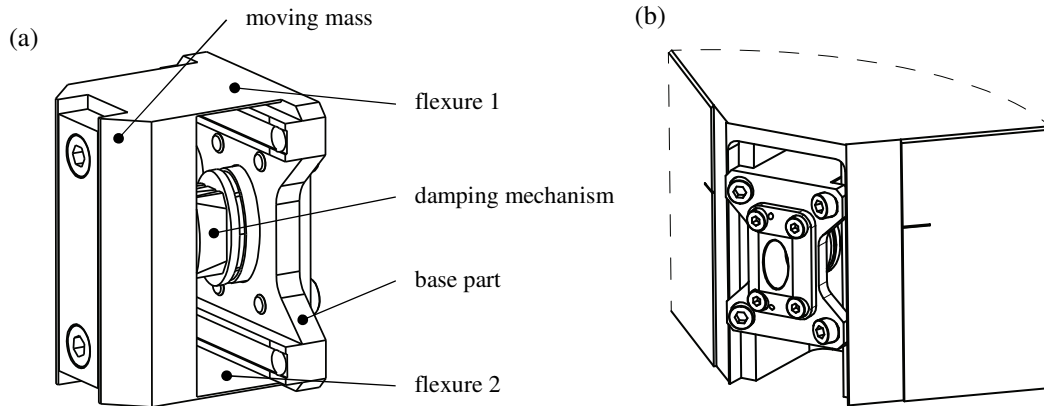


Figure 6.3: a) Impression of the robust mass damper design. b) The RMD integration at the stage's corner.

The flexure stiffness is determined by the geometry of the flexures and the material applied. The dimensions of the flexures are design parameters, which can be determined as function of the RMD's natural frequency  $\omega_{RMD}$  and the moving mass  $m_{RMD}$ . The RMD's modal damping  $\zeta_{RMD}$  can be estimated by the applied fluid and the geometry of the damping mechanism. This damping mechanism geometry is expressed in one parameter called geometrical damping factor ( $GDF$ ) and is defined as the ratio of the fluid contact area  $A$  and the gap width  $h$ . The  $GDF$  is a parameter used in the elaboration of the RMD damper components. The relation between  $GDF$  and the other RMD parameters  $m_{RMD}$ ,  $\omega_{RMD}$ , and  $\zeta_{RMD}$  is given by:

$$GDF = \frac{A}{h} = \frac{2 \cdot m_{RMD} \cdot \zeta_{RMD} \cdot \omega_{RMD}}{\eta_{ZSV}} \quad (6.1)$$

In this equation,  $\eta_{ZSV}$  indicates the zero shear viscosity (ZSV) of the fluid. Due to the linear viscoelastic fluid behavior as function of frequency, only an estimate of the RMD modal damping can be given, based on low-frequency behavior in which the fluid is determined by the static viscosity. Chapter 4 provides the fluid characterization procedure and the corresponding fluid models. A dynamic model of the RMD has been presented, which includes the fluid model, and is used in the analyses of this chapter, see Figure 4.11. This damper model contains a moving mass and a mounting mass. The amount of moving mass determines the amount of resonance suppression that can be obtained at a certain resonance frequency. The mounting mass however, contributes only to the modal mass of the stage and, therefore, affects the natural frequencies of the stage, which is detrimental for the performance. The mounting mass is estimated to be 0.7 times the moving mass. This shows that an increasing amount of moving mass simultaneously increases the base mass, which is negative for the results.

### 6.3 Closed-loop parameter optimization

The parameters of the dampers have to be determined for optimal performance of the closed-loop system in z-direction. Therefore, a closed-loop optimization criterion is formulated which includes parameters of both the dampers and the controller. This optimization problem is formulated as:

$$\min_{x \in \mathfrak{R}} J(x) \quad (6.2)$$

subject to:

$$lb \leq x \leq ub \quad (6.3)$$

$$Ax \leq b \quad (6.4)$$

$$C(x) \leq 0 \quad (6.5)$$

To calculate a correct and usable solution, the resulting parameter values should satisfy the following requirements:

- 1) a sensible performance criterion has to be defined,
- 2) the amount of damper mass should be limited,
- 3) the RMD natural frequency should exceed the BW of the closed-loop system,



- 4) robust damper behavior has to be obtained,
- 5) useless combinations of controller parameters should be avoided,
- 6) closed-loop stability has to be enforced,
- 7) closed-loop robustness margins should be included.

### 6.3.1 $PID^+$ controller

The implementation of the above requirements in the optimization procedure is as follows: Firstly, as stated in the first requirement, a sensible performance criterion has to be determined to maximize the performance of the control loop. The absolute value of the complex sensitivity function, further referred to as sensitivity, at low frequencies is a useful measure of controller gain and corresponding bandwidth, see Chapter 3. This low-frequency sensitivity value describes the ability of the control system to counteract low-frequency position disturbances. In case of a  $PID^+$  type controller, the sensitivity function shows a +3 slope (+60 dB/dec) for frequencies below the integrator turnover frequency  $\omega_i$ . Each point in the frequency range of the integrator, therefore, can be used as broad-banded measure of the controller gain at low frequencies. The frequency at which the sensitivity is evaluated for the cost function  $J(x)$  is called  $\omega_{LF}$ . This introduces the definition of the cost function:

$$J(x) = |S_Z(x, \omega_{LF})| \quad (6.6)$$

Vector  $x$  contains the parameters of the dampers and the turnover frequencies of the PID controller:

$$x = \left[ m_{RMD} \quad \omega_{RMD} \quad \zeta_{RMD} \mid k_p \quad \omega_i \quad \omega_{ld,z} \quad \omega_{ld,p} \quad \omega_{lp} \quad \zeta_{lp} \right]^T \quad (6.7)$$

The first three parameters  $m_{RMD}$ ,  $\omega_{RMD}$ , and  $\zeta_{RMD}$  correspond respectively to the mass, undamped natural frequency, and the modal damping factor of the RMDs. The remaining 6 parameters describe the controller parameters: the proportional gain, the frequencies of, respectively, the integrator  $\omega_i$ , the zero and pole of the lead filter  $\omega_{ld,z}$ ,  $\omega_{ld,p}$  and the second order low pass filter  $\omega_{lp}$ . The last component  $\zeta_{lp}$  describes the modal damping of the low pass filter.

The upper and lower parameter bounds define the parameter space and, therefore, the average order of magnitude of the parameters:

$$lb \leq x \leq ub \quad (6.8)$$

These magnitudes are used for scaling during optimization to improve the convergence rate. In addition, the lower bounds make that requirement 3 and 4 are satisfied by setting lower values for the natural frequency and modal damping of the RMDs. The upper bounds limit requirement 2: the RMD mass.

Linear inequality constraints are applied of the form:

$$Ax \leq b \quad (6.9)$$

which describe linear relations between the components in the parameter vector  $x$ . The following three constraints are applied, in accordance with constraint 5:

$$\omega_i \leq \omega_{ld,z} \quad (6.10)$$

$$\omega_{ld,z} \leq \omega_{ld,p} \quad (6.11)$$

$$\omega_{ld,p} \leq \omega_{lp} \quad (6.12)$$

Non-linear inequality constraints are defined as:

$$C(x) \leq 0 \quad (6.13)$$

In which  $C(x)$  contains the closed-loop stability criterion and the robustness margins of the closed-loop system, according to constraints 6 and 7. For the stability criterion, the real parts of the closed-loop poles are included, which should be negative for stability and the robustness margin is included by limiting the maximum value of the sensitivity  $S(x, \omega)$  to a maximum value  $S_{max}$ . These two statements result in the following equations:

$$Re\{pole(S(x))\} \leq 0 \quad (6.14)$$

$$max(|S(x)|) - S_{max} \leq 0 \quad (6.15)$$

### 6.3.2 Extension with notch filters

To enable further closed-loop performance improvements, the controller can also be extended with a notch filter to deal with higher order stage dynamics. The same optimization problem is used. The parameter vector  $x$  is extended by four components for a free notch filter:

$$x_{N,f} = \left[ x^T \mid \omega_{n,z} \quad \varsigma_{n,z} \quad \omega_{n,p} \quad \varsigma_{n,p} \right]^T \quad (6.16)$$

In this definition  $x$  is the parameter vector as shown in (6.7) with dampers and PID<sup>+</sup> controller included. The frequencies of the zeros and poles are included in  $\omega_{n,z}$  and  $\omega_{n,p}$ . The damping factors corresponding to these zeros and poles are described by  $\varsigma_{n,z}$  and  $\varsigma_{n,p}$ , respectively.

In case of a pure notch filter the frequencies of the zeros and poles are equal  $\omega_{n,z} = \omega_{n,p}$ . This results in the possibility to redefine the parameter vector in the following form:

$$x_{N,p} = \left[ x^T \mid \omega_{n,zp} \quad \varsigma_{n,z} \quad \varsigma_{n,p} \right]^T \quad (6.17)$$

in which parameter  $\omega_{n,zp}$  is used for both the zeros and the poles in the notch filter. This reduces the parameter vector length by one and decreases the number of constraints. Especially in optimization algorithms, the presence of equality constraints increases the difficulty of the problem, therefore, this redefinition of the parameter vector is useful in case a pure notch filter is applied instead of a free notch filter.

If the notch filter frequency parameters are located in the same frequency region as the cost function  $\omega_{LF}$ , the notch filter can be used to introduce a sharp notch in the sensitivity at frequency  $\omega_{LF}$ . Although this improves the cost function value substantially, it does not contribute to the quality of the solution. This unwanted behavior is prevented by adjusting the lower bounds well for these parameters.

#### 6.4 Practical elaboration of the optimization procedure

This section describes the approach to find the optimal solution. The first three components of parameter vector  $x$  – the RMD parameters – are used to calculate the damped plant model containing 6 degrees of freedom. Subsequently, the multi SISO plant model is calculated by the geometrical decoupling procedure and the transfer function in  $z$ -direction is selected for further analysis. The open loop is calculated by multiplication of the plant and the controller.

This optimization formulation has a non-convex character, as many controller optimizations have, which indicates that many local optima exist within the parameter space. A genetic algorithm is applied to find the global optimum within the parameter space [48,50,7]. This algorithm starts with an initial population calculation of  $n$  randomly generated parameter combinations, called individuals, and calculates the cost function for every individual. The inverse of this cost function is indicated as fitness function. Subsequently, a percentage of individuals with the worst cost function is deleted. The information contained in the remaining population is combined to create a new population. The general idea is that this population will contract to the global minimum by creating a new population by using a

percentage of the fittest individuals of the current population. Obviously, the initial population has to be large enough to cover the parameter space with a certain density to find the global minimum. Although these algorithms are able to search optima for very complex functions, they are usually very time-consuming. Therefore, it usually does not pay off to iterate completely to the global minimum: if a point close to the global optimum is found, a gradient based optimization algorithm can be applied to converge rapidly to the absolute minimum. This sequential approach is known as hybrid optimization [48]. Optimal convergence values for the genetic algorithm can be found in literature [36,5]. To increase the efficiency of the genetic algorithm further, a good initial population should be calculated as starting point. This implies:

- the population size should match the complexity of the problem,
- the number of generations has to be large enough in order to converge to the global minimum,
- the population has to be evenly distributed over the parameter space,
- all individuals have to be feasible (satisfy both linear and nonlinear constraints).

For this specific optimization formulation these points are empirically determined as:

- the population size is empirically determined to be 750-2000 individuals,
- a total number of 15 generations leads to a relatively good solution for the genetic algorithm,
- logarithmic scaling of the parameter vector is applied,
- each initial population member is checked on feasibility.

The main limitation with respect to the population size and number of generations is the calculation time. A population size of 1000 individuals and 15 generations typically leads to a qualitatively good solution with a calculation time less than one week. The logarithmic parameter scaling is an advantage in this case: controller design is typically a problem in which the improvement factor is much more important than the absolute bandwidth increase. This scaling means that, for the initial population, each decade in the parameter space contains the same number of individuals. For low bandwidth systems, it is easier to satisfy the constraints, therefore, the calculation time for the initial population decreases drastically. However, the initial population calculation shows that only 2-5 % of the parameter space is feasible, which shows the difficulty of this specific problem. For gradient based optimization procedures, parameter scaling has to be applied to improve the convergence rate. This scaling results in comparable magnitudes for all parameters. This is an advantage in the calculation of the direction derivative which is calculated to define the direction of the next iteration step.

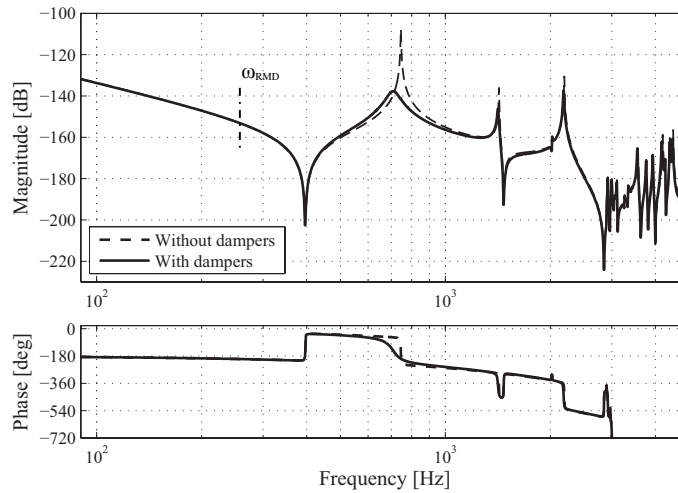


Figure 6.4: FRF of the undamped and damped plant in z-direction. The natural frequency of the dampers is indicated in the figure. Note that the RMD dynamics is not visible at this frequency.

### 6.5 Optimization results

As shown in the previous sections, a  $PID^+$  type controller is applied with an optional notch filter. In addition, the practical implementation enables to exclude the damper parameters from the optimization: in this case, a controller for the undamped stage is solved. This result is used to compare the performance increase for the results of the damped stage. Four different cases are optimized to obtain comparable results in terms of performance:

- Plant without dampers,  $PID^+$  controller,
- Plant with dampers,  $PID^+$  controller,
- Plant without dampers,  $PID^+$  controller with notch filter,
- Plant with dampers,  $PID^+$  controller with notch filter.

The first case results in a bandwidth of around 52 Hz. This value is used to set the upper and lower bounds for the RMD parameter values:

- the RMD mass  $m_{RMD}$  upper bound is set to 50 g,
- the RMD natural frequency  $\omega_{RMD}$  lower bound is set to 250 Hz,
- the RMD modal damping  $\zeta_{RMD}$  lower bound is set to 0.75.

These settings make that 1) the mass increase of the stage is limited, 2) the RMD is rigidly connected at the bandwidth frequency, which prevents energy dissipation in the dampers at this frequency, and 3) forces a robust damper solution instead of a very frequency specific notch behavior. The results of the optimization procedures are listed in Table 6.1. The plants corresponding to the first 2 solutions, with the  $PID^+$  controllers, are presented in Figure 6.4. This graph shows that the damping increase is mainly focused on the first resonance, which indicates that, in the undamped case, the bandwidth is mainly limited by the first resonance. A

Table 6.1: Optimization results listed for four different optimization cases.

| Closed-loop performance table                  |          |                |                     |                   |               |           |       |
|--|----------|----------------|---------------------|-------------------|---------------|-----------|-------|
|  | Plant    | $m_{RMD}$ [kg] | $\omega_{RMD}$ [Hz] | $\zeta_{RMD}$ [-] | $S_{LF}$ [dB] | $BW$ [Hz] | # DoF |
| <b>Controller: PID<sup>+</sup></b>             | Undamped | -              | -                   | -                 | -138,8        | 52,3      | 6     |
|  | Damped   | 0,03           | 250                 | 2,0               | -151,2        | 78,3      | 9     |
| <b>Controller: PID<sup>+</sup> &amp; notch</b> | Undamped | -              | -                   | -                 | -150,6        | 81,7      | 10    |
|  | Damped   | 0,04           | 250                 | 2.5               | -159,5        | 107,4     | 13    |

few observations can be made regarding the solution as presented in the second row of Table 6.1 – PID<sup>+</sup> controller with damped plant:

Although the algorithm had the freedom to place the RMD's natural frequency  $\omega_{RMD}$  around 740 Hz, at the resonance frequency, this parameter value is determined to be 250 Hz. This frequency  $\omega_{RMD}$  is indicated in the figure. This is the result of the lower bound of the RMD's modal damping value  $\zeta_{RMD}$ , which forces a robust solution. Within this robust parameter space this is the best solution in terms of performance increase. Note that this solution principle with a relatively low natural frequency and high modal damping, although for a simplified stage model and ideal dampers, is in accordance with the broad-banded damping results as presented in Chapter 2.

The resulting damper mass from the optimization amounts 30 g. This is substantially lower than the upper bound of 50 g which is applied during optimization. This indicates that increasing the damper mass too much, can result in decreasing natural frequencies and therefore a performance decrease. The algorithm deals with the tradeoff between the mass amounts of the detrimental mounting mass and the effective moving mass.

The behavior of the closed loop is visualized to validate if the complete set of constraints is satisfied. Figure 6.5a shows the Nyquist diagram of solutions 1 and 2 of Table 6.1. This figure shows that the modulus margin constraint is satisfied. Figure 6.5b shows the step responses and shows the faster response of the damped stage with respect to the undamped stage. In

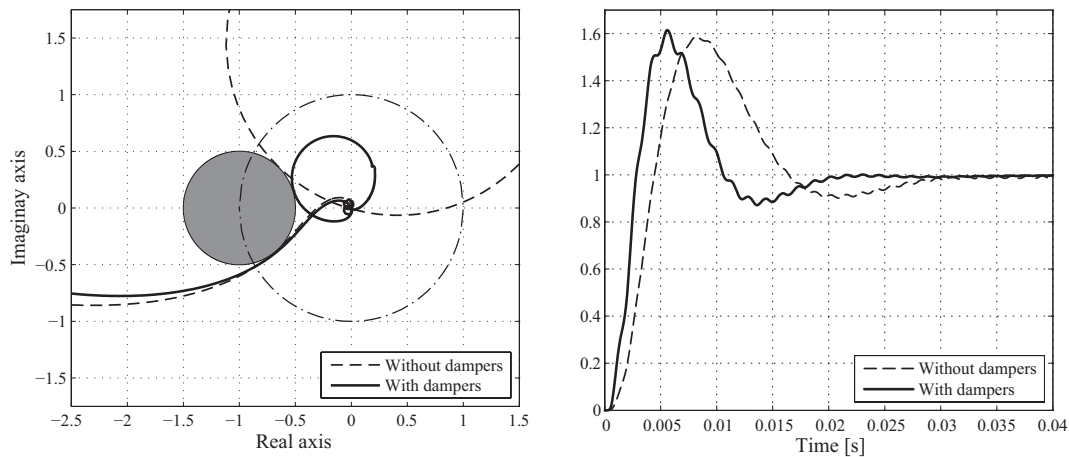


Figure 6.5: a) Nyquist diagram of the open-loops. b) Step responses for both solutions.

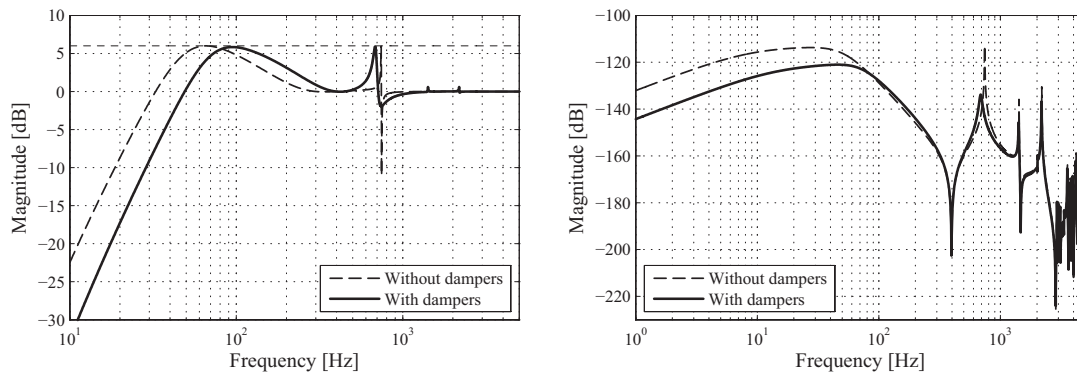


Figure 6.6: a) Sensitivity diagrams of the solutions with and without dampers. In the optimization without dampers, only the controller is optimized. In the case with dampers the dampers and the controller are optimized simultaneously. b) Process sensitivity diagrams of both solutions.

addition, stability is visualized by these responses.

Figure 6.6a presents the sensitivity plots of both systems as function of the frequency. This figure shows that the low-frequency suppression factor has increased for the damped system. This indicates that a higher controller gain is implemented. The right plot shows the process sensitivity, which is also better at low frequencies for the damped case.

## 6.6 Experimental validation in closed loop

The RMD parameters resulting from the second optimization, as listed in Table 6.1, are used to elaborate the mechanical design and provide experimental validation. This case is chosen because it shows the principle well. Upon the time the dampers were produced the stage was not ready to measure and, therefore, the correctness of the resonance frequencies was difficult to estimate. This uncertainty led to the decision to exclude the solution with the notch filter. Figure 6.7 presents a photograph of the RMDs, which are based on the parameter values as described in Table 6.1, solution 2 – Controller  $PID^+$  / Damped stage model.

### 6.6.1 Damper identification

Figure 6.8 presents the measured frequency response of the RMD with fluid applied. This measurement clearly shows a stiffness dominant part, indicated by the horizontal line and a

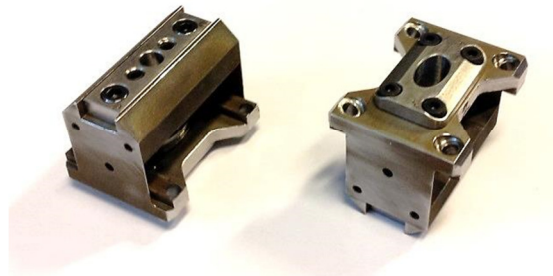


Figure 6.7: Photograph of the damper hardware after realization.

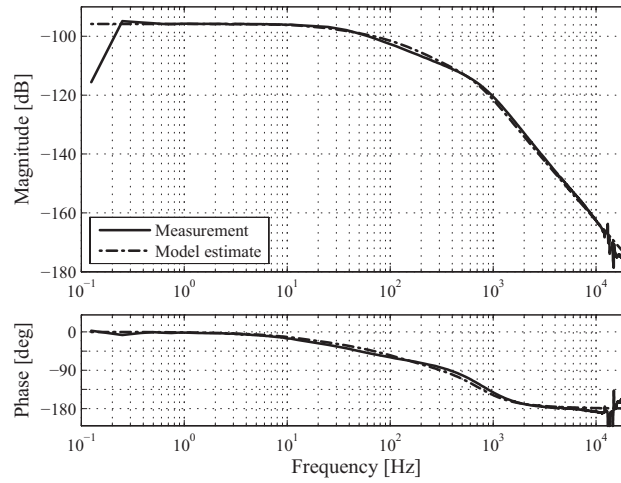


Figure 6.8: Frequency response functions of the damper. The solid line presents the measurements and the dashed line represents the model estimate.

damping dominant frequency range, with a negative slope up to 1000 Hz. Above this frequency the damper behavior is determined by a mass dominant line. The characteristics of the measured behavior match the model quite well.

This RMD is designed to influence the performance limiting resonance around 800 Hz. The measurement above shows that the damping force is mainly present between 50 and 1000 Hz. In this frequency range, the fluid is largely determined by the viscous behavior and, therefore, the linear viscoelastic behavior is less important than in the broad banded approach shown in Chapter 5, in which damping was added up to 4000 Hz.

The undamped motion stage and the damped one are identified in a closed-loop setting. The sensitivity and process sensitivity are measured and the plant behavior is calculated [71]. Figure 6.9 shows the resulting Bode diagrams of the undamped and damped plant. The damping increase at the umbrella mode, the first natural frequency visible in Figure 6.9, amounts approximately 15 times. The dynamics of the RMD is, due to the high damping values, not visible in the frequency response function despite the low natural frequency of 250 Hz.

### 6.6.2 Performance in $z$ -direction

The increased modal damping values enable to apply controllers with higher gains. Due to small differences between the plant model and the measurement, the model based controllers as listed in Table 6.1, are slightly adjusted, based on the measurements shown in Figure 6.9. This results in performance values as listed in Table 6.2. Figure 6.10a shows the open loop of the system with and without dampers, these graphs correspond to the upper two rows in Table 6.2. Figure 6.10b shows the Nyquist diagram of both systems. The increased damping on the first resonance is clearly visible in Figure 6.9 as well as in Figure 6.10a as reduced amplification factor and in Figure 6.10b as circle with a decreased circle diameter.



Table 6.2: Characteristic values for different closed-loop systems

|  | Plant    | $S_{LF}$ [dB] | $BW$ [Hz] | $\omega_{LP}$ [Hz] |
|--|----------|---------------|-----------|--------------------|
| <b>Controller: PID<sup>+</sup></b>             | Undamped | -140,3        | 50,1      | 275                |
|  | Damped   | -149,2        | 75,4      | 400                |
| <b>Controller: PID<sup>+</sup> &amp; notch</b> | Undamped | -150,1        | 77,8      | 600                |
|  | Damped   | -153,6        | 102,7     | 600                |

Figure 6.10a shows the following advantages for the damped stage:

- a bandwidth increase due to the larger proportional controller gain is visible in the amplitude difference between the two lines around the cross-over frequency. This proves the improved low-frequency sensitivity against position disturbances,
- the turnover frequency of the low-pass filter can be placed at higher frequencies for the damped stage. This phenomenon is well visible in the phase plot, which shows a larger phase lead for the damped case at frequencies above the bandwidth. The frequencies corresponding to the low pass filter  $\omega_{LP}$  are listed in the last column of Table 6.2,
- although the controller gain is larger in case of the damped plant, the diameter of the resonance is smaller in the Nyquist diagram, which clearly indicates the advantage with respect to robustness of the damped stage,
- the damping increase shows a decrease of the amplification factor and a broadening of the resonance peak. As a result, the damped resonance contains more frequency points than the undamped resonance. The result is clearly visible in Figure 6.10b in which a more accurate circle is described in case of the damped resonance.

The performances for the closed loops after controller implementation are comparable with

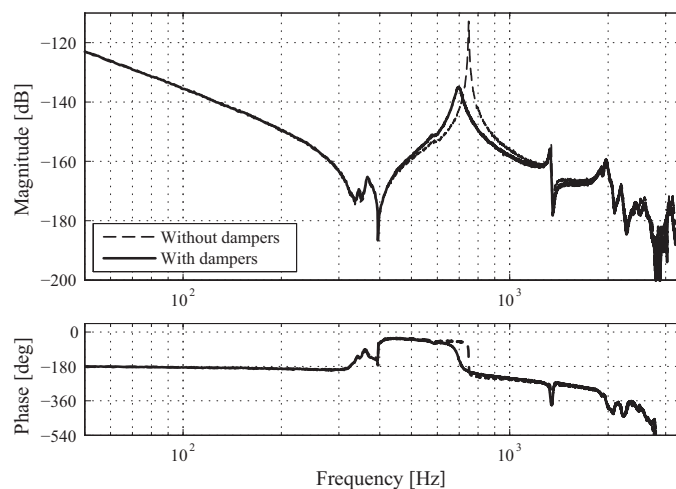


Figure 6.9: Measurements of the undamped and damped stage in z-direction.

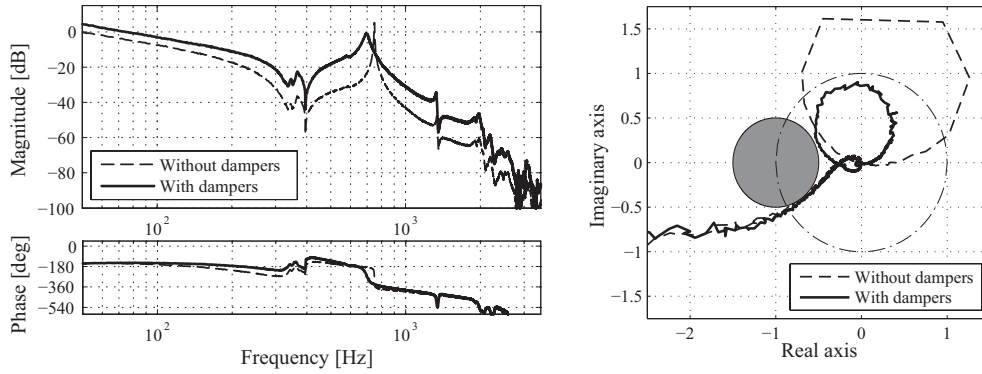


Figure 6.10: a) Measurements of the open-loop of the undamped and damped stage in z-direction. b) Nyquist diagram of both open-loops, which shows the stability margin of 6 dB and the first resonance frequency.

the ones resulting from the optimization procedure. See Table 6.1 and Table 6.2 for comparison. The differences in bandwidth and low-frequency sensitivity values between optimization and experiments are negligible.

Figure 6.11 shows graphs of the sensitivity and process sensitivity as function of the frequency. The sensitivity shows that the modulus margin of 6 dB is not violated. It in addition shows that the resonance at 740 Hz limits the controller gain: more gain results in exceeding the modulus margin of 6 dB at this frequency.

In addition, the process sensitivity shows an advantage of the principle to add damping to the stage. This advantage is due to the suppressed resonance amplifications in the plant. The process sensitivity is determined as the product of the sensitivity and the plant. Usually, as described in the analysis part of this chapter and Chapter 2, the low-frequency sensitivity is used as criterion for performance. Simultaneously, the modulus margin has to be satisfied to guarantee robustness. The low-frequency sensitivity, and therefore the bandwidth, can often easily be improved by adding a notch filter to the controller. To show the advantage of plant damping two principally different notch applications are explained briefly:

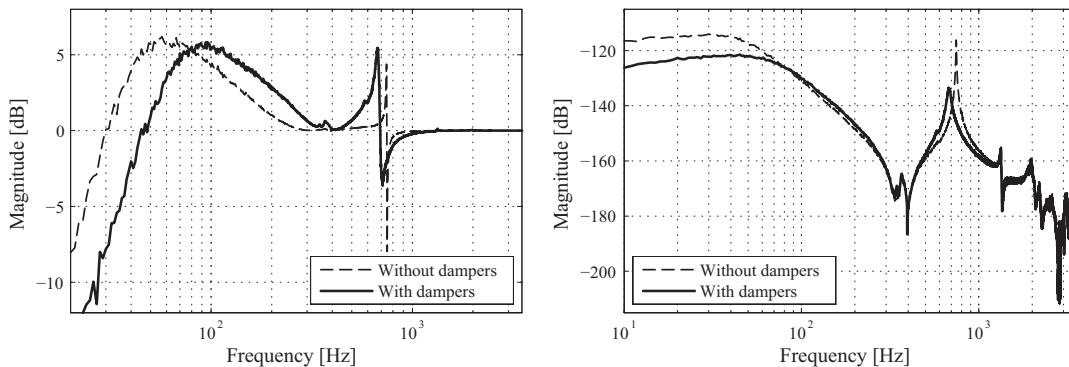


Figure 6.11: a) Measured sensitivity functions of the damped and the undamped stage. b) Process sensitivities for both cases.

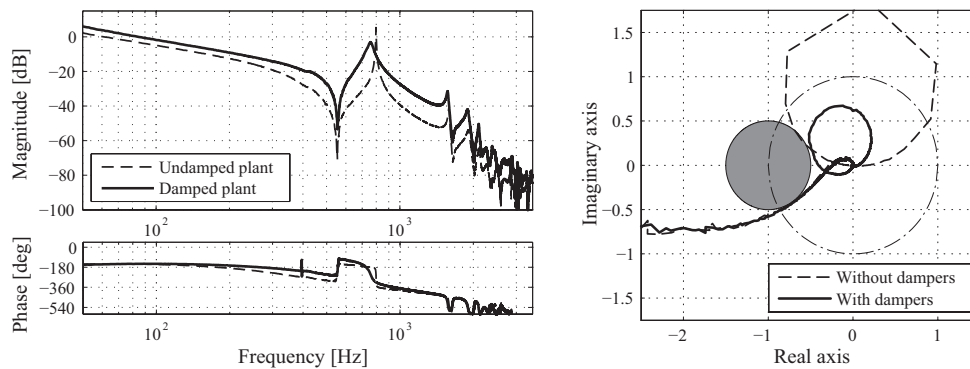


Figure 6.12: a) Open-loop Bode diagrams of the rotational direction ( $\varphi$ ) of the undamped and damped stage with  $PID^+$  controllers applied. b) Nyquist diagrams of both open-loops.

- resonance amplitude suppression. The frequencies of the poles and zeros are equal (pure notch). The result is an uncontrollable resonance due to a very low controller gain at the resonance's frequency: the sensitivity value at the resonance frequency decreases. Therefore, a higher proportional gain is applicable. However, the low-damped resonance still appears in the plant and therefore in the process sensitivity. This indicates that force disturbances at the resonance frequencies are effectively transmitted to the output,
- resonance phase rotation. This means that the pole and zero frequencies are not equal, which creates phase lead or lag in between the pole and zero frequencies. This application of a notch filter is known as skewed notch. If the additional phase is created at a resonance frequency, the resonance's circle is rotated in the Nyquist diagram and the closed-loop damping of the resonance is increased. Therefore, the resonances in the process sensitivity show substantially higher damping than the plant resonances. This introduced damping is due to the influenced sensitivity. Although this increased closed-loop damping is very useful, this way of applying notches is less robust against phase shifts and therefore not widely used in industry.

The advantages of both above solutions are combined in case of increasing the damping in the plant: pure notches can be applied on the resonances that limit the controller gain. The result of having uncontrollable resonances is compensated by the damping increase that has been realized in the plant instead of the controller.

Summarizing:

- Pure notch filters can be applied instead of skewed notches,
- The process sensitivity reduction at resonances – closed-loop damping – is obtained by adapting the plant behavior.

Table 6.3: Characteristic values for the closed-loop performance in rotational directions  $\varphi$  and  $\psi$ .

|                         | Plant    | $S_{LF}$ [dB] | BW [Hz] | $\omega_{LP}$ [Hz] |
|-------------------------|----------|---------------|---------|--------------------|
| <b>Controller: PID+</b> | Undamped | -144,9        | 61,1    | 375                |
|                         | Damped   | -153,0        | 84,5    | 625                |

### 6.6.3 Performance in rotational directions

In addition to the behavior in the decoupled z-direction, the dampers influence the plant behavior in the rotational directions around the  $x$ - and  $y$ -axes. These directions are indicated by  $\varphi$  and  $\psi$ , respectively. Although the performance in these directions is not included in the optimization section, it is elaborated to show the advantages in these directions too. Figure 6.12 shows the Bode diagram of the open loop and the Nyquist diagram for both systems. Table 6.3 lists the results of the closed-loop performances in rotational directions for a PID<sup>+</sup> controller. Note that the damping results in a higher frequency of the low pass filter, this effect already has been observed in the translational directions. This phenomenon is clearly visible in Figure 6.12a, in which the gain difference at 1000 Hz is much larger than at the bandwidth frequency around 75 Hz.

## 6.7 Advantageous side-effects of the RMDs

As shown, the dampers are designed to maximize the performance increase in the translational z-direction. In addition, the rotational directions benefit almost as much as the translational direction. As stated in Section 6.2, the torsion mode is not visible in the frequency response in z-direction due to the four actuators and sensors in this direction. However, a disturbance force acting on the stage close to the corners will excite this mode and the spatial performance of the stage will deteriorate. This behavior is not visible in the control loops in the rigid body motion directions and, therefore, it cannot be counteracted. The RMDs however, due to their mounting positions on the stage's corners, are able to add damping to this mode. This implies that if the torsion mode is excited, the amplitude will decrease very rapidly. This phenomenon is measured in the experimental setup for both the stage without dampers and with dampers added. A short pulse is applied to one of the actuators in z-direction which excites the torsion mode. The displacements at the corners in z-direction are measured to obtain a response over time and estimate the damping improvement. Figure 6.13 shows the measured time responses for the undamped and damped stage on the left side and shows the corresponding power spectra of the signals on the right.

In the left figures, the times are indicated in which the amplitude has decreased to 15 % of the initial amplitude. The response in case of the damped stage shows a 4.75 times faster amplitude decrease than in case of the undamped stage. The right figures show the frequency content and show the damping increase by a lower peak value around 400 Hz. This peak corresponds to the torsion mode. In addition, a frequency decrease is visible due to the mass increase of the torsion mode. Looking at higher frequencies, less sharp peaks appear, which indicates that a number of higher order modes have obtained a damping increase as well.

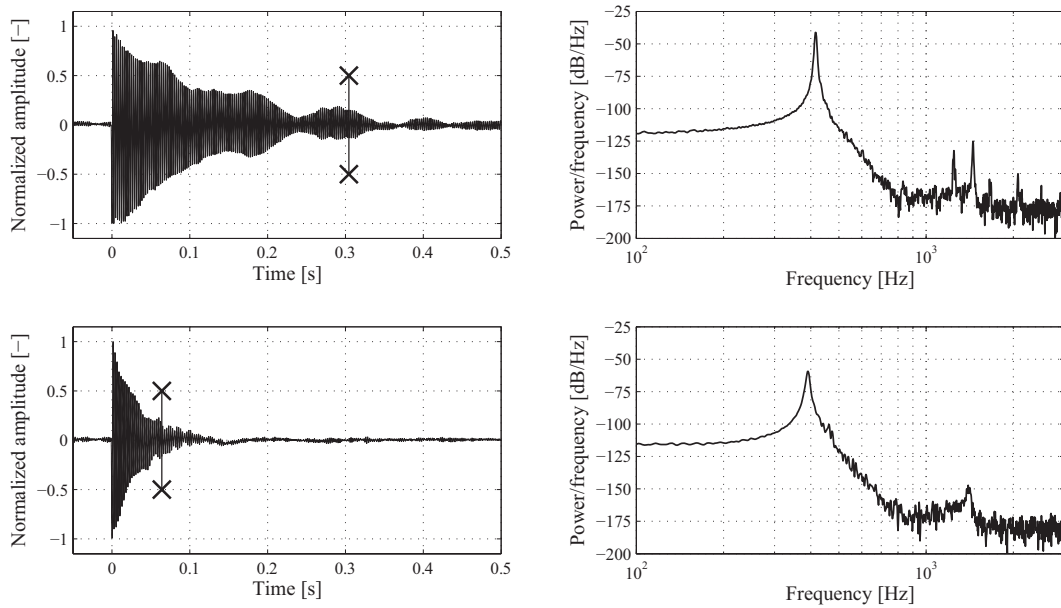


Figure 6.13: Impulse responses are shown in the left figures for both the undamped and damped motion stage. The settling time based on a 15 % remaining amplitude is indicated in the figures. The right figures show the power spectral densities of the responses in the left figures.

## 6.8 Concluding remarks

In this chapter closed-loop performance optimization is presented for full complexity motion stage designs. A sensitivity based performance criterion is defined as well as constraints for stability and robustness to solve the optimal parameters of the dampers and the controller simultaneously. A non-convex optimization algorithm, combined with a gradient based optimization algorithm is applied to solve this non-convex optimization problem in a limited amount of time.

This general problem formulation is applied to a motion stage design with 6 degrees of freedom to maximize the performance of the translational z-direction due to the modes that appear in this direction at relatively low frequencies. The practical design is fully elaborated and experimental validation is provided. In addition to the translational direction, two rotational directions benefit from the added damping and the performance increase in these directions is shown. As a third advantage, the damping increase of the torsion mode is shown. This mode is decoupled from the FRF in z-direction by a fourth actuator and sensor.

The optimization procedure shows:

- the hybrid optimization works well and provides useful design parameters,
- the closed-loop performance of complex stage designs can be optimized with the controllers included,
- the amount of performance improvement in z-direction is well estimated and amounts 50 % for a PID<sup>+</sup> controller in terms of bandwidth,

- the amount of performance improvement in case of a  $PID^+$  controller extended with a notch filter amounts 31 % in terms of bandwidth.

The results obtained by the experimental validation are:

- the sensitivity improvement in z-direction is 9 dB for low frequencies. This value corresponds to a bandwidth increase of 50 %,
- the sensitivity improvement in the rotational directions ( $\varphi$  and  $\psi$ ) is 3.5 dB. This value corresponds to a bandwidth increase of 32 %,
- the modal damping of the torsion mode is increased by over a factor 4.5,
- the total mass increase amounts 1.8 % for the 4 added complete RMDs, including the moving damper mass, the base mass and the damping unit.

## 6.9 Discussion

The successive modelling steps in FEM and state space combine the advantages of both modelling techniques: the FEM model allows for high complexity and efficient calculation of the corresponding undamped mode shapes. A modal state space model, although much smaller, contains the dynamic behavior without loss of information. The non-proportional damping introduction by local RMD mechanisms allows for dynamic couplings between the low-damped stage model and the heavily damped RMD models.

The hybrid optimization algorithm as applied proved to work well and provides design parameters for the RMDs which are used to design the dampers and validate the theory. The RMD's modal damping  $\zeta_{RMD}$  and natural frequency  $\omega_{RMD}$  are used in the parameter vector. Robust damper behavior is enforced by setting a lower bound for the modal damping parameter  $\zeta_{RMD}$ . The lower bound for the natural frequency  $\omega_{RMD}$  is set to 250 Hz in order to create rigidity at the bandwidth frequency. This lower bound estimate is based on the obtained bandwidth frequency in case of the undamped system. This approach contains a few drawbacks:

- it may lead to a  $GDF$  that is difficult to realize in case of a relatively high RMD natural frequency  $\omega_{RMD}$  and a large modal damping factor  $\zeta_{RMD}$ . This might result in a large  $GDF$  and, therefore, the RMD might not fit within the available space,
- the RMD's natural frequency lower bound is fixed. This implies, at least theoretically, that the bandwidth frequency is able to exceed  $\omega_{RMD}$ .

A more elegant approach is to create a dependency between the lower bound of the RMD's natural frequency and the bandwidth of the system. In addition, a maximal value for the  $GDF$  can be defined and implemented in the optimization criterion. These limits can be implemented in the algorithm by adding constraints. In addition, for practical cases, more criteria can be added. An example is a constraint on the process sensitivity in a certain frequency range in case of known force disturbances in this frequency range.

After optimization of the dampers and the  $PID^+$  controller, an optimal damper mass of 30 g was presented in Section 6.5, Table 6.1, although the upper bound was set to 50 g. This result is different than the results of Chapter 5, which stated that a larger damper mass is able to provide a larger suppression factor. This statement also holds for the system as presented in this chapter and is useful, however, an increasing RMD mass decreases the natural frequency of the resonance, which is detrimental for the performance. This shows the tradeoff between RMD mass contribution and the resonance suppression. This tradeoff basically proofs that an open-loop criterion will not be able to maximize the performance of the closed-loop system. Therefore, corresponding to the approaches in Chapter 5, it is useless to include the damper mass as a design parameter in the open-loop optimization, in contradiction to the closed-loop criterion in which the amount of mass is less trivial.

In the experimental setup, the first resonance (torsion mode) is decoupled from the rigid body loops and is therefore not visible in these rigid body loops. Therefore, if a control loop is closed for this decoupled mode, its closed-loop damping can be increased by a controller which mainly consists of a differentiator.

The experimental case as elaborated shows that the dampers mainly suppress the first resonance in the frequency response function in z-direction and thereby enable an increased controller gain. The resulting improvements show the maximum amount of performance increase with a simple fixed structure controller ( $PID^+$ ).

The solution of the optimization to suppress the first resonance is due to the 1) strong presence of this resonance in the frequency response function and 2) the limited controller complexity ( $PID^+$ ). Adding a notch filter in the optimization algorithm enables to suppress resonances in the open loop and generates more freedom for the algorithm to suppress the first resonance in the controller by means of the notch filter and applies the RMDs to suppress resonances at higher frequencies. In the optimizations as presented, the notch filter increases the bandwidth and creates more broadband damping, see Table 6.1. The modal damping increase with respect to the  $PID^+$  controller case shows this broad banded effect.

Different techniques exist to improve the performance of high-tech motion systems, as discussed above. The possibility to add RMDs is an additional technique to improve the closed-loop performance further. In general, seen from a control point of view, it is possible to divide the NRB resonances in different categories, which usually have their own frequency range:

- decoupled modes, which have their own control loop and can be influenced by a controller. These modes are usually the most low-frequency NRB modes of the system. These modes can respectively be:
  - damped by a differentiator without creating a bandwidth frequency,
  - stiffened by creating a bandwidth frequency by means of a proportional gain,
- non-decoupled notchable modes, which can be affected by a notch filter. These modes can be influenced by different notch filters:

- pure notches which suppress the modes and make them uncontrollable,
- skewed notches which introduce closed-loop damping,
- non-decoupled and non-notchable modes. These modes are usually located at relatively high frequencies and are usually suppressed by a low-pass filter. These modes can be adapted by the RMDs.

In addition, the modes as described above often benefit from the damping increase. The approach as described above mainly focusses at increase of the bandwidths of control loops.

In these control loops often not all modes are visible. This implies that the invisible modes can be excited by disturbance forces without being counteracted by a controller. Another approach with respect to RMD design, therefore, is to damp the resonances that are unobservable and/or uncontrollable by the motion control system and improve the spatial transient behavior over the motion stage's surface in this way. This approach will not result in bandwidth increases if these modes are not visible in the open loops, however, it will improve the performance.





# Conclusions and Recommendations

**Abstract:** The performance of motion stages has been improved by adding dampers to the stage at specific locations. The hardware is modelled, performance limits are indicated and performance increases have been investigated in a systematic way. This chapter summarizes the conclusions with respect to the results, grouped by different topics. Subsequently, the scope is widened and other applications are suggested that might benefit from the application of robust mass dampers. Finally, recommendations for further research are provided.

### 7.1 Concluding remarks

In this thesis, the opportunities to increase the performance of high-tech motion systems are investigated by increasing the modal damping of non-rigid body resonances by introducing robust mass dampers (RMD), which provides damping over a broad frequency band. A combination of techniques is applied to improve the performance of motion stages in a systematical way, including mechanical design, dynamic modeling, material characterization and optimization procedures. Theoretical improvement factors are calculated and experimental validation is provided to support the theory.

The main conclusions of the previous chapters are summarized and listed by subject.

#### **Robust Mass Dampers** (Chapter 2, 5, 6)

Robust mass dampers have proven to be able to provide broad banded damping. In addition, robust behavior is proven in case of parameter variations of both the motion stage and/or the parameters of the RMDs. This property explicitly underlines the suitability of RMDs to improve the behavior of motion stages that are operated in closed-loop conditions: parameter sensitive designs will result in a performance decrease and might eventually lead to destabilization of the closed-loop system.

The RMDs in this thesis are passive and stand-alone devices. Advantages of these types of devices are (1) the stabilizing behavior due to the principle of energy dissipation. (2) The stand-alone property implies that no connection between any structural part and the motion stage is created, and no signal or power cables are needed which prevents the introduction of disturbance forces. (3) The damper design by application of LVE behavior enables larger suppression factors than purely viscous fluid behavior, see Chapter 5 and Appendix C.

At least in case of motion stages with a relatively large length-height ratio it appears that an overall mass contribution by the RMDs of 2 % of the stage mass is sufficient to improve the stage performance in z-direction significantly. This is proven by experiments and is described in Chapter 5 and Chapter 6.

#### **Influence on stage dynamics** (Chapter 2, 3, 5, 6)

The relatively high modal damping of the RMDs prevents for visible effects in the rigid body mass line of the frequency response functions. In other directions, the natural frequencies of the RMDs can be designed above 6 kHz for dampers of 65 g. This is usually high enough to prevent for detrimental properties in the directions of motion.

#### **RMD locations** (Chapter 5)

The location of an RMD on the mechanical stage is a significant factor in the performance increase factor. The effectiveness of the RMD to improve the modal damping factor scales quadratically with the stage displacement at the damper location. Therefore, if the limiting

natural frequencies are determined, the locations with large displacements for the corresponding mode shapes have to be found. In case of more than one resonance this might be a weighted criterion for the different modes. This approach is applicable for both open-loop and closed-loop performance criteria.

### **The fluid model (Chapter 4)**

A linear viscoelastic fluid model is derived from measurements and applied in the optimization formulations of respectively Chapter 5 and Chapter 6. The results of these two chapters show that the model quality is good enough to predict the system's damped behavior quite accurately. Suggestions for an improved measurement setup are provided (Chapter 4), and an improved fluid model for Rocol Kilopoise 0868 is presented in Appendix B.

### **Open-loop modal damping improvement (Chapter 2, 5)**

The principle of broad banded damping is well applicable for practical cases: in the elaboration of Chapter 5 the intended damping range was 1-4 kHz. In addition, a damping increase is visible up to 6 kHz. This frequency range abundantly covers the range in which performance limiting flexibilities usually arise in motion stage designs. An optimization criterion in terms of resonance suppression is applied and works well: this criterion inherently only optimizes the visible resonances at the actuator and sensor location. The choice which resonances should be suppressed, therefore, is specified in the cost function by the frequency response function. Robustness of the solution and broad banded effect in practical cases is proven by the experimental validation. The calculated suppression factor compares well to the measured ones. The suppression factor amounts approximately 24 dB between 1 and 4 kHz, which indicates a modal damping increase factor of 16.

### **Iterative optimization approach (Chapter 3)**

This iterative approach as presented does not guarantee a globally optimal solution in terms of damper parameters. However, it is often useful to – at least once – execute this approach for a number of reasons:

- it creates insight in the bandwidth limiting dynamics of the open loop,
- the first iteration step provides, at least roughly, an estimate of the obtainable improvement factor: the largest progression is usually obtained in the first step,
- it is relatively easy to execute the iterations: only a loop has to be created which calculates the high-frequency sensitivity values instead of creating a closed-loop optimization criterion with constraints included,
- convergence is guaranteed during this approach. The worst solution possible for a single iteration step is that the improvement factor is zero: the optimization saturates.

**Closed-loop performance increase (Chapter 3, 6)**

The principle of closed-loop performance increase is formulated in an optimization formulation which accurately estimates the bandwidth improvement factor. The optimization formulation is non-convex, however, a hybrid optimization procedure is able to solve this specific problem in a limited amount of time. In addition to the improvements in the intended control loops, other control loops often benefit from the damping increase.

**Spatial improvements (Chapter 5, 6)**

In Chapter 6, the goal was to improve the controller gain of the control loop in z-direction. The torsion mode was excluded from this loop by geometrical decoupling. The experimental results showed that this mode's damping, as a side effect, was increased substantially.

**Advantages in analysis**

A more general observation regarding the analyses method is presented. The approach with separate RMDs is an efficient approach which contains two large advantages:

It enables to continue with the current applied mechanical design approach for high natural frequencies and increase the modal damping afterwards. This enables to still apply the materials with high specific stiffness and low damping.

In the analysis phase the advantages are enormous. 1) Undamped natural frequencies and mode shapes can be calculated and are valid for the low damped stage's mechanical design. These algorithms are very efficient and large models can be solved. 2) State space models can be created which contain the complexity of the FEM model and can be validated by calculating the responses by means of superposition of the undamped modes in the FEM software. 3) RMDs can be added at specific locations. This results in non-proportional damping and complex mode shapes, which are correctly calculated by the state space model. 4) This enables to apply optimization algorithms and compare different RMDs very quickly.

The complete model including dampers can be solved in FEM, however, this approach contains serious drawbacks. 1) The mode shapes change from real normal modes to complex modes due to the damping at specific locations. This implies that complex solvers have to be applied. These solvers are much more time consuming than the solvers for real natural modes. 2) The frequency response functions can be calculated using fully harmonic solvers. This results in the most accurate solution because the model is not truncated as in case of a state space model with a limited number of modes. However, this algorithm solves the complete model for every frequency point in the frequency response function and, therefore, this approach is extremely time-consuming. 3) Therefore, in this approach the ability to implement different RMD parameters and execute optimization algorithms practically vanishes due to the limitations listed above.

## 7.2 Possible RMD applications

Motion stages as discussed in this thesis usually show well defined natural frequencies with relatively low variations in frequency and modal damping. Small differences (over lifetime) might be visible due to wear and tear and small temperature variations. The resulting small differences in dynamic behavior can easily be caught in the robustness and broad banded effect of the RMDs.

More applications could benefit from the characteristics of the robust mass damper, in which a tuned mass damper is not applicable due to the frequency specific behavior or instead of a TMD in order to broaden the damping range. Suggestions for future application fields in which RMDs might be able to improve the behavior are:

- other precision motion systems,
- coordinate measuring machines with very fast and accurate motions. These machines are often comparable with the motion systems presented in this thesis in terms of low damping and force to position control,
- printers, these devices operate at different speeds,
- production equipment,
  - production machines such as milling machines, these machines operate with varying spindle overlengths which results in different natural frequencies. In addition, the disturbance forces are very large due to the milling process,
  - robots for assembly and production. Variations in natural frequencies arise in these machines due to different positions,
  - flat-bed laser cutting machines. These machines with a horizontal H-bridge structure show position dependent natural frequencies. In addition, temperature variations arise due to varying process output powers.
- structural engineering: slim and tall structures (skyscrapers, windmills) usually show one or two dominating natural frequencies and tuned mass dampers are common in this field to reduce corresponding amplitudes. An RMD can be applied in more dynamically complex structures that show ranges of resonances. Examples are bridges, mobile cranes, lattice structures, off-shore platforms, etc,
- aviation and space engineering,
  - in airplanes usually a broad vibration spectrum is present due to the engines, aerodynamics and vibrations from other aircraft systems,
  - space applications, (e.g. satellites etc.) are subject to large disturbance forces with a broad frequency content during take-off.

## 7.3 Recommendations

### 7.3.1 In general

Based on the different analyses and experiments as showed in this thesis, the following recommendations for future development can be given.

The analyses and experiments as conducted showed the advantages of RMDs on motion stages. However, the RMDs as presented are not able to increase the modal damping of all non-rigid body modes. Only the modes with translational movements at the damper locations can be influenced. The following recommendations can be stated to improve the stage behavior further:

Design of different RMDs for one motion stage in order to obtain different goals. For instance: 1) 4 RMDs to improve the bandwidth as shown in this thesis and 2) an additional number of RMDs to increase the damping of the remaining modes and thereby improve the spatial and transient behavior. These RMDs might be mounted at different locations and might have different moving masses, natural frequencies and modal damping. This enables to search for the optimal damper location to maximize the performance for both goals. A drawback is the mass increase of the motion stage.

Develop RMDs with more degrees of freedom. Appendix E shows an example of a damper with two degrees of freedom, a translational and a rotational one. Advantages are the increased efficiency due to benefits of the moving mass in more degrees of freedom. A drawback of the increasing number of degrees of freedom is the difficulty to design high natural frequencies in other directions.

The RMDs should be integrated in the stage design. This 1) reduces the mass contribution on the damper mounting side. In addition, 2) it may provide a more stiff connection between stage and RMD and therefore may result in higher natural frequencies. 3) RMD implementation in an early stage in the design process of the motion stage is necessary to have full freedom with respect to damper placement. The motivation for this recommendation is the dependency of the suppression on the displacements of the modes: if stage locations with large displacements are already used for other devices the dampers may become less effective.

A ‘Design for Damping’ strategy can be applied in order to improve the performance further. As stated above, stage locations with large displacements have to be found to mount the dampers to. This observation might lead to adaptation of the mechanical design in order to increase the damper efficiency. If stage features are built out (further), the resonance amplitudes can increase and therefore the ability to add damping to the modes.

Robust encapsulations should be created to prevent the RMDs from fluid loss. In addition to the loss of damping properties in case of a fluid run-out it will lead to tough contamination inside machines.

### **7.3.2 From control point of view**

The robustness properties of stages with RMDs should be investigated in detail and the implications for control theory should be elaborated. In case of a more robust plant behavior, the following results can be obtained: 1) Notch filters can be placed at resonances with higher frequencies. The improved plant robustness will cause less amplitude mismatch in case of parameter variations. 2) The modulus margin is a robustness margin and is set to a certain value to guarantee robustness of the closed-loop system. In case of increased plant robustness at high frequencies, the modulus margin value can be increased in the controller design phase. This enables, in addition to the improvements due to the resonance suppression, to increase the controller gain further. This effect is not elaborated upon in this thesis and therefore the extent to which this phenomenon can be utilized is a useful topic for further investigation.

### **7.3.3 Damping materials**

A linear viscoelastic fluid is applied in this thesis. Chapter 5 and Appendix C showed that the suppression factor depends on the mass ratio and the applied LVE material. This implies that better results can be obtained if fluids with better LVE characteristics are applied. Specific LVE fluid properties for specific frequency ranges can be selected. In order to obtain better fluids, possibly blending of existing fluids might be a good starting point.

A lower zero shear viscosity often leads to more purely viscous properties, with the LVE behavior at higher frequencies. These fluids might be used at high frequency ranges. However, the lower zero shear viscosity has to be compensated by the geometrical damping factor. In case of smaller gap widths, this leads to an increased sensitivity of the damping value with respect to production tolerances. The limits of the production techniques and tolerances during assembly have to be explored to improve the behavior further.





# Appendices

## Appendix A Modal damping models

Many models exist to describe linear damping in a dynamic model. Material damping is often better described by a structural damping model than by a viscous damping model. The viscous model creates a damping force with the amplitude proportional and the phase opposite to the velocity. Equation A1 shows the modal-3 form  $A$ -matrix for mode  $i$  of a dynamic system with modal damping  $\zeta$  included.

$$A_{mi} = \begin{bmatrix} 0 & 1 \\ -\omega_i^2 & -2\zeta_i\omega_i \end{bmatrix} \quad (A1)$$

The structural model introduces a force with the amplitude proportional to the displacement and the phase opposite to the velocity. Equation A2 shows the  $A$ -matrix for mode  $i$  of a dynamic system with the loss factor  $\eta$  included.

The stiffness and damping are both proportional to the displacement given their placement in the first column. The stiffness component is in phase with the displacement and the damping part is in phase with the velocity, due to the 90 deg shift induced by the complex unit  $j$ .

$$A_{mi} = \begin{bmatrix} 0 & 1 \\ -\omega_i^2(1 + \eta j) & 0 \end{bmatrix} \quad (A2)$$

For simplicity, however, the viscous damping model is often used to describe material damping. This approximation is valid because of the low damping present in stage designs and the low number of modes that have to be described. The state space models as presented in this thesis contain viscous damping with equal modal damping factors for all NRB modes. However, it is observed that the modal damping model should be adjusted to describe the dynamic behavior well for large frequency ranges. The measurements in Chapter 4 are investigated further to fit a better transfer function. Figure A1a shows the measurement and the fitted transfer function. As known from literature [3], proportional damping as well as constant modal damping are two linear damping models and are applied frequently in dynamic models. The proportional damping model for mode  $i$  at frequency  $\omega_i$  is shown in (A3).

$$\zeta_i = \frac{1}{2} \left( \frac{\alpha_1}{\omega_i} + \alpha_2 \omega_i \right) \quad (A3)$$

It contains a decreasing part and increasing part as function of frequency: a constant part is not present. The disadvantage of the proportional damping model is easy to see: if  $\alpha_1$  and  $\alpha_2$  are both non-zero and positive numbers, the modal damping increases for high frequencies due to  $\alpha_2$ . If  $\alpha_2$  is set to zero, the modal damping disappears for high frequencies. The two

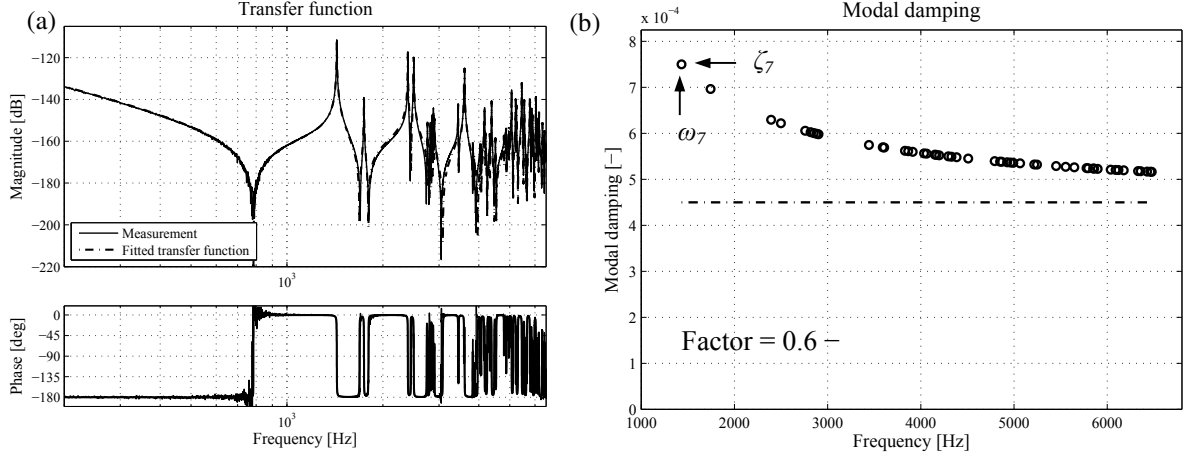


Figure A1a: A measurement and transfer function fit are shown in the left figure.

Figure A1b: The modal damping as function of the frequency. The factor describes the constant part of the modal damping. The frequency of the first circle is  $\omega_7$  and the corresponding damping is  $\zeta_7$ . The modal damping of this first resonance amounts 7.5e-4.

parameters indicate that, for a good choice of both parameters, the modal damping is only correct at two frequencies.

The constant modal damping model, if fitted on the first resonance's modal damping, seems to overestimate the high-frequency damping too. Therefore, another damping model is applied, which consists of a constant part and a part which is inversely proportional to the frequency. The model is shown in Equation A4, and uses the modal damping factor of the first NRB resonance  $\omega_7$  as input: resonance number 7 is the first NRB resonance in a motion stage. The factor  $f_c$  describes the constant part of the modal damping of the first resonance. This results in the constant model if the factor is set to 1, and if the factor is set to 0 it results in the proportional damping model with  $\alpha_2 = 0$ . For  $f_c > 0$ , this is a non-proportional damping model.

$$\zeta_i = \zeta_7 \left( (1 - f_c) \frac{\omega_7}{\omega_i} + f_c \right) \quad (A4)$$

Figure A1a shows a model fit on measurement data with 51 modes: 1 rigid body (RGB) mode and 50 NRB modes. The resonance frequencies are used to create the  $A$ -matrix. The  $B$ - and  $C$ -matrices contain the modal amplification factors and a constant value is included in the  $D$ -matrix to compensate for model truncation. This shifts the transfer function zeros and therefore the gain in the  $D$ -matrix can be determined based on the locations of the zeros. The damping value of the first resonance is determined and subsequently the factor  $f_c$  is adjusted to obtain a good model fit. A good result for this model is obtained with a factor  $f_c$  of 0.6. The model damping values corresponding to this factor are shown in Figure A1b.

The dash-dotted line shows the constant part and on top the part is shown which decreases by  $1/\text{frequency}$  is visible. The modal damping value for the first resonances appears to be  $7.5e-4$ . This approach gives quite a good estimate of the modal damping and corresponding amplifications at the resonance frequencies.

## Appendix B Improved LVE Rocol fluid model

Chapter 5 showed an RMD design for a motion stage based on a 3-mode Maxwell fluid model of Rocol Kilopoise. The RMDs are characterized and compared with the model behavior. In the frequency region between 2 and 4 kHz, the RMD model showed an overestimation of the damping with respect to the measurement. This mismatch is mainly due to an overestimation of the damping in the LVE fluid model. The derivation of the fluid model and the resulting 3-mode Maxwell model are described in Chapter 4. To obtain a more accurate fluid model, the procedure as described in Chapter 4 is applied on RMD measurements as presented in Chapter 5. The resulting fluid model is compared with the fluid model described in Chapter 4.

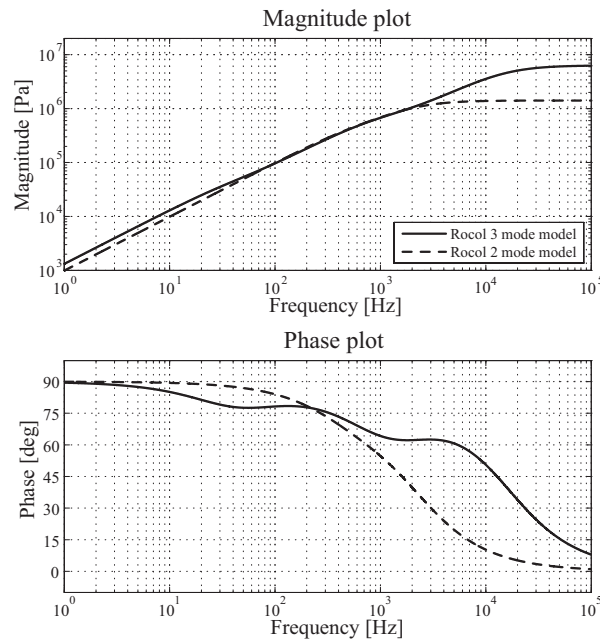


Figure B1: Magnitude and phase plot of the two Maxwell models of the Rocol Kilopoise 0868 VLE fluid.

Table B1: 3 mode fluid model and 2 mode fluid model parameters.

| First model 3 mode   | M#1    | M#2    | M#3    | Unit |
|----------------------|--------|--------|--------|------|
| $G$                  | 1.55e4 | 4.41e5 | 5.87e6 | Pa   |
| $\eta$               | 66.3   | 81.1   | 62.3   | Pas  |
| $f_0$                | 37.3   | 864.6  | 1.50e4 | Hz   |
| Zero Shear Viscosity |        |        | 209.7  | Pas  |

| Second model 2 mode  | M#1    | M#2    | Unit |
|----------------------|--------|--------|------|
| $G$                  | 2.10e5 | 1.20e6 | Pa   |
| $\eta$               | 63,7   | 93,5   | Pas  |
| $f_0$                | 524.7  | 2042.6 | Hz   |
| Zero Shear Viscosity |        | 157,2  | Pas  |

#### A-B1 Improved Rocol model

An optimization procedure is applied to minimize the error between the model behavior and the RMD measurement as shown in Chapter 5, Figure 5.24. The resulting fluid model is shown in Figure B1. The first 3 mode model of Chapter 4 is plotted for comparison. Table B1 lists the parameter values of the fluid modes of both models. The fluid in both cases is Rocol Kilopoise 0868. The first fluid model was described by three modes: the second model contains two fluid modes. The phase of the second fluid model crosses 45 deg at 2 kHz, instead of 13 kHz for the first model. This indicates that the damping of the 2 mode model above 1000 Hz is lower than that of the 3-mode model. The specific frequencies as listed in Table B1 show that the first model contains a mode with a turnover frequency around 15 kHz which induces the high-frequency damping overestimate. The second fluid model's highest turnover frequency is around 2 kHz, which explains the sharp phase decrease around 2 kHz. The zero shear viscosity of the second model amounts 157.2 Pas: this value is 28.5 % lower than specified by the manufacturer. The first fluid model showed a ZSV of 209.7 Pas, which is 4.7 % less than specified.

#### A-B2 Stage damped transfer function with new fluid model

The damped transfer functions of the complex stage design as investigated in Chapter 4 are calculated with both fluid models to compare their quality in more detail. Figure B2 shows the undamped frequency response as well as the frequency responses with the 3-mode and 2-mode fluid model. The measurements showed the modal damping of the first mode to be  $7.5e-4$ . This damping value is applied in the stage model to make the results more comparable to the measurement. The natural frequency and geometrical damping factor of 1270 Hz and 14.33 m respectively, are applied as in Chapter 4.4. Figure B3 shows the Bode diagram of the measurements as presented in Chapter 4, Figure 4.30. The mode numbers are indicated in both figures to enable comparison. The non-rigid body resonances within the cost function range (1-4 kHz) are listed in Table B2 with their suppression factors.

In addition to the suppression factors, some other observations can be done regarding the resonance shapes in the Bode diagram and the frequency shifts of the resonances:

- Mode #7 shows equal natural frequencies for both damped models, which are both lower than the undamped resonance frequency.
- Mode #9/10/11 show a continuous line in the measurement in which the separate resonances are barely visible. This behavior is better estimated by the second – 2-

Table B2: Suppression factors for the resonances within the frequency range of the cost function.

| Mode number    | Measurement | First model<br>3 mode | Second model<br>2 mode | Unit |
|----------------|-------------|-----------------------|------------------------|------|
| Mode # 7       | -24,3       | -26,1                 | -24,8                  | dB   |
| Mode # 9/10/11 | -38,7       | -30,9                 | -35,9                  | dB   |
| Mode 13        | -26,6       | -28,2                 | -26,9                  | dB   |

mode – fluid model than by the first fluid model.

- Calculated with the 3-mode model, the natural frequency of mode # 13 is lower than for the undamped model behavior. The transfer function calculated by the 2-mode model, however, shows a higher damped frequency than undamped frequency. This

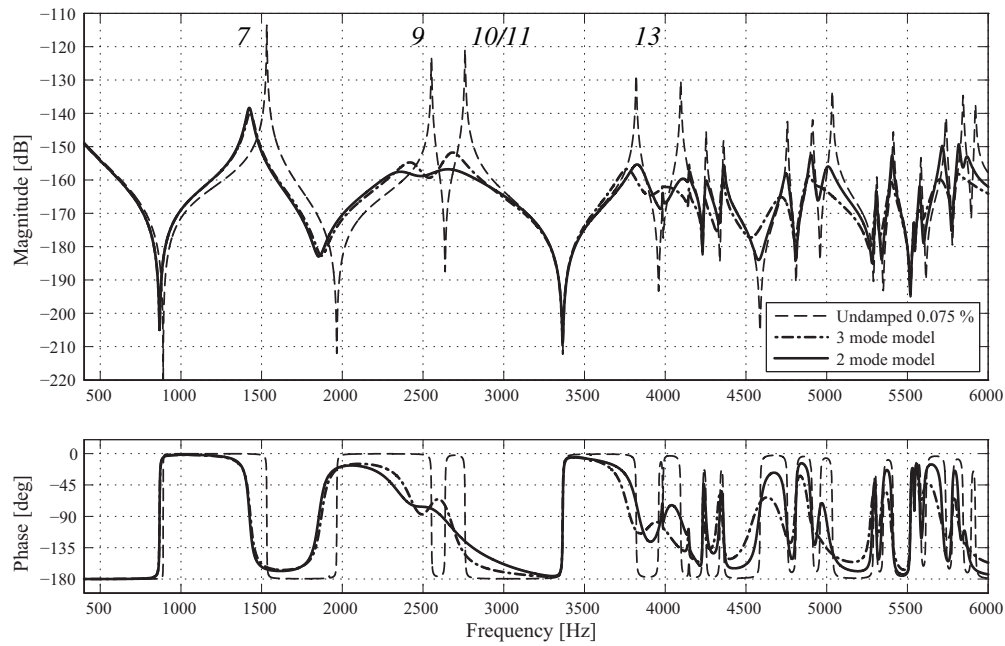


Figure B2: Collocated frequency responses at the stage corners. The dotted line shows the undamped frequency response with a modal damping of  $7.5 \times 10^{-4}$ . The other two frequency responses are calculated with the two fluid models.

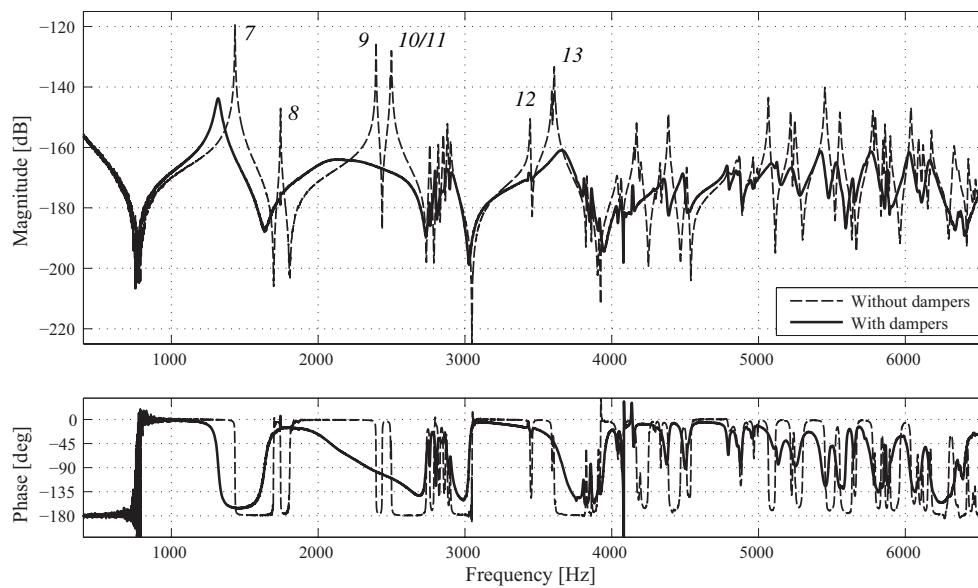


Figure B3: This figure is equal to Figure 5.24, and presented here again to facilitate comparison. This figure shows the transfer function measurements of the undamped and the damped stage.



positive shift is in correspondence with the measured frequency shift.

- At frequencies above 5.5 kHz, the damping of the 3-mode model slightly overestimates the damping. The second fluid model however, underestimates the damping at those frequencies.
- The second fluid model performs better than the first fluid model, especially within the frequency range of interest. However, for frequencies above 5 kHz the damping estimate is a little too low. The 2-mode fluid model can be improved further by adding a third fluid mode with a time constant between 5 and 7 kHz, which slightly increases the phase, and therefore the damping, of the fluid model between 5 and 10 kHz.

## Appendix C Linear viscoelastic damping materials

### A-C1 LVE Fluids and solids

Chapter 5 described an approach to increase the modal damping of a motion stage over a specified frequency range. In that chapter, the explanation is based on a linear viscoelastic fluid, which introduces practical difficulties. Another solution is adding damping by rubber-like materials which show LVE behavior too. A principal difference between fluids and solids is: elastic solids show stress based on the applied strain, where viscous fluids show stress based on the induced strain rate.

LVE materials, both solids and fluids, can be modelled by the multi-mode Maxwell model. A single mode in this model, existing of a spring and damper, describes viscous behavior at low frequencies, which changes in elastic behavior for high frequencies. The transition frequency between viscous and elastic behavior is indicated as characteristic frequency for that specific Maxwell mode. The phase is 90 deg for low frequencies and 0 deg for high frequencies. The 45 deg phase crossing is located at the characteristic frequency for that Maxwell mode.

An LVE fluid shows viscous behavior for low frequencies, LVE behavior in the intermediate frequencies and elastic behavior in the high frequency range. The characteristic frequencies of a multi-mode Maxwell model for a fluid are located within the LVE frequency range. The difference between the model for an LVE fluid and an LVE solid is the presence of low-frequency modes for the solid, with one zero-frequency mode to model the steady state elastic behavior. This mode is not present in a fluid model, which shows steady state viscous behavior.

For a flexure based RMD design, these differences in material properties result in (1) a worse decoupling between stiffness and damping for LVE solids with respect to fluids: the stiffness of LVE material contributes significantly to the RMD stiffness. This contribution is compensated by a decrease in flexure stiffness to maintain the optimal natural frequency. As a result, it will be more difficult to design high natural frequencies in other directions. An additional drawback of LVE solids is that (2) they usually contain modes with relative low characteristic frequencies with respect to fluids, which do not contribute to the performance within the frequency range in which the damping of the motion stage has to be increased. However, these modes contribute to the time response of the dampers.

To quantify the two statements above, examples are given for four different LVE materials. Three of these examples are LVE fluids with different material properties and the fourth is a rubber material. The rubber and one fluid model are based on real materials. The other two fluid models are created for comparison reasons and do not describe the behavior of an existing material. These four materials are compared to show their different influences with respect to motion stage damping. The four materials are:

- A viscous fluid up to 100 kHz: a single mode fluid model is used which shows purely viscous behavior up to 10 kHz. The time constant of the fluid mode equals 1e6 Hz and the ZSV amounts 220 Pas.

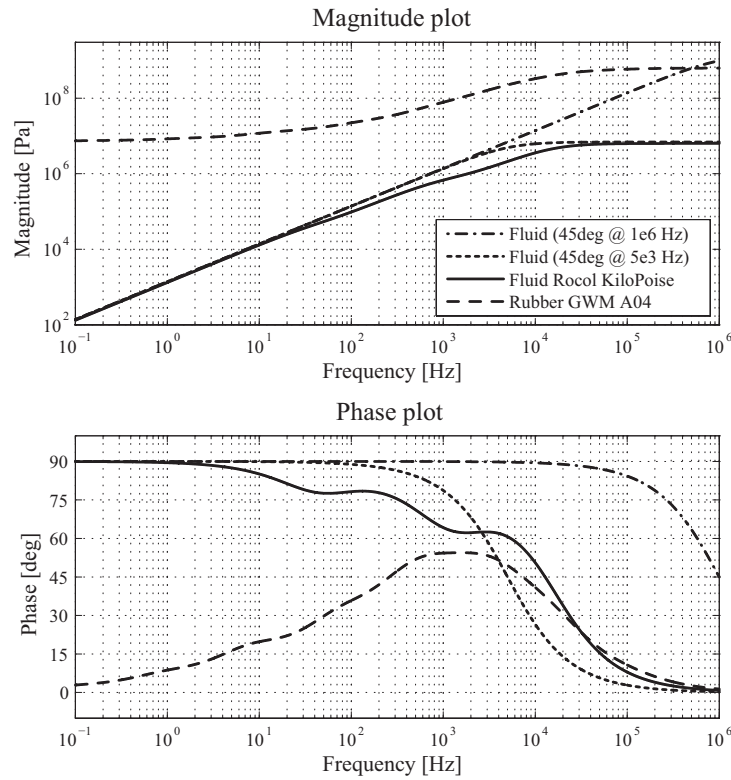


Figure C1: Magnitude and phase plot of the different LVE materials.

- an LVE fluid with the characteristic frequency at 5 kHz: this fluid model contains 1 Maxwell element and crosses the 45 deg phase at 5 kHz. The ZSV of this fluid is 220 Pas.
- the Rocol Kilopoise 3-mode model: this is a realistic fluid model as applied in chapter 4 and 5. The ZSV of this fluid is 220 Pas.
- an industrial rubber type (GWM-A04): this material shows LVE behavior in the frequency range of interest for motion stage damping (1-4 kHz).

All fluids have a ZSV of 220 Pas to make the fluids more comparable. The magnitude and phase of these materials are presented in Figure C1.

#### A-C2 Frequency dependent behavior

To show the differences between the materials, different optimizations are executed on the complex stage design as investigated in Chapter 4. Optimal damper parameters – natural frequencies and geometrical damping factor (see chapter 3 & 4) – for the different materials are sought after. The results are listed in Table C1. The RMD masses are 65 g for all results listed and the damper locations are equal. The algorithms are as the one applied in Chapter 5, which is a hybrid optimization algorithm. Two cases are studied:

The small banded optimization: the cost function is defined between 1 and 2 kHz. This suppresses the first resonance and the resulting parameter values show typical TMD behavior. See Chapter 5, Section 5.3.3.

The broad banded optimization: the cost function is defined between 1 and 4 kHz. This suppresses a broad range of resonances and the resulting parameter values show typical RMD behavior. See Chapter 5, Section 5.3.4.

First the results of the small banded optimization are explained: the suppression factor for the three fluids is comparable. This is roughly 40 dB. Looking top-down in Table C1, the TMD natural frequency is decreasing and the geometrical damping factor is increasing. Fluid 1 does not perform the best, although it contains perfectly viscous damping up to 10 kHz. The difference is only 0.34 dB in this case, which is senseless for practical use. However, the effect is visible in the simulation results and a property of the fluid. Figure C1 shows that the phase at 1500 Hz – the resonance frequency – is decreasing for the different fluids: fluid 1 = 90 deg, fluid 2 = 75 deg and fluid 3 (Rocol) shows about 60 deg. This decrease in damping is compensated by larger geometrical damping factors: respectively 0.81, 0.85 and 2.10 m.

The introduced fluid stiffness from the larger geometrical damping factors is compensated by a decreased optimal stiffness for the leaf springs, visible as a lower natural frequency, 1391, 1326 and 1270 Hz, respectively. The rubber shows a lower suppression factor combined with a very low natural frequency. The geometrical damping factor is lower than for the fluids. The reason is visible in the magnitude plot of Figure C1, which shows values over an order larger than for the fluids. The optimal geometrical damping factor therefore is more than a magnitude smaller than for the fluids. The problem of this specific rubber material is the high stiffness-damping-ratio, which is too high for optimal resonance suppression. A larger geometrical damping factor introduces more damping. However, it increases the stiffness too, and therefore the natural frequency. A rubber material with this phase characteristic and a lower zero frequency stiffness would have performed much better in this case.

Table C1: Suppression factors for the resonances for the small banded case (cost function between 1 and 2 kHz) and the broad banded case (cost function between 1 and 4 kHz). The damper mass is 65 g for all results listed.

| <b>Small banded optimization</b> | <b>Suppr. [dB]</b> | <b>Nat. Fr. [Hz]</b> | <b>GDF [m]</b> |
|----------------------------------|--------------------|----------------------|----------------|
| Fluid (45 deg @ 1e6 Hz)          | -39,41             | 1391                 | 0,81           |
| Fluid (45 deg @ 5e3 Hz)          | -39,75             | 1326                 | 0,85           |
| Rocol KP 3 mode model            | -39,62             | 1270                 | 2,10           |
| Rubber                           | -30,96             | 10                   | 0,054          |
| <b>Broad banded optimization</b> | <b>Suppr. [dB]</b> | <b>Nat. Fr. [Hz]</b> | <b>GDF [m]</b> |
| Fluid (45 deg @ 1e6 Hz)          | -22,76             | 2136                 | 4,87           |
| Fluid (45 deg @ 5e3 Hz)          | -24,81             | 1437                 | 5,54           |
| Rocol KP - 3 mode model          | -23,66             | 1271                 | 14,32          |
| Rubber                           | -24,02             | 0                    | 0,144          |

The comparable suppression factors in case of the broad banded optimization results show that all four materials perform well within this frequency range (1-4 kHz). However, small differences are present. The first fluid obtains the worst suppression value, although it shows a phase of 90 deg over the cost function frequency range. This is in comparison with the small banded suppression results. The other two fluids are performing better. Looking top-down in Table C1, the geometrical damping factor increases for the fluids, and the natural frequency decreases, as for the small banded case. The fluid with 45 deg phase at 5 kHz performs best again. In this case the rubber performs well in terms of suppression factor. However, because of the relatively high rubber stiffness, the flexure based natural frequency is very low again. This results in a difficulty to obtain high parasitic natural frequencies in the mechanical RMD design phase.

### A-C3 Suppression as function of damper mass

Figure C2 shows the maximal suppression factor, the natural frequency and the geometrical damping factor as function of the damper mass for the broad banded case, as shown in Table C1. These plots are the result of 50 optimizations for each LVE material. The right figures are details of the left figures and show the damper mass of 65 g indicated by the dashed line. The upper left figure shows straight lines as function of the damper mass. The lines do not intersect which clearly shows that the maximum obtainable suppression factor for a certain RMD mass and damping range solely depends on the LVE fluid characteristics: the fluid that performs best with a certain damper mass is the best fluid for other damper masses too. These

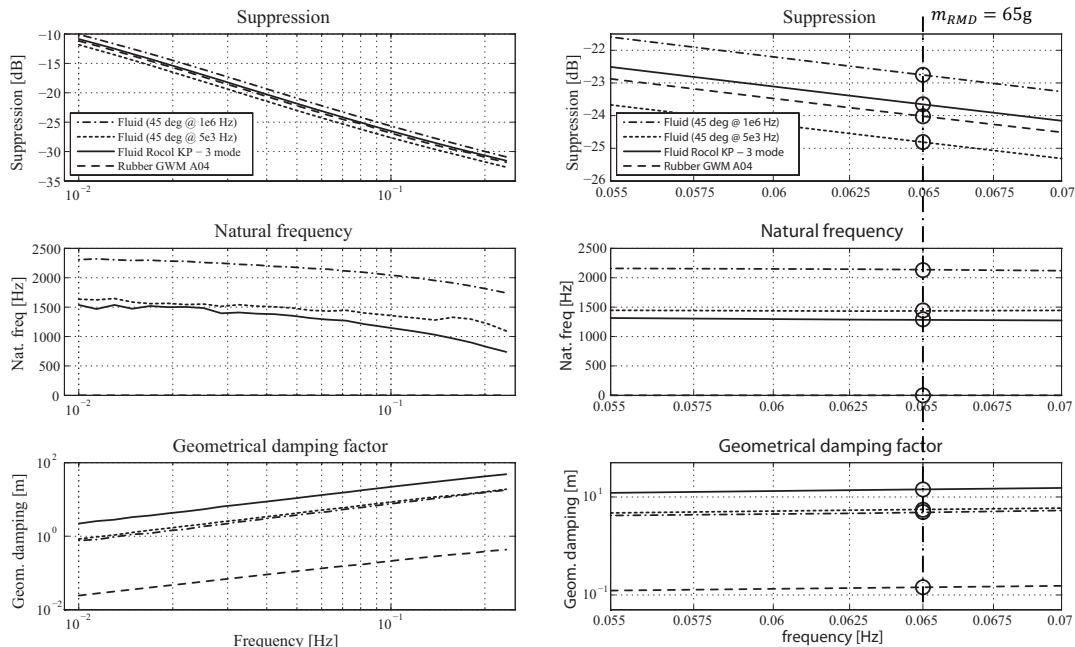


Figure C2: Maximal suppression value as function of the damper mass for the 4 materials presented above. The left figures shows a mass range from 10 g to 250 g and the right figures show a detail plot with 65 g damper mass indicated.

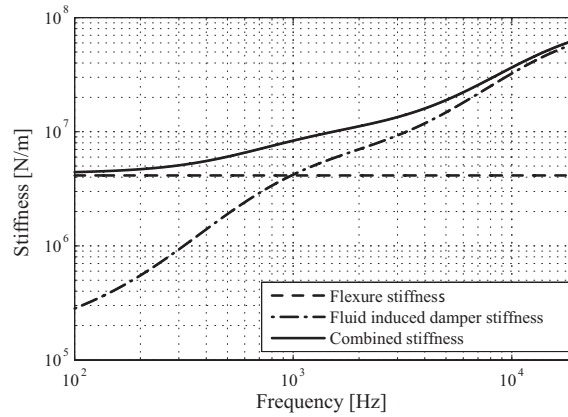


Figure C3: Stiffness as function of the frequency. The flexure stiffness is constant.

graphs show that 1) pure viscous damping (Fluid 45 deg @ 1e6 Hz) does not provide optimal suppression. This holds for both the small banded case and the broad banded case, see Table C1, and 2) the broader the frequency range is specified, the larger the advantage of LVE behavior with respect to viscous behavior will be. The mechanism behind these results is explained in the next section.

#### A-C4 Frequency dependent natural frequency

To explain the advantage of an LVE material with respect to a purely viscous material, the RMD design of Chapter 4 is used. The corresponding values are also presented in Table C1, Broad banded optimization, Rocol KP 3 mode model. The damper mass of 65 g combined with the leaf spring stiffness results in an undamped natural frequency of 1270 Hz, with a theoretical stiffness of 4.13e6 N/m. This value is constant as function of frequency and shown in Figure C3 as Flexure stiffness. The complex fluid damper response shows an in-phase component with the displacement. This phenomenon arises due to higher order dynamic behavior of the multi-mode Maxwell fluid model and can be seen as a ‘frequency dependent stiffness’: each Maxwell mode contributes to the stiffness in a specific frequency range. This frequency dependent stiffness is shown in the Figure C3 as fluid induced damper stiffness. A combined stiffness as function of frequency can be calculated by taking the sum of the flexure stiffness and the fluid damper stiffness, which is shown by the continuous line. This frequency dependent stiffness enables to calculate a frequency dependent natural frequency of the RMD. Figure C4 shows the RMD natural frequency-frequency ratio for the flexure stiffness and the combined stiffness: the natural frequency curves are divided by the frequency on the horizontal-axis, which indicates that the actual natural frequency can be found at the 1 crossing. The natural frequency for the flexure stiffness is 1270 Hz as shown by the 1 crossing.

The natural frequency for the combined stiffness is approximately 2100 Hz. The frequency range in which the modal stage damping has to be increased is indicated by the thicker line. A more horizontal slope contributes to the effectiveness of the damper. This explains the smaller advantage in case of the small banded optimization: the change in natural frequency is smaller

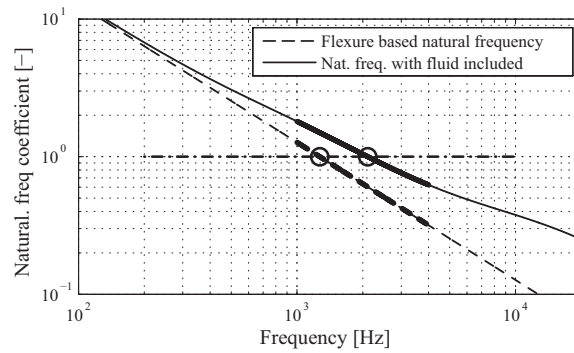


Figure C4: Natural frequency coefficient as function of frequency. The circles indicate the static natural frequency and the actual natural frequency.

over the frequency range of interest. For comparison: Table C1, broad banded optimization, Fluid (45 deg @ 1e6 Hz) shows a natural frequency of 2136 Hz for a fully viscous fluid. This natural frequency is roughly in the middle of the cost function range. This already indicates that this fluid does not benefit from LVE stiffness (see the lower suppression factor).

#### A-C5 Time domain results

Table C1 shows optimal RMD parameters for four TMDs with different LVE materials. The dynamic models of these RMD's and step responses are calculated to show another important difference between LVE solids and fluids. Figure C5 shows normalized step responses for the four RMDs. The upper figure shows the response on a linear time scale and the lower one on a logarithmic time scale. The upper figure clearly displays the difference in behavior between the four RMDs. The damper with the viscous fluid (45 deg at 1 MHz) shows the quickest response. This mechanism has the highest stiffness and the fluid has short time constants. The

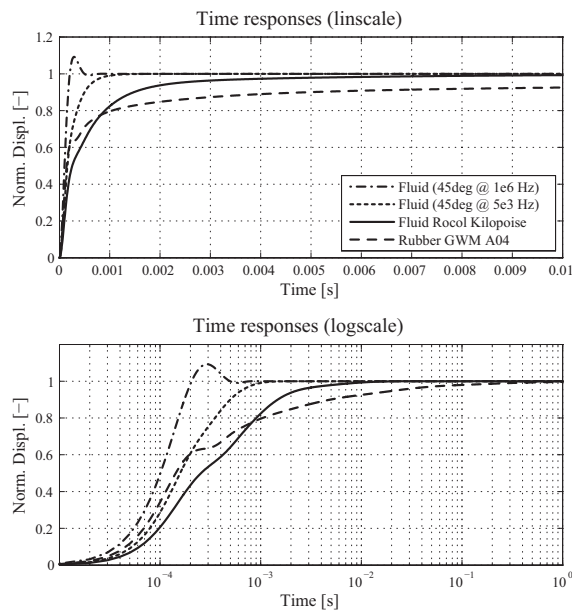


Figure C5: Normalized step responses of the different RMD designs.

RMD with optimal fluid for suppression (45 deg at 5 kHz) also shows a fast response. The lower time constant is visible in the slower response with respect to the viscous fluid. The RMD with the Rocol model applied shows a slower response than the first two. The RMD with rubber applied however, shows a much slower response. The initial response is relatively good. However, the low-frequency LVE modes cause a step response with a very slow component. Finally the step response converges to 1 as in case of the other fluids, see the lower plot of Figure C5. Note that the performance of these dampers on the motion stage is comparable in the frequency range between 1 and 4 kHz.

#### **A-C6 Conclusions**

For damping over a specified frequency range with RMDs, although counterintuitive, linear viscoelastic damping behavior enables better performance i.e. larger suppression factors than purely viscous damping behavior. This effect is introduced by the in-phase part of the behavior of the fluid, which can be interpreted as a frequency dependent stiffness of the linear viscoelastic material. The amount of performance improvement of an LVE material with respect to a purely viscous fluid is determined by:

- the LVE material properties,
- the frequency range.

The improvement factor is independent of the damper mass. The advantage is visible in both the design of TMDs and RMDs but is more utilizable in case of broad banded damper design.

Although rubber materials work as well as fluid damping for HF resonance damping, they show low-frequency Maxwell modes, which are visible in the transient responses.



## Appendix D Thermal effects

The principle of damping is based on energy dissipation, which implies that kinetic energy is transformed into thermal energy. The corresponding temperature increase during operation affects the damping constant and therefore the performance of the RMDs. This appendix briefly presents an estimate of the temperature increase of the damper during operation. The following assumptions are made:

- the zero shear viscosity of the fluid is used in the damping value,
- a sinusoidal displacement profile is assumed between the RMD and the stage,
- the dissipation is calculated for one frequency,
- the displacement amplitude is estimated.

Given the above assumptions, the displacement of the RMD with respect to the stage as function of time is described by:

$$x(t) = x_0 \cos(\omega t) \quad (D1)$$

in which  $x_0$  describes the displacement amplitude. The power dissipation as function of time for a viscous damper is described by:

$$P(t) = dx_0^2 \omega^2 \sin(\omega t) \quad (D2)$$

with  $d$  representing the damping constant in Ns/m. Over time, this leads to an averaged power dissipation of:

$$P_{AVG} = \frac{dx_0^2 \omega^2}{2} \quad (D3)$$

The calculations are elaborated upon for the one degree of freedom setup which is used to characterize the fluid behavior and is described in Chapter 4. The damping constant  $d$  is 500 Ns/m and the displacement amplitude  $x_0$  is assumed to be 100 nm. The natural frequency of the setup is 1150 Hz which is used for  $\omega$  in (D-3). This leads to an average power dissipation of 130  $\mu$ W. In case a steel fin and slot part are assumed of 10 g, the temperature increase in 1 minute amounts 1.6e-3 K.

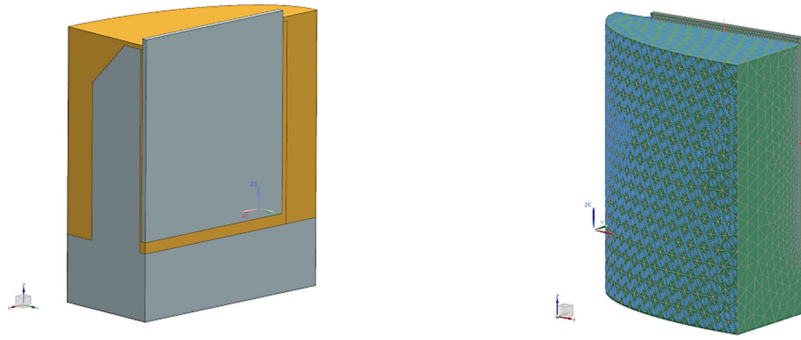


Figure D1: a) Quarter damper model and b) corresponding FEM model.

To provide more insight in the temperature increase over time, the transient behavior is calculated by means of FEM. Because of the damper symmetry, only a quarter has been modelled. This quarter of the fin and slot part is presented in Figure D1a. Figure D1b shows the FEM model in which a heat load of a quarter of  $130 \mu\text{W}$  is defined and heat convection to the environment. The fin and slot material is defined as steel and for the material in between the properties of oil are defined. A transient calculation shows the temperature increase over one hour of excitation, in which a steady state is reached. The resulting temperature distribution is presented in Figure D2a.

Points 1 and 2 indicate the locations at which the transient response is calculated. These two transients are presented in Figure D2b. The initial slope of the responses corresponds to the estimated value of  $1.6 \times 10^{-3} \text{ K/min}$  as calculated on the previous page.

These calculations show that the temperature increase during measuring for fluid characterization, even with a relatively long measurement time, will not be visible in the resulting frequency response. This is important with respect to the frequency response measurements and corresponding model quality as presented in Chapter 4.

In addition, it provides an estimate for the damper behavior in case of practical implementation at a motion stage. For implementation, the resulting temperature might be

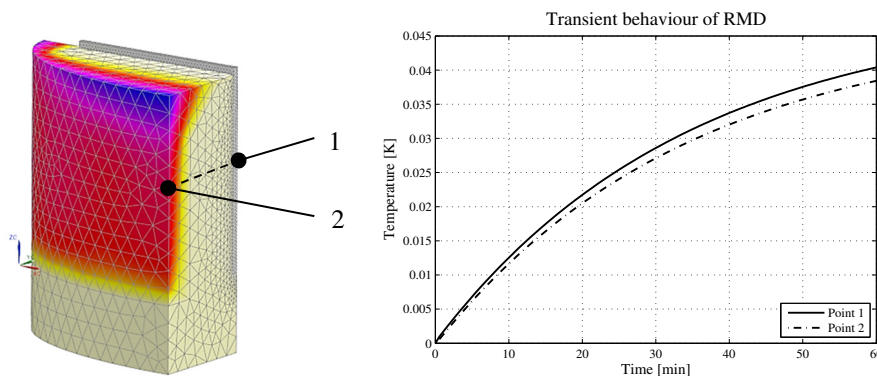


Figure D2: a) Temperature distribution in the fin, slot and damper fluid after one hour of excitation.

Point 1 and 2 show the locations at which the transient behavior is calculated. The transients are presented in Figure D2b.

smaller than estimated by these calculations, as:

- the amplitudes are smaller, which is quadratically included in the equations,
- the damper is excited discontinuously, which provides unexcited time. This enables the damper to cool down during operation,
- the energy dissipation is lower for high frequencies due to the linear viscoelastic behavior, which shows a damping decrease and, therefore, a dissipation decrease as function of frequency (see Chapter 4 and Appendix C).

## Appendix E RMD design with two degrees of freedom

This thesis presents an RMD design which allows to increase the modal damping of resonances. The maximal resonance suppression is a function of the normalized displacement of the corresponding mode. This implies however, that a certain resonance cannot be damped if it doesn't show displacements at the RMD locations. For the stage designs as discussed, this implies that mode shapes that don't show displacements at the corners, cannot be damped. For plate like structures, these undampable NRB modes start with the saddle mode. See for instance Chapter 2 and 5.

To increase the modal damping of a larger amount of structural modes, a few solution directions can be explored:

- the location of the dampers on the stage can be changed. This usually reduces the efficiency for the BW limiting modes but can increase the number of modes that can be influenced,
- the stage design can be adapted, i.e., a non-symmetrical stage can be designed,
- the RMD design can be adapted to influence the other modes too.

The latter is elaborated upon in this appendix. Figure E1 shows modes 7, 8 and 15 of a square plate. These modes are respectively the torsion mode, the saddle mode and a higher order saddle mode.

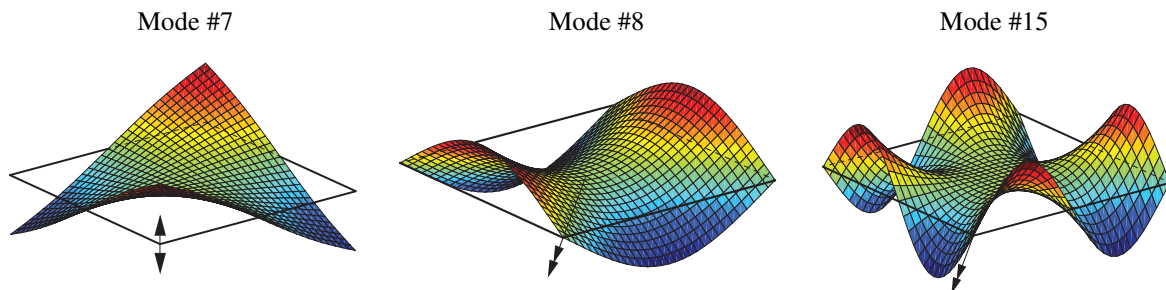


Figure E1: Three mode shapes of a square plate, respectively mode 7, 8 and 15. Mode 7 shows a translation at the plate's corner. Mode 8 and 15 show rotations around the plate diagonal.

Figure E1 shows that modes that do not show displacements at the stage corners, have a nodal line crossing the stage's corner and therefore show a rotation at this location. Therefore, an RMD design that will be able to damp all out-of-plane modes can be designed containing:

- a translation in vertical direction,
- a rotation around the stage's diagonal.

This appendix shows an idea for the mechanical realization of a two degree of freedom RMD.

In addition to the translational RMD as described in this thesis, an additional degree of freedom should be added. This implies that the structural material should be shaped in such a way that two DoFs have a relatively low stiffness and four DoFs have a relatively high

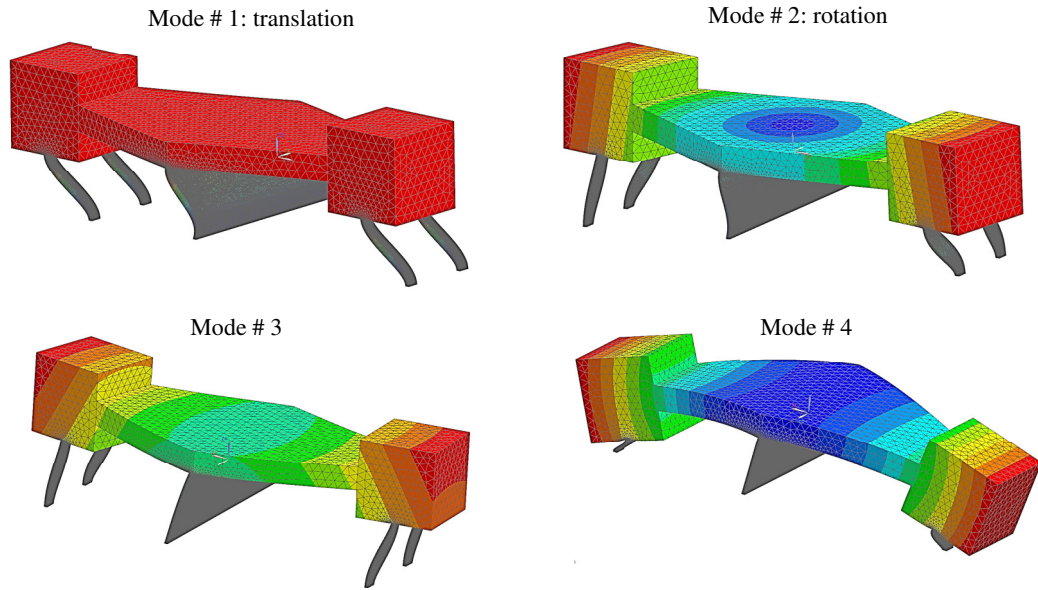


Figure E2: The first four mode shapes of the mechanical part of a two degree of freedom RMD design. The corresponding natural frequencies are listed in Table E1.

stiffness. In addition, the translational mass should be designed in such a way that an as high as possible moment of inertia is obtained to damp the rotational DoFs.

A two DoF RMD design is presented in [95]. This design is statically determined, fixing 4 DoF and enabling 2 DoF; a translation and a rotation. The resonance suppression factor is a function of the RMD mass and likewise, the rotational suppression is a function of the moment of inertia. Therefore, the RMD design is aimed at maximizing the moment of inertia with a fixed amount of mass. According to the formula of Huygens-Steiner, the most efficient way to obtain this is by enlarging the effective length of the mass with respect to the center of rotation. This results in a design of two masses connected by an intermediate body. This design, including the first four mode shapes, is presented in Figure E2.

Table E1: The mechanical properties of the two DoF RMD and the corresponding natural frequencies.

| Properties of the RMD design |                             | Value | Unit              |
|------------------------------|-----------------------------|-------|-------------------|
| Moving mass                  |                             | 35e-3 | kg                |
| Moment of inertia            |                             | 15e-6 | kg·m <sup>2</sup> |
| Mode nr.                     | Mode description            | Value | Unit              |
| Mode # 1                     | Transation                  | 1250  | Hz                |
| Mode # 2                     | Rotation                    | 1800  | Hz                |
| Mode # 3                     | Plate spring in-plane-shear | 7230  | Hz                |
| Mode # 4                     | Tension of the struts       | 8900  | Hz                |

Because of the small mass percentage that is included in the intermediate body and the relatively large distance between the two masses, the four struts are applied to counteract internal degrees of freedom. The mechanical properties and the frequencies corresponding to the mode shapes as presented are listed in Table E1.

After calculation of the optimal damper properties for a specific stage design, a physical damper has to be designed, which is more difficult than in case of the single DoF RMD.



## References

- [1] Abe, M., & Fujino, Y. (1994). Dynamic characterization of multiple tuned mass dampers and some design formulas. *Earthquake engineering & structural dynamics*, 23(8), 813-835.
- [2] Abe, M. (1996). Semi-Active tuned mass dampers for seismic protection of civil structures. *Earthquake engineering & structural dynamics*, 25(7), 743-749.
- [3] Adhikari, S. (2000). Damping models for structural vibration. *University of Cambridge, Cambridge*.
- [4] Agrawal, D. K., & Roy, R. (1985). Composite route to “zero” expansion ceramics. *Journal of materials science*, 20(12), 4617-4623.
- [5] Alander, J. T. (1992, May). On optimal population size of genetic algorithms. In *CompEuro'92. Computer Systems and Software Engineering, Proceedings*. (pp. 65-70). IEEE.
- [6] Al-Hulwah, K. I., & Kashani, R. (2004, January). Floor vibration control using three-degree-of-freedom tuned mass dampers. In *ASME 2004 International Mechanical Engineering Congress and Exposition* (pp. 509-515). American Society of Mechanical Engineers.
- [7] Åström, K. J., Panagopoulos, H., & Hägglund, T. (1998). Design of PI controllers based on non-convex optimization. *Automatica*, 34(5), 585-601.
- [8] Ashby, M. F., & Cebon, D. (1993). Materials selection in mechanical design. *Le Journal de Physique IV*, 3(C7), C7-1.
- [9] Back, T. (1996). *Evolutionary algorithms in theory and practice*. Oxford Univ. Press.
- [10] Balas, G. J., & Doyle, J. C. (1994). Control of lightly damped, flexible modes in the controller crossover region. *Journal of guidance, control, and dynamics*, 17(2), 370-377.
- [11] Balendra, T., Wang, C. M., & Cheong, H. F. (1995). Effectiveness of tuned liquid column dampers for vibration control of towers. *Engineering Structures*, 17(9), 668-675.
- [12] Benzing, D. W., & Russel, W. B. (1981). The viscoelastic properties of ordered lattices: experiments. *Journal of Colloid and Interface Science*, 83(1), 178-190.



- [13] Bert, C. W. (1973). Material damping: An introductory review of mathematic measures and experimental technique. *Journal of Sound and Vibration*, 29(2), 129-153.
- [14] Blom, C., & Mellema, J. (1984). Torsion pendula with electromagnetic drive and detection system for measuring the complex shear modulus of liquids in the frequency range 80–2500 Hz. *Rheologica acta*, 23(1), 98-105.
- [15] Bodden, D. S., & Junkins, J. L. (1985). Eigenvalue optimization algorithms for structure/controller design iterations. *Journal of Guidance, Control, and Dynamics*, 8(6), 697-706.
- [16] 16 - Book, W.J., Controlled Motion in an Elastic World, *Journal of Dynamic Systems, Measurement and Control*, 50th Anniversary Issue, March 1993, p. 252-261
- [17] Bruijnen, D., & van Dijk, N. (2012, June). Combined input shaping and feedforward control for flexible motion systems. In *American Control Conference (ACC), 2012* (pp. 2473-2478). IEEE.
- [18] Butler H., (2011). Position control in lithographic equipment: An enabler for current-day chip manufacturing. *IEEE Control Systems Magazine*, 31(5):28-47.
- [19] Chen, D., & Seborg, D. E. (2003). Design of decentralized PI control systems based on Nyquist stability analysis. *Journal of Process Control*, 13(1), 27-39.
- [20] Chung, D. D. L. (2001). Review: Materials for vibration damping. *Journal of Materials Science*, 36(24), 5733-5737.
- [21] Cao, H., Reinhorn, A. M., & Soong, T. T. (1998). Design of an active mass damper for a tall TV tower in Nanjing, China. *Engineering Structures*, 20(3), 134-143
- [22] Crandall, S. H. (1970). The role of damping in vibration theory. *Journal of Sound and Vibration*, 11(1), 3-IN1.
- [23] De Kraker, de, (2004). *A numerical-experimental approach in structural dynamics*. Shaker Publishing.
- [24] De Roover, D., & Bosgra, O. H. (2000). Synthesis of robust multivariable iterative learning controllers with application to a wafer stage motion system. *International Journal of Control*, 73(10), 968-979.
- [25] Den Hartog, J.P., *Mechanical Vibrations* (4<sup>th</sup> edn). McGraw-Hill, New York, 1956. (Reprinted by Dover, New York, 1985)
- [26] Desoer, C. A., & Wang, Y. T. (1980). On the generalized Nyquist stability criterion. *Automatic Control, IEEE Transactions on*, 25(2), 187-196.
- [27] Dejima, S., Gao, W., Shimizu, H., Kiyono, S., & Tomita, Y. (2005). Precision positioning of a five degree-of-freedom planar motion stage. *Mechatronics*, 15(8), 969-987.

- [28] Diaz-Gomez, P. A., & Hougen, D. F. (2007). Initial Population for Genetic Algorithms: A Metric Approach. In *GEM* (pp. 43-49).
- [29] Ferry, J. D. (1980). *Viscoelastic properties of polymers*. John Wiley & Sons.
- [30] Franklin G.F., Powell J.D., Emami-Naeini A., (1994) Feedback control of dynamic systems, *robotics.itee.uq.edu.au*
- [31] Fritz, G., Pechhold, W., Willenbacher, N., & Wagner, N. J. (2003). Characterizing complex fluids with high frequency rheology using torsional resonators at multiple frequencies. *Journal of Rheology (1978-present)*, 47(2), 303-319.
- [32] Gaul, L. (1999). The influence of damping on waves and vibrations. *Mechanical systems and signal processing*, 13(1), 1-30.
- [33] Gawronski, W. K. (2004). *Advanced structural dynamics and active control of structures* (Vol. 1). New York: Springer.
- [34] Guo, Y. Q., & Chen, W. Q. (2007). Dynamic analysis of space structures with multiple tuned mass dampers. *Engineering Structures*, 29(12), 3390-3403.
- [35] Griffin, W. S., Richardson, H. H., & Yamanami, S. (1966). A study of fluid squeeze-film damping. *Journal of Fluids Engineering*, 88(2), 451-456.
- [36] Grefenstette, J. J. (1986). Optimization of control parameters for genetic algorithms. *Systems, Man and Cybernetics, IEEE Transactions on*, 16(1), 122-128.
- [37] Havre, K., & Skogestad, S. (1996). Effect of RHP zeros and poles on performance in multivariable systems.
- [38] Havre, K., & Skogestad, S. (2001). Achievable performance of multivariable systems with unstable zeros and poles. *International Journal of Control*, 74(11), 1131-1139.
- [39] Herpen, R. van, Oomen, T., Kikken, E., Wal, M. van de, Aangenent, W., Steinbuch, M., Exploting additional actuators and sensors for nano-positioning robust motion control, *Submitted*
- [40] Huan, S.C., Inman, D.J., & Austin, E.M., Some design considerations for active and passive constrained layer damping treatments, *Smart Materials and Structures*, Vol. 5 (1996) p. 301-313
- [41] Huang, S. C., Inman, D. J., & Austin, E. M. (1996). Some design considerations for active and passive constrained layer damping treatments. *Smart Materials and Structures*, 5(3), 301.
- [42] Johnson, C. D. (1995). Design of passive damping systems. *Journal of Vibration and Acoustics*, 117(B), 171-176.
- [43] Kim, O. S., Lee, S. H., & Han, D. C. (2003). Positioning performance and straightness error compensation of the magnetic levitation stage supported by the linear magnetic bearing. *Industrial Electronics, IEEE Transactions on*, 50(2), 374-378.

- [44] Kim, S. M., Wang, S., & Brennan, M. J. (2011). Dynamic analysis and optimal design of a passive and an active piezo-electrical dynamic vibration absorber. *Journal of Sound and Vibration*, 330(4), 603-614.
- [45] Kish, L. B. (2002). End of Moore's law: thermal (noise) death of integration in micro and nano electronics. *Physics Letters A*, 305(3), 144-149.
- [46] Krenk, S., & Høgsberg, J. (2008). Tuned mass absorbers on damped structures under random load. *Probabilistic Engineering Mechanics*, 23(4), 408-415
- [47] Krenk, S. & Hogsberg, J., (2008) Tuned Mass Absorbers on damped structures, 7<sup>th</sup> European Conference on Structural Dynamics, Southampton, 7-9 July
- [48] Kolda, T. G., Lewis, R. M., & Torczon, V. (2003). Optimization by direct search: New perspectives on some classical and modern methods. *SIAM review*, 45(3), 385-482.
- [49] Konno A., Makino S., Kaneko M., (1968) Measurements of the mechanical properties of a polymer solution, *Jap. Journal of Applied Physics*, 7, pp89,
- [50] Krohling, R. A., & Rey, J. P. (2001). Design of optimal disturbance rejection PID controllers using genetic algorithms. *Evolutionary Computation, IEEE Transactions on*, 5(1), 78-82.
- [51] Kwok, K. C. (1984). Damping increase in building with tuned mass damper. *Journal of Engineering Mechanics*, 110(11), 1645-1649.
- [52] Kwok, K. C. S., & Samali, B. (1995). Performance of tuned mass dampers under wind loads. *Engineering Structures*, 17(9), 655-667.
- [53] Lallart, M., Yan, L., Wu, Y. C., & Guyomar, D. (2013). Electromechanical semi-passive nonlinear tuned mass damper for efficient vibration damping. *Journal of Sound and Vibration*, 332(22), 5696-5709.
- [54] Lambrechts P., Boerlage M., Steinbuch M., (2005). Trajectory planning and feedforward design for electromechanical motion systems. *Control Engineering Practice* 13 145-157/ doi:10.1016/j.conengprac.2004.02.010
- [55] Lee, H. S., & Tomizuka, M. (1996). Robust motion controller design for high-accuracy positioning systems. *Industrial Electronics, IEEE Transactions on*, 43(1), 48-55.
- [56] Mann, C. C. (2000). The End of Moores Law. *Technology Review*, 103(3), 42-48.
- [57] Makosko, C. W. (1994). Rheology principles, measurements, and applications. *VCH, New York*.
- [58] Martinez V.M., Edgar T.F., (2006). Control of lithography in semiconductor manufacturing. *IEEE Control Systems Magazine* 26(6): 46-55
- [59] Meckl, P. H., & Kinceler, R. (1994). Robust motion control of flexible systems using feedforward forcing functions. *Control Systems Technology, IEEE Transactions on*, 2(3), 245-254.

- [60] Middleton, R. H. (1991). Trade-offs in linear control system design. *Automatica*, 27(2), 281-292.
- [61] Moore, G. E. (1965). Cramming more components onto integrated circuits. *Electron. Mag.*
- [62] Moore, G. E. (1995, May). Lithography and the future of Moore's law. In *SPIE's 1995 Symposium on microlithography* (pp. 2-17). International Society for Optics and Photonics.
- [63] Nishimura, I., Kobori, T., Sakamoto, M., Koshika, N., Sasaki, K., & Ohrui, S. (1992). Active tuned mass damper. *Smart Materials and Structures*, 1(4), 306-311.
- [64] Oakley, J. G., & Giacomini, A. J. (1994). A sliding plate normal thrust rheometer for molten plastics. *Polymer Engineering & Science*, 34(7), 580-584.
- [65] Ohnishi, K., Shibata, M., & Murakami, T. (1996). Motion control for advanced mechatronics. *Mechatronics, IEEE/ASME Transactions on*, 1(1), 56-67.
- [66] Oomen, T., van Herpen, R., Quist, S., van de Wal, M., Bosgra, O., & Steinbuch, M. (2014). Connecting system identification and robust control for next-generation motion control of a wafer stage. *Control Systems Technology, IEEE Transactions on*, 22(1), 102-118.
- [67] Oosterbroek, M., Waterman, H. A., Wiseall, S. S., Altena, E. G., Mellema, J., & Kip, G. A. M. (1980). Automatic apparatus, based upon a nickel-tube resonator, for measuring the complex shear modulus of liquids in the kHz range. *Rheologica Acta*, 19(4), 497-506.
- [68] Pechold W., (1959) Eine method zur messung des komplexen schubmoduls im frequenzbereich 1-100 kHz, *Acustica* 9.1, 39-48.
- [69] Pedersen, N. L. (2000). Maximization of eigenvalues using topology optimization. *Structural and multidisciplinary optimization*, 20(1), 2-11.
- [70] Pinkaew, T., & Fujino, Y. (2001). Effectiveness of semi-active tuned mass dampers under harmonic excitation. *Engineering Structures*, 23(7), 850-856.
- [71] Pintelon, R., & Schoukens, J. (2012). *System identification: a frequency domain approach*. John Wiley & Sons.
- [72] Pombo, J. L., & Laura, P. A. A. (1986). Use of two dynamic vibration absorbers in the case of machinery operating at two frequencies which coincide with two natural frequencies of the system. *Applied Acoustics*, 19(1), 41-45.
- [73] Powell, J. R. (2008). The quantum limit to Moore's law. *Proceedings of the IEEE*, 96(8), 1247-1248.
- [74] Preumont, A., *Vibration Control of Active Structures*, Springer-Verlag, Berlin Heidelberg, 2011

- [75] Rao, S. S., & Rao, S. S. (2009). *Engineering optimization: theory and practice*. John Wiley & Sons.
- [76] Ragueneau, F., La Borderie, C., Mazars, J. (2000). Damage model for concrete-like materials coupling cracking and friction, contribution towards structural damping: first uniaxial applications. *Mechanics of Cohesive-frictional Materials*, 5(8), 607-625.
- [77] Ronde, M., van de Molengraft, R., & Steinbuch, M. (2012, June). Model-based feedforward for inferential motion systems, with application to a prototype lightweight motion system. In *American Control Conference (ACC), 2012* (pp. 5324-5329). IEEE.
- [78] Rosenbrock, H. H. (1970). State-space and multivariable theory.
- [79] Roy, R., Agrawal, D. K., Alamo, J., & Roy, R. A. (1984). [CTP]: a new structural family of near-zero expansion ceramics. *Materials research bulletin*, 19(4), 471-477.
- [80] Schaller, R. R. (1997). Moore's law: past, present and future. *Spectrum, IEEE*, 34(6), 52-59.
- [81] Schmidt, P., & Rehm, T. (1999). Notch filter tuning for resonant frequency reduction in dual inertia systems. In *Industry Applications Conference, 1999. Thirty-Fourth IAS Annual Meeting. Conference Record of the 1999 IEEE* (Vol. 3, pp. 1730-1734). IEEE.
- [82] Schneiders, M.G.E., Van De Molengraft, M.J.G., & Steinbuch, M., Benefits of over-actuation in motion systems, *Proceedings of the American Control Conference*, Boston, Massachusetts, 2004, June 30 –July 2, p. 505-510
- [83] Schönhoff U., Normann,R., (2002). A  $H_\infty$ -weighting scheme for PID-like motion control. *Proc. IEEE International Conference on Control Applications*, Glasgow, Scotland, UK. p.192-197.
- [84] Schrag, J. L., & Johnson, R. M. (1971). Application of the Birnboim multiple lumped resonator principle to viscoelastic measurements of dilute macromolecular solutions. *Review of Scientific Instruments*, 42(2), 224-232.
- [85] Schrag, J. L. (1977). Deviation of velocity gradient profiles from the “gap loading” and “surface loading” limits in dynamic simple shear experiments. *Transactions of The Society of Rheology (1957-1977)*, 21(3), 399-413.
- [86] Skogestad, S., & Postlewaite, I., *Multivariable Feedback Control*, John Wiley & sons Ltd. Chichester, 2005
- [87] Soovere, J., & Drake, M. L. (1985). *Aerospace Structures Technology Damping Design Guide. Volume 1. Technology Review*. LOCKHEED-CALIFORNIA CO BURBANK.
- [88] Stix, G., (1995) Trends in semiconductor manufacturing: Toward “point one”. *Scientific American*, 272(2), 72–77.

- [89] Steinbuch, M., & Van de Molengraft, M. J. G. (2000). Iterative learning control of industrial motion systems. In *1st IFAC Conference on Mechatronic Systems*, Darmstadt, Germany (pp. 967-972).
- [90] Stokich, T. M., Radtke, D. R., White, C. C., & Schrag, J. L. (1994). An instrument for precise measurement of viscoelastic properties of low viscosity dilute macromolecular solutions at frequencies from 20 to 500 kHz. *Journal of Rheology (1978-present)*, 38(4), 1195-1210.
- [91] Swevers, J., Pipeleers, G., Diehl, M., & De Schutter, J. (2010, March). Pushing motion control systems to their limits using convex optimization techniques. In *Advanced Motion Control, 2010 11th IEEE International Workshop on* (pp. 807-814). IEEE.
- [92] Steinbuch, M., & Norg, M. L. (1998). Advanced motion control: An industrial perspective. *European Journal of Control*, 4(4), 278-293.
- [93] Silvas, E., Hoogendijk, R., Aangenent, W., & Steinbuch, M. V. D. W. M. Modal Decoupling of a Lightweight Motion Stage Using Algebraic Constraints on the Decoupling Matrices.
- [94] Sittel, K., Rouse Jr, P. E., & Bailey, E. D. (1954). Method for Determining the Viscoelastic Properties of Dilute Polymer Solutions at Audio-Frequencies. *Journal of Applied Physics*, 25(10), 1312-1320.
- [95] Steur, M.M.A. (2012). Designing a TMD for wafer stage implementation, CST Report, Eindhoven University of Technology
- [96] Thompson, S. E., & Parthasarathy, S. (2006). Moore's law: the future of Si microelectronics. *Materials Today*, 9(6), 20-25.
- [97] Thramboulidis, K., Model-Integrated Mechatronics – Toward a New Paradigm in the Development of Manufacturing Systems, *IEEE Transactions on Industrial Informatics*, Vol. 1 - No. 1, February 2005
- [98] Umeno, T., Kaneko, T., & Hori, Y. (1993). Robust servosystem design with two degrees of freedom and its application to novel motion control of robot manipulators. *Industrial Electronics, IEEE Transactions on*, 40(5), 473-485.
- [99] Van Herpen, R., Oomen, T. A. E., Van de Wal, M., & Bosgra, O. H. (2009). Robust Beyond-Rigid-Body Control of Next Generation Wafer Stages.
- [100] Van Herpen, R., Oomen, T., & Bosgra, O. (2011, June). A robust-control-relevant perspective on model order selection. In *American Control Conference (ACC), 2011* (pp. 1224-1229). IEEE.
- [101] Van De Wal, M., & De Jager, B. (2001). A review of methods for input/output selection. *Automatica*, 37(4), 487-510.
- [102] Van de Wal M., Van Baars G., Sperling F., Bosgra O.H., (2002) Multivariable  $H_\infty/\mu$  feedback control design for high-precision wafer stage motion, *Control Engineering Practice* 10 739–755

- [103] Van der Meulen, S. H., Tousain, R. L., & Bosgra, O. H. (2008). Fixed structure feedforward controller design exploiting iterative trials: Application to a wafer stage and a desktop printer. *Journal of Dynamic Systems, Measurement, and Control*, 130(5), 051006.
- [104] Verbaan, C. A. M., Rosielle, P. C. J. N., & Steinbuch, M. (2014). Broadband damping of non-rigid-body resonances of planar positioning stages by tuned mass dampers. *Mechatronics*, 10.1016/j.mechatronics.2013.12.013
- [105] Wielen, A.M. van der, Positioning System Mass Reduction due to Exchange of Structural Stiffness by Additional Actuators, PhD Thesis, Technische Universiteit Eindhoven, Eindhoven, The Netherlands, 2009
- [106] Yan, M. J., & Dowell, E. H. (1972). Governing equations for vibrating constrained-layer damping sandwich plates and beams. *Journal of Applied Mechanics*, 39(4), 1041-1046.
- [107] Yang, C., Li, D., & Cheng, L. (2011). Dynamic vibration absorbers for vibration control within a frequency band. *Journal of Sound and Vibration*, 330(8), 1582-1598.
- [108] Yao, B., & Jiang, C. (2010, March). Advanced motion control: from classical PID to nonlinear adaptive robust control. In *Advanced Motion Control, 2010 11th IEEE International Workshop on* (pp. 815-829). IEEE.
- [109] Zhang, H., Shi, Y., & Saadat Mehr, A. (2011). Robust non-fragile dynamic vibration absorbers with uncertain factors. *Journal of Sound and Vibration*, 330(4), 559-566.
- [110] Zuo, L., & Nayfeh, S. A. (2006). The two-degree-of-freedom tuned-mass damper for suppression of single-mode vibration under random and harmonic excitation. *Journal of vibration and acoustics*, 128(1), 56-65.
- [111] Zuo, L. (2009). Effective and robust vibration control using series multiple tuned-mass dampers. *Journal of Vibration and Acoustics*, 131(3), 031003.







# Woorden van dank

Een promotietraject is veel meer groepsprestatie dan de ene naam op de kaft doet vermoeden. Veel mensen zijn betrokken geweest en zonder hun hulp en advies zou er in veel gevallen nogal eenzijdig onderzoek zijn uitgevoerd.

Maarten, bedankt voor je vertrouwen en ondersteuning. Ik zal me altijd herinneren hoe snel je dwarsverbanden trok van mechanische oplossingen naar regeltechnische equivalenten. Dat is voor mij als constructeur bijzonder waardevol geweest. Het feit dat ik altijd even binnen kon vallen om je een vraag te stellen bleek onmisbaar om meters te kunnen maken binnen het project. Nick, je onuitputtelijke stroom van ideeën, gecombineerd met je vasthoudendheid om een probleem op te lossen, blijven voor mij een voorbeeld. Graag wil ik je danken voor je ondersteuning en de open gesprekken die we hebben gehad: Het begrip begeleider heeft voor mij gedurende dit traject aan diepgang gewonnen. De commissieleden wil ik danken voor de bereidheid om zitting te nemen en voor de feedback op deze thesis.

ASML Research heeft, naast de financiering van zowel de promotieplaats als de experimentele opstellingen, zich niet onbetuigd gelaten in de begeleiding van dit project. In dit kader wil ik Hans Vermeulen danken alsmede Stan van der Meulen, Marc van de Wal, Ton de Groot en Wouter Aangenent. Stan en Marc; de sparsessies die ik met jullie heb gehad, hebben de industriële toepasbaarheid van dit werk doen stijgen. Dit beschouw ik, mede vanuit mijn achtergrond, als bijzonder waardevol. Stan, ook bedankt voor het doornemen van de thesis tot in detail en het geven van kritische feedback: Hierdoor is het proefschrift inhoudelijk een niveau gestegen. Dank ook aan George Leenknecht, die me in een beperkte hoeveelheid tijd door de hoge complexiteit van de experimentele opstellingen heeft geloodst.

De demper hardware is vervaardigd door TU/e EPC. Erwin Dekkers, Luciano Oorthuizen en René Henselmans, bedankt voor het gemakkelijke overleg en de resulterende hardware: Jullie vakmanschap is te zien in de kwaliteit van de meetresultaten in dit proefschrift.

Aan het begin van dit project heb ik me ingewerkt in het modelleren van dynamische systemen. In het bijzonder ben ik Robbert van Herpen, Rob Hoogendijk en Michael Ronde dank verschuldigd omdat ik bij hen binnen kon vallen met vragen die hier betrekking op hadden. Later in het traject hebben Bert Maljaars en Pascal Etman me met grote snelheid wegwijs gemaakt in de mogelijkheden van optimalisietechnieken, welke zich in meerdere hoofdstukken van deze thesis hebben bewezen.

De collega's van de Control Systems Technology group: Dank voor de mooie tijd. Graag wil ik Bas, David, Elize, Frank, Gerrit, Jan, Matthijs, Menno, Sinan, Tom en Rick noemen. Met sommigen van jullie bewaar ik hierbovenop goede herinneringen aan conferenties.

Vanuit het lab zal ik me de constructieve en hulpvaardige houding van collega's herinneren, waarbij gezelligheid nooit ontbrak: Linda, Roger, Chris, Ron, Thijs, Simon, Geert-Jan, Raimondo, Arjo, Jordan, Marc en Micha, bedankt! Micha, bedankt voor je bijdrage in de vorm van een stageopdracht. Marc, bedankt voor het lezen van een groot deel van deze thesis.

Petra en Geertje, jullie zijn onmisbaar voor ons als promovendi! Bij jullie kon ik altijd terecht voor vragen van algemene aard. Dank voor de gesprekken met oprechte interesse in de persoon zelf. Karin, dank je voor het verzorgen van mijn werkomgeving en de goede gesprekken die we gevoerd hebben.

Vrienden buiten de TU hebben ervoor gezorgd dat de broodnodige afleiding ook aanwezig was: Erik, Gert, Hans en Koen; met jullie heb ik, in aanvulling op de vriendschappelijke band, een gedeelde passie voor en geschiedenis in techniek en tweewielers. Luuk & Ida, Cees & Petra, Ina & Bertjan, Govert & Corina, Peter & Pieta, Marian & Martijn, Mirjam, Wijnand en Barend, bedankt voor alle mooie, soms bewogen, uren die we de afgelopen vele jaren samen hebben doorgebracht.

Pa en ma Van Erk, bedankt voor het mede-mogelijk maken van de afgelopen studiejaren. Niet minder bedankt voor de gezelligheid en interesse: Het even 'naar de andere kant' kunnen lopen voor een bakkie koffie was af en toe de juiste afleiding om daarna weer verder te gaan.

Pa en ma, ik wil jullie danken dat jullie mij hebben opgevoed op een manier die dit resultaat mogelijk heeft gemaakt. Leren doorzetten is één van de meest waardevolle lessen geweest. Bedankt voor het vrij laten om eigen keuzes te maken en de ondersteuning daarin. Jullie hebben, over lange tijd, heel veel bijgedragen: Een rugzak met vaardigheden om dit te kunnen doen.

Lieve Susanne. Alweer 7,5 jaar geleden hebben we besloten om samen verder te gaan: Ik ervaar dat dagelijks als verreweg de beste keuze die we gemaakt hebben tot nog toe. Bedankt voor de onvoorwaardelijke steun. Het is voor omstanders slecht zichtbaar, maar jij hebt een heel groot aandeel in dit werk: Jij bent voor mij mede-eerste auteur van dit proefschrift.

# Curriculum Vitae



Kees Verbaan was born on September 15<sup>th</sup>, 1983 in Utrecht, The Netherlands. After primary school he finished his secondary education at 't Gilde in Gorinchem in 2000. Subsequently, he studied mechanical engineering at ROC ASA Scutos in Utrecht and the Hogeschool van Utrecht. In 2007, he obtained the degree of Bachelor of Engineering from the Hogeschool van Utrecht (*with great appreciation*). He did his graduation project for TNO Applied Production and Precision Equipment working on a flexible endoscope for vitreoretinal eye surgery.

After finishing the pre-master program, he studied Mechanical Engineering at Eindhoven University of Technology and obtained the master's degree in 2010 (*Cum Laude*). He did his graduation project for ASML Research Mechatronics which resulted in a master's thesis entitled "Light Weight Short Stroke Stage Design for Ø 450 mm Wafers – an iterative approach".

January 2011, he started as a Ph.D. student in the Control Systems Technology group, under supervision of prof.dr.ir. M. Steinbuch and dr.ir. P.C.J.N. Rosielle, and worked on a project for ASML Research Mechatronics & Control. This project resulted in this thesis.